Cobalt-Doped Zinc Oxide Dilute Magnetic Semiconductors for Spintronics Devices

Liu Qing

School of Materials Science and Engineering

A thesis submitted to the Nanyang Technological University
in fulfillment of the requirement for the degree of
Doctor of Philosophy

2009

Abstract

In recent years, Dilute Magnetic Semiconductors (DMS) with ZnO as host materials have attracted enormous attention. Structural and magnetic properties of $Zn_{0.95}Co_{0.05}O$ thin films grown on *n*-type (001) silicon by pulsed laser deposition method were characterized. Contributions by metallic cobalt nanoclusters, oxygen partial pressure and substrate deposition temperature to ferromagnetism were investigated. Experiments have shown that the observed ferromagnetism in Co-doped ZnO thin films was not due to the metallic cobalt nanoclusters. Bound magnetic polaron (BMP) model and Ruderman-Kittel-Kasuya-Yosida (RKKY) interaction are the two mechanisms that most likely explain the origins of $Zn_{0.95}Co_{0.05}O$ ferromagnetism. The amount of oxygen vacancies, which could be adjusted by varying the oxygen partial pressure during DMS thin film deposition, affects the polaron density in the BMP model that leads to formation of long range order of magnetic cations. It was also demonstrated that there is an optimal substrate temperature range for maximum saturation magnetization as a balance between the carrier concentration and carrier mean free path have to be achieved. Metal-insulator-semiconductor structures were fabricated by pulsed laser deposition method to investigate the injection of carriers by an external electric field into the DMS layer. Under different applied electric field, the carrier concentration in the Co-doped ZnO layer was adjusted. This led to a change in the ferromagnetic properties of the DMS layer that could be explained by the RKKY mechanism.

Furthermore, ordered DMS nanostructures are attractive for their potential applications in nano-spintronic devices. With an anodic aluminum oxide template, ferromagnetic $Zn_{0.95}Co_{0.05}O$ DMS nano-dots with 50 nm diameter were fabricated through pulsed laser deposition method. With vertically aligned ZnO nanowires as templates, ferromagnetic $ZnO/Zn_{0.95}Co_{0.05}O$ core-shell nanowires were also fabricated using pulsed laser ablation technique. No superparamagnetic or spin glass state was observed from the magnetization-field curves with zero field cooling and field cooling.

Acknowledgements

I am indebted to my supervisors, Dr. Gan Chee Lip and Dr Han Guchang who have given me the opportunity to embark on this project. I am also grateful to their direction, encouraging and patient guidance through my four years.

I thank the School of Materials Science and Engineering of Nanyang Technological University for the financial support.

Special thanks go to my team members and friends: Li Shaozhou, Cai Hui, Tan Tam Lyn, Dr Yuan Cailei and Peter Darmawan of their help in lab work, discussions and of course, friendship. I would also like to send my appreciation to technicians during the experiments: Mastura Aidel, Sandy Leong, Heryani Binte Ahmad, Wu Shu Cheng, John Koh, Low Jim Hee, Wang Lee Chin, Irene Heng, Maung Zaw Tun, Guo Jun day to day support in my lab work.

Last but not least, I own much to my parents who are always supporting me.

Table of Content

List of Figures

List of Tables

Chapter 1: Introduction

1.1 Research Motivation

Conventional electronics function by the charge property of electrons, and ignore the spin of the electrons. Although electron spin is known since earlier 20^{th} century, there has been seldom technical use of this fact till today [1]. In every hi-fi and radio set, around 50% of the conducting electrons tend to be spin up and the remainders are spin down. Spin up and spin down electrons have different transport properties, which act like two families of charger carriers. Ferromagnetic exchange field can split the spin up and spin down conduction bands, leaving different band structures at the Fermi surface, such that the number of electrons left in the conduction band is different for the two types of spins. Further more, because the density of states for spin up and spin down electrons is different, the scattering of the two spin types is different, such that their mobility is different [2-5]. In recent years, the integration of spin electronic as spintronic devices into conventional semiconductor technology has attracted more attention. Devices based on spin-dependent effects such as read heads for hard disks or non-volatile magnetic random access memory have a strong impact on storage technology [6, 7]. However, spin coherent transport in semiconductors has three main issues: (1) spin-coherence effects within the semiconductor, (2) spin injection into the semiconductor from the outside world, and (3) detection of the spin polarized current. Among these three issues, a long electron spin coherence length in the micro meter range has been demonstrated for spin transport [8]. Spin injection has also attracted a lot of researchers' interests, and two possible spin injection methods were investigated. The first is injection from a metallic ferromagnetic electrode by tunneling effect, and the second is injection from a ferromagnetic semiconductor. So far, the first method has been proven to be poor for the spin injection, and the second method needs to be further investigated for a breakthrough [9-14]. For ferromagnetic semiconductors, the Curie temperature is typically below 100 K, so alternatives have to be searched which exhibits ferromagnetism at room temperature for the devices' applications. One way is to use non-magnetic semiconductors doped with magnetic atoms, which are called dilute magnetic semiconductors (DMS) [15-17]. However, the origins of this ferromagnetism in DMS need to be investigated. Currently, some oxide based DMS have been reported to be robust, room temperature Ferro magnets, and the host materials used are group II-VI elements [18-22]. However, there are still questions to be answered about the DMS materials. What are the microstructures of these DMS materials prepared by different growth techniques and growth parameters? Is there any relationship between the microstructures and Ferro magnets? What are the origins of the ferromagnetism inside the DMS materials or the nature of the magnetic coupling? Lastly, it is still a big challenge to prove or disprove that whether the ferromagnetic properties are contributed by micro magnetic clusters.

Recently, ferromagnetism in group III-V DMS materials are found only at very low temperature. This therefore prompts major effort in finding room temperature ferromagnetic semiconductors. Predictions of suitable room temperature ferromagnetic semiconductors sparked enormous effort in producing these materials. Particularly, ZnO, a cheaply available wide band gap semiconductor is a potential host material that can display room temperature ferromagnetism. Two likely dopants candidates are Manganese (Mn) and Cobalt (Co) transition metals [1, 14, 16, 18].

1.2 Objectives

To overcome the limitations and challenges in the realization of spintronics devices, group II-VI based DMS materials is one of the promising solutions. However, the origin of high temperature ferromagnetic properties of group II-VI based DMS is still under investigation, Therefore, the objectives to be achieved in this project mainly consist of the following 3 parts:

- → To fabricate and characterize cobalt doped ZnO DMS thin films on silicon substrates.
- → To investigate the role of metallic cobalt nano-clusters to the ferromagnetic properties of DMS materials, and the origins of ferromagnetism inside cobalt doped ZnO DMS materials.
- → To fabricate and characterize cobalt-doped ZnO DMS nano-structures (nanodots and nanowires) for nano devices application.

1.3 Scope

In this project, cobalt doped ZnO DMS thin films will be deposited using pulsed laser deposition technique. Deposition conditions (substrate temperature, oxygen partial pressure) will be studied. The origins of ferromagnetism in cobalt doped ZnO DMS materials will be investigated. Metal insulator semiconductor structures will be fabricated through same deposition technique. External control of ferromagnetism in DMS layers will be demonstrated. Room temperature ferromagnetic nano-structures will be fabricated and studied for their future application on spintronics devices. Both structural and magnetic properties will be characterized in this project.

1.4 Thesis Outline

The motivation and objectives of this project are presented in Chapter 1. Chapter 2 reviews some theoretical models of the spin electronic devices, and the challenges faced by the researchers currently. Different preparation methods and properties of different types of DMS materials are reviewed as well. Chapter 3 introduces the fabrication method for the DMS thin films adopted by this research and the characterization methods of these thin films. Chapter 4 presents the characterization results of these thin films. The role of metallic cobalt will be analyzed in Chapter 5. The effects of growth parameters on the properties of the cobalt doped ZnO DMS thin films will be analyzed in this chapter as well. The origins of ferromagnetic properties of cobalt doped ZnO DMS materials are investigated and discussed in chapter 6. Chapter 7 presents the nano-structures of the DMS materials which may be applied for the nano spin devices purpose. Finally, Chapter 8 concludes the report and lists the future direction and detailed works to be carried out.

Chapter 2: Literature Review

The general concept of spintronics stems from the idea of how a semiconductor works, but with the exploitation of the spin of the charge carriers incorporated. Conventional semiconductors are concerned with the type, concentration and the transportation factors of the charge carriers, while the spins of the charge carriers are now taken into consideration in spintronics. Spin is the intrinsic property of an electron. It is the intrinsic angular momentum characterized by quantum number ½. In fact, during conduction of the charge carriers, their spins are all polarized (spin polarization) in a certain direction, creating ferromagnetism in semiconductors.

The ability to spin polarized the charge carriers provides a well of new functionality of electronic and photonic devices, for example spin-valve transistors, spin light-emitting diodes, non-volatile memory, logic devices, optical isolators, ultra-fast switches and integrated magnetic/electronic/photonic devices. Furthermore, as the magnetic properties of the spintronics are related to the carrier concentration, it can be controlled electrically and optically by using field-grating transistor structures or by optical excitation to alter the carrier density.

Work on spin polarized charge carriers was pioneered by Mott in 1936 [23]. He observed that for ferromagnetic metals at adequately low temperatures, there was an absence of mixing of electrons with majority and minority spins accompanying with magnetic moment parallel and antiparallel to the magnetization of a ferromagnet. Hence the conductivity is the sum of these two kinds of spins. This phenomenon is modeled as a "two-current" model and is latter employed to explain various magnetoresistive phenomena. Magnetoresistivity is the change in the electron resistance of a material when subjected to a magnetic field.

2.1 Spintronics Devices

2.1.1 Spin Diode

Spin diodes are made of inhomogeneous two-terminal devices. The properties of spin polarization of the carriers will determine the electronic and optical properties. The schematic device geometry and band diagram of a spin LED are shown in Figure 2.1. Figure 2.1 (a) shows that under an external electric field, spin polarized electrons will be injected from the GaMnAs spin aligner, and unpolarized holes will be attracted from the p type doped GaAs layer. These spin polarized electrons and holes will recombine at the intrinsic GaAs quantum well, such that circularly polarized light would be generated. The polarization of spin electrons will determine the polarization of the light generated in the intrinsic quantum well. The GaMnAs acts as a spin aligner, which means that electrons would be aligned when electrons pass through this layer leading to a higher polarization. Electron spin is quantized, such that there are only two states of spin, which are "UP" and "DOWN". The polarization gives the properties of "net" spins, which are (SPIN UP-SPIN DOWN) / (SPIN UP+SPIN DOWN). Conduction and valence bands of a spin aligner in an external magnetic field are shown in Figure 2.1 (b). Figure 2.1 (c) sketches the corresponding band edges and band offsets in the device geometry. In the quantum well, spin-down electrons and unpolarized holes are depicted by solid and empty circles, respectively [22]. Optical methods are usually effective in detection of spin polarization light. However, in some devices, such as silicon-based diodes, optical method may not be effective enough to detect the spin polarization. In this case, electrical detection would be desired [24].

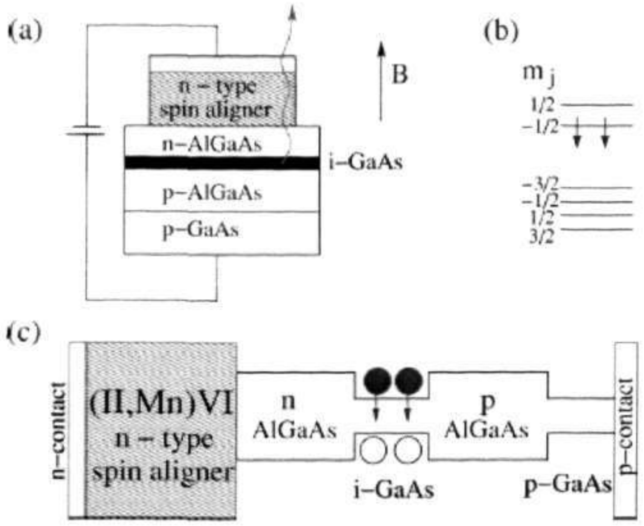

Figure 2.1 (a) Schematic device geometry, (b) conduction and valence bands of a spin aligner in an external magnetic field, and (c) band diagram of a spin LED [22].

The spin light-emitting diode shown in Figure 2.1 demonstrated the injection and detection of spins in semiconductors [22]. Previously, the spin aligner used is metallic ferromagnetic materials, such that there will be a big lattice and resistivity mismatch at the interfacial layer [25-29]. It uses a magnetic semiconductor as an injector, such that the lattice and resistivity mismatch at the interfacial layer will be significantly reduced which can lead to higher spin injection efficiency. Beside the spin light emitting diode, magnetic bipolar diode (MBD) that combines a ferromagnetic and a nonmagnetic semiconductor was demonstrated as well. It is a *p-n* junction diode. [30-32]. Both electrons and holes can be the carriers to transfer data with either the holes or electrons spin polarized. Figure 2.2 shows the schematic diagram of a MBD [32]. The left layer is *p* region and is magnetic. It has a spin split conduction band with the spin splitting known as Zeeman splitting. This splitting of conduction band is indicated by $2q\zeta$. As shown in Figure 2.2 (a) narrow band gap semiconductor would enhance Zeeman splitting. This is because in narrower band gap semiconductor, gyromagnetic ratio, which is the electron spin *g* factor, is larger. The right layer is the *n* region and is nonmagnetic. However, if there is a spin source, such as a magnetic electrode or circularly polarized light, spin polarized electrons can be generated. In Figure 2.2, filled circles indicate spin-polarized electrons and empty circles indicate unpolarized holes. Similar to the read head, if the nonequilibrium spin in both *p* and *n* regions is oriented parallel (top figure), a smaller barrier would be induced (similar to magnetic resistance), such that a higher current flows. On the other hand, if the relative orientation is antiparallel (bottom), the current would be reduced significantly [30-32].

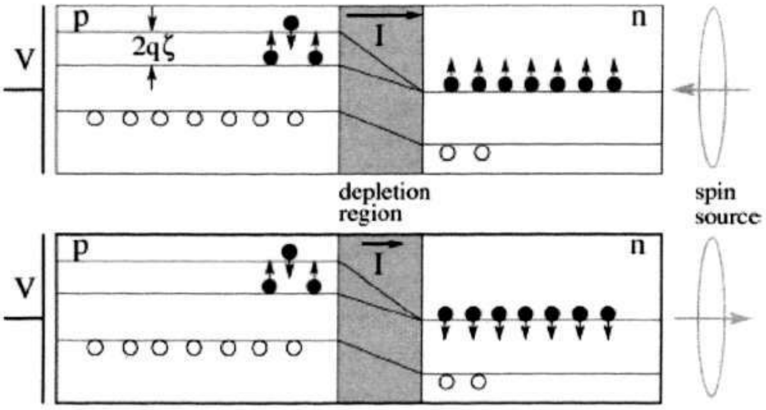

Figure 2.2 Schematic diagram of a magnetic bipolar diode [32].

2.1.2 Spin Transistor

A prototypical spintronic device scheme which is the Datta-Das spin field-effect transistor (SFET) was proposed by Datta and Das [33]. The Datta-Das SFET structure is shown in Figure 2.3. The source, which acts as a spin injector, and the drain (spin detector) are ferromagnetic metals or semiconductors, with parallel magnetic moments. External unpolarized electrons are injected into the source with the source acting as an aligner, electrons would become polarized electrons. After the electrons become polarized, the injected spin polarized electrons move ballistically along a quasi-one-dimensional channel. The current will be large if the electron spin at the drain is in the same direction as the detector, which is similar as the read head. The current will be small if the direction is reversed [33]. By using ferromagnetic source and drain, the spin injection and spin detection could be realized. The advantage of the Datta-Das SFET is that spin-dependent device operation is controlled not by external magnetic fields, but by external electric field, which controls the spin precession rate.

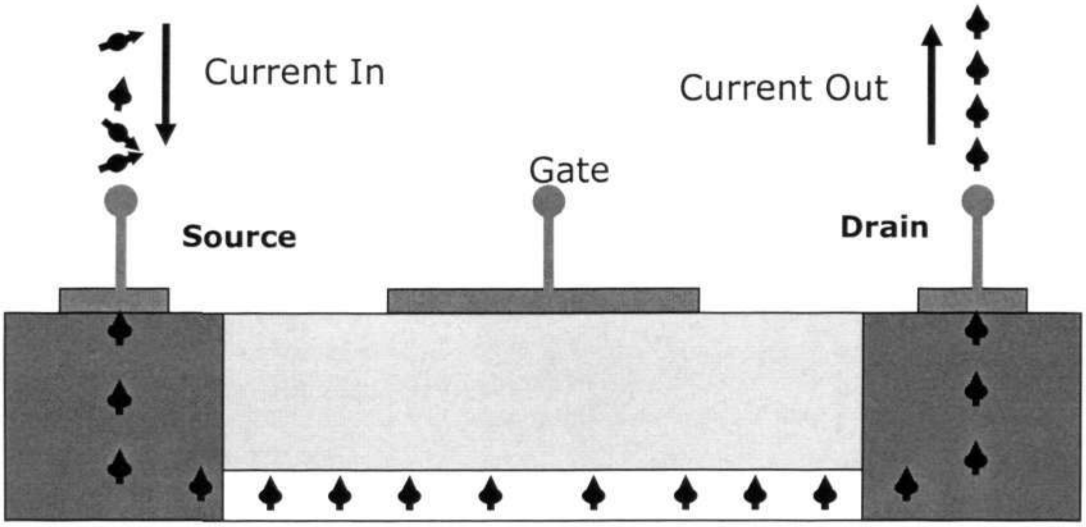

Figure 2.3 Schematic diagram of the Datta-Das spin field-effect transistor (SFET) [33].

In order to realize the proposed effect, there are at least four important challenges that need to be investigated:

(i) The efficiency of spin-polarized carriers injection from the ferromagnetic source into a 2 directional electron gas is low.

(ii) Uniform structure inversion asymmetry coefficient is required for ballistic spin-polarized transport through the channel. However, due to the interface inhomogeneities, the electric fields are not desirable.

(iii) The gate bias should have an effectively control of the structure inversion asymmetry coefficient.

(iv) The structure inversion asymmetry should be dominated. At least a half precession during the ballistic transport is required.

These four factors present a great challenge to fabricating a Datta-Das SFET at room temperature, limiting the design to special materials and very clean interfaces [34-36]. Besides the above mentioned spin devices, there are some other spin devices, such as spin valves, and magnetic bipolar transistor (MBT), which is similar to the conventional bipolar transistor [37, 38].

2.2 Dilute Magnetic Semiconductors Material

Dilute Magnetic Semiconductors (DMS) [39] is a material which exhibits both semiconducting and magnetic properties. This kind of compound as shown in Figure 2.4 (c) is an alloy between a non-magnetic semiconductor (Figure 2.4 (b)) and a magnetic semiconductor (Figure 2.4 (a)). The non-magnetic semiconductors are normally group III-V and group II-VI compounds, and the usual magnetic dopants are Mn or Co [41-43]. However, for practical application purposes, room temperature DMS materials are required.

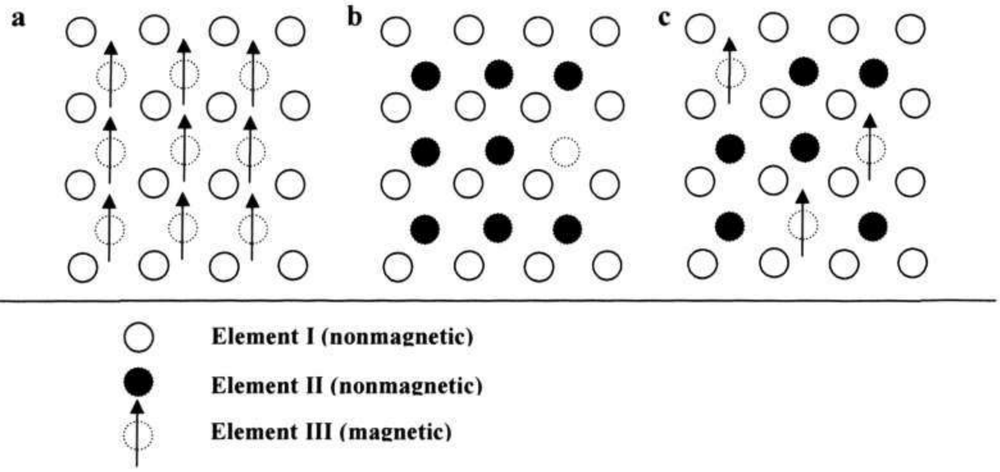

Figure 2.4 (a) Schematic diagram of different types of semiconductor: (a) a magnetic semiconductor, (b) a non-magnetic semiconductor, and (c) a dilute magnetic semiconductor [40].

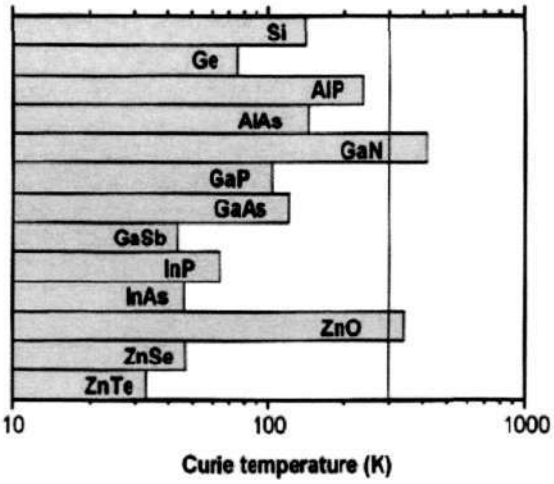

Figure 2.5: Computed values of Curie temperature for various p-type semiconductors containing 5% of Mn and 3.5 x 10^{20} hole/cm^3 [19].

A theoretical prediction by Dietl *et. al* [19] indicated that the Curie temperature can be increased above room temperature in p-type doped DMS as shown in Figure 2.5. From this figure, we observe that room temperature ferromagnetism is stable in ZnO DMS, which is a wide bandgap and group II-VI semiconductor. This theoretical simulation was done by *ab initio* calculations based on the local density approximation, and is the first step towards the realization of DMS.

2.3 Origins of Magnetic Properties in DMS

Before we highlight some of the experiments carried out by other research groups, we first discuss on the theoretical models that are most commonly used to describe the magnetic interactions in DMS. These models, such as the double exchange interaction, indirect interaction and super exchange interactions, describe the mechanisms of ferromagnetic or anti ferromagnetic interaction. However, the actual magnetic properties of the DMS depend on the details of their chemical bonding, crystal structure, defects structure, magnetic dopant concentrations, carrier concentrations, preparation method, etc.

2.3.1 Exchange in Insulators

2.3.1.1 Direct Exchange

The exchange interaction coupling the spins s_i of localized electrons in an insulator is called the direct exchange interaction, which can be described by using the Heisenberg Hamiltonian which is shown in equation (2.1) [44, 45].

$$H_{ex} = -\sum_{ij} J_{ij} s_i \cdot s_j \tag{2.1}$$

From this Hamiltonian, the sign of the exchange integral J_{ij} will give a clear indication of the magnetic properties of the system. If the two states coupled by the exchange integral J_{ij} are electronic states in a free atom, then the value of the exchange integral J_{ij} tends to be positive. This implies that the spins are aligned parallel, such that ferromagnetism will occur, and this is reflected in the Hund's rules. If the exchange interaction is between electrons which are localized on different neighboring atoms, the exchange integral J_{ij} tends to be a negative. This implies that the two electrons are aligned anti-parallel. Because of this anti-parallel alignment, a bonding state will form, and anti-ferromagnetic properties will result. If a solid has unpaired electrons, the sign of exchange integral J_{ij} can be either positive or negative in principle. However, the dominating part is typically the negative side, which leads to anti-ferromagnetic alignment of the neighboring spins.

2.3.1.2 Super Exchange

Super exchange mechanism is a kind of magnetic coupling normally found in group II-VI compounds, or those compounds related to group II-VI elements. This is because in many transition metal oxides and related materials, such as ZnO and TiO_2, the magnetic interaction between the transition metal ions (Zn or Ti) are mediated by the intermediate anions oxygen. Normally the *p* orbital of oxygen acts as an intermediate, and this coupling is sometimes known as *p-d* interaction, which is short-ranged. This kind of interaction can also be described by a Heisenberg Hamiltonian. From the semi-empirical Goodenough-Kanamori_Anderson (GKA) rules [44], factors that affect the sign of J_{ij} are the metal-oxygen-metal bond angle, and the *d* electron configuration on the group II transition metals.

2.3.2 Carrier Mediated Exchange

Carrier mediated exchange is another type of magnetic coupling for localized magnetic moments. This type of coupling occurs with the help of free carriers in the system, which means the free carriers are intermediates for the localized magnetic moments. Here free carriers do not mean that they are exactly free, with zero force constraint. In group II-VI base DMS, defects are easily formed in the system, this will results in some free carriers generated. In this review, three limiting cases for carrier mediated exchange are described below.

Ruderman-Kittel-Kasuya-Yosida (RKKY) interaction

RKKY [46] is the first theory used to explain the magnetic properties inside DMS materials. In this theory, it describes the magnetic exchange between a single localized magnetic moment and a free electron gas, such that it can be exactly treated by quantum mechanics. The exchange interaction *J* is shown in equation (2.2). The sign of *J* can be shown that it oscillates with a distance from the localized magnetic moment *R*, and the density of electrons in the free electron gas. If the *J* value is negative, it shows that the localized magnetic moments are aligned anti-parallel, which results in anti-ferromagnetic properties. If it is aligned parallel, it will generate ferromagnetism inside the DMS materials.

$$J(R) = \frac{m^* k_F^4}{\hbar^2} F(2k_F R) \tag{2.2}$$

Where m^* is the effective mass, $\hbar$ is the Planck constant, and k_F is the Fermi wave vector of the electron gas. Here the *F* function is the oscillating function as shown in equation (2.3), and it is plotted in Figure 2.6.

$$F(x) = \frac{x\cos x - \sin x}{x^4} \tag{2.3}$$

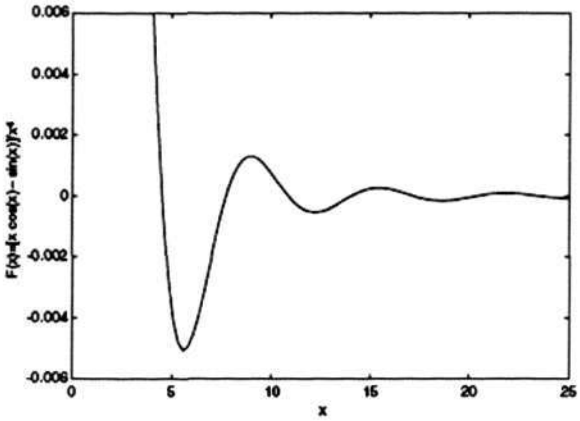

Figure 2.6: The oscillatory part of the RKKY interaction energy, x is proportional to the product of the Fermi wave vector k_F and the distance R from the localized moment [46].

Zener carrier-mediated exchange [47]

In some DMS materials, they may be doped with some extrinsic materials. In such a system, it may have both some itinerant carriers and localized magnetic moments. These itinerant carriers can mediate a ferromagnetic interaction between the localized magnetic moments, known as Zener carrier mediated exchange. In this system, the spin sub-bands can be split apart and redistributed because of the exchange interaction. As a result, the carriers' energy is lowered, and the ferromagnetic ordering is driven by the lowering of the carriers' energy.

Zener double exchange [49]

This is similar to the super exchange mechanism, with the only difference in the involvement of carriers. This model was first proposed to explain the ferromagnetism which was observed experimentally in the doped perovskite structure manganites $La_{1-x}A_xMnO_3$, where A can be Ca, Sr, or Ba, and $0 < x < 1$ [49]. Inside this system, Mn has two valance states, one is Mn^{4+}, and the other one is Mn^{3+}. There are four and three electrons in the *3d* orbitals of Mn^{3+} and Mn^{4+} respectively. The kinetic energy of the system is lowered if the magnetic moments align in parallel, and the parallel alignment can allow electron transfer from Mn^{3+} to Mn^{4+}. This coupling is indirect, which is mediated by the oxygen atoms between neighboring Mn^{3+} to Mn^{4+} ions.

The above-mentioned are three possible mechanisms for carrier mediated exchange. However, in a real system, they may exhibit characteristics of two or all the models depending on the actual samples.

2.3.3 Bound Magnetic Polarons

The previous two theories proposed are for short range interactions. However, in some DMS materials, the concentration of magnetic doping is very small, such that long range magnetic order can not be explained by the models. Here, we discuss another model which can explain long range interactions, which is Bound Magnetic Polarons (BMP) [50]. It has been shown that in dilute magnetic semiconductors, the ferromagnetic exchange is mediated by shallow donor electrons which form bound magnetic polarons, and these polarons overlap to create the spin split impurity band. For example, the general formula for oxides is $(A_{1-x}M_x)$ $(O\square_{\delta})_{n,}$ where A is the non-magnetic cation, M is a magnetic cation, and □ represents a donor defect. The defect associated with one electron will be confined in a hydrogenic orbital of a certain radius. Initially, the electron is bonded inside the *1s* orbital. When the donor defect concentration δ increases, the *1s* orbital radius will increase and result in an overlap to form an impurity band. If it reaches above a critical concentration of the donor defects, delocalized impurity band states may result. If the magnetic cations M interact with the hydrogen-like electrons in the impurity bands, the donors will tend to form magnetic polarons, which couple the *3d* moments of the ions with their orbits [50-54]. The basic idea of magnetic polarons is shown in Figure 2.7.

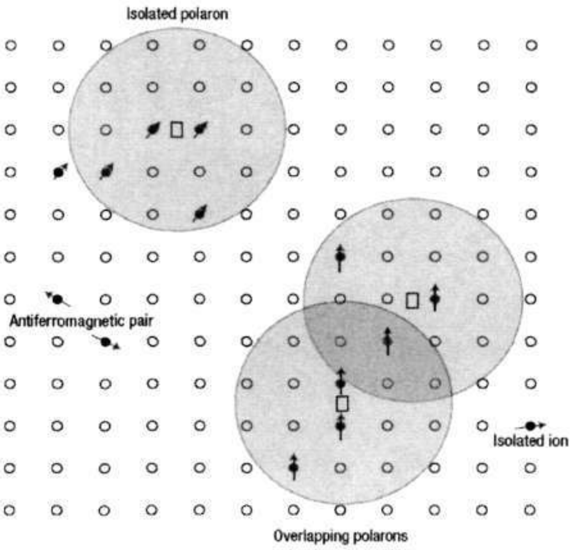

Figure 2.7: Schematic diagram of magnetic polarons. Small circle is the cation sites, while squares represent oxygen vacancies [50].

Because magnetic cations present an extra random potential, if the amount of magnetic cations increases, the localized region will be extended which can result in a sufficiently large radius of its orbital. In this case, the coupling between the cation and the donor electron is ferromagnetic when the *3d* shell of M is less than half full, and anti-ferromagnetic when the *3d* shell of the M is half full or more.

When the concentration of defects increases, the hydrogenic orbitals associated with the randomly positioned defects overlap. This results in a percolation threshold for the appearance of long range ferromagnetic order, which is temperature dependent [55].

Two thresholds are identified. One is donor polaron percolation, δ_p, and the other is the magnetic cation percolation threshold x_p. These two thresholds play important roles in the magnetic properties of DMS, as shown in Figure 2.8.

From this phase diagram, ferromagnetism occurs when $\delta > \delta_p$ and $x < x_p$. Anti-ferromagnetism or ferrimagnetism results when $x > x_p$. This is because when the concentration of cations becomes larger, there are continuous paths throughout the crystal joining the nearest neighbor magnetic cations. However, if x is small enough, the super-exchange which resulted in anti-ferromagnetic property will not create long range order. If the doping of M is not uniform, such that there are some small areas which have super-exchange, this will lead to anti-ferromagnetic clusters which can reduce the magnetic moment per cation.

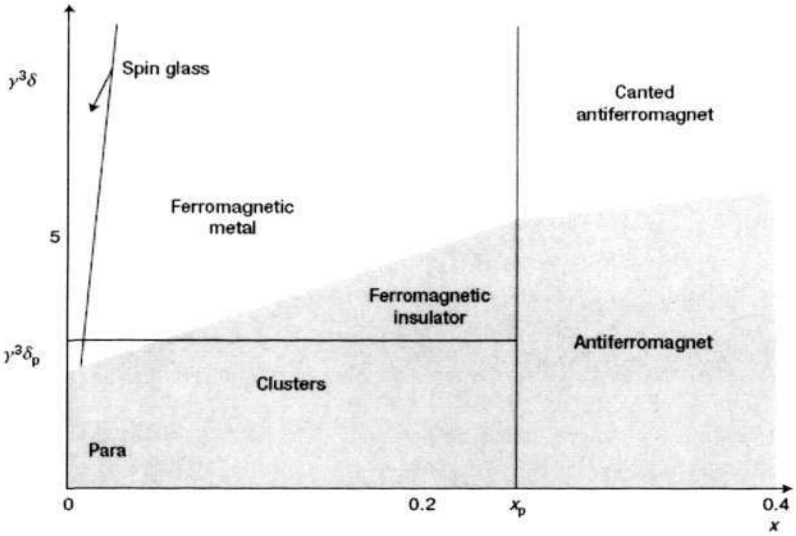

Figure 2.8: Magnetic phase diagram of DMS [50], x_p is the cation polaron percolation thresholds, δ_p is the donor polaron percolation thresholds, and γ is the ration of the radius of the hydrogenic donor orbital to the Bohr radius.

2.4 ZnO Based DMS

So far, group III-V and group II-VI are the most popular candidates for the host material of DMS. However, the Curie temperature of group III-V DMS is still below room temperature [56-61], while group II-VI room temperature DMS has been reported in recent years [18,20,62-68].

2.4.1 Experimental Results of Transition Metal doped ZnO

Transition metal doped ZnO based DMS has attracted much interest in the world, and this is due to the prediction that doped ZnO is a promising candidate for the realization of high temperature Curie temperature DMS [19,41,69]. ZnO is a wide bandgap semiconductor with *Eg* around 3.3 eV at room temperature. It has a hexagonal wurtzite structure (space group- P 63 m c) (Figure 2.9).

It has a formula weight of 81.369 g/mol with lattice constants of a = 3.2Å and c = 5.2 Å at 298 K with a unit cell volume of 47.6 Å^3. Due to the defects (*i.e.* oxygen vacancies, zinc interstitials) that have formed inside ZnO, it is very easy to form *n*-type ZnO. At the same time, *n*-type ZnO can also be achieved easily by using extrinsic doping, such as Al, Ga or In. With group III substitution doping, high electron carrier density can also be realized. However, to achieve a *p*-type ZnO is still a big challenge, although recently Tsukazaki *et. al* reported *p*-type doping by N in ZnO layers grown on high quality ZnO [70, 71]. According to the prediction made previously [19], the dominant mechanism of room temperature ferromagnetism in ZnO based DMS is hole mediated. Thus *p*-type ZnO can be a potential candidate as host material and doped with transition metal for spintronics devices.

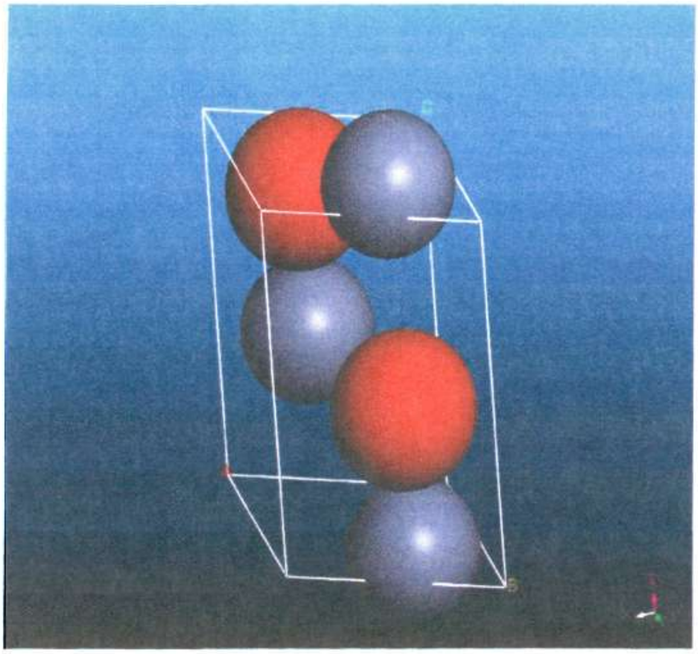

Figure 2.9: Crystal structure of ZnO, The red ball represents Oxygen atom while the grey ball represents zinc atom.

Mn-doped ZnO films were deposited by pulsed laser deposition method by Fukumura *et. al* in 1999 [72]. In this group's investigations, 35% of Mn dopants were added inside the ZnO without affecting the crystallographic quality of the DMS much. XRD result was not shown in this report, so further scrutiny is needed. In this report, the solubility of Mn was quite high, and this may be expected in ZnO host owing to Mn^{2+} nature, which can be achieved easily with the $4s^2$ electrons participating in the bonding process. *4s* electrons are much closer to the oxygen atom, and the oxygen atom lacks 2 electrons in its *2p* shell. Mn^{2+} has half filled *3d* shell, so it will cost a considerable amount of energy to add an electron with the opposite spin to the *3d* orbit of Mn. Thus, Mn behaves in much the same manner as Zn, which means that Mn substitutes Zinc cations. Because of this similarity, Mn has a high solubility in ZnO. However, future investigations are also required, as the atomic size of Zn is relatively larger than Mn, and the Mn solubility in ZnO should be constrained by this factor.

Because of the reported high solubility of Mn in ZnO [72], a lot of interest was generated in fabricating transition metal doped ZnO DMS by using various thin film deposition techniques. A large number of studies on ZnO doped with various kinds of transition metals have been reported, although Mn may not be electronically conducive to ferromagnetism in ZnO. The thin film growth techniques of these ferromagnetic materials are normally molecular beam epitaxy (MBE), metal-organic chemical vapor deposition (MOCVD), and pulsed laser deposition (PLD). These techniques provide excellent control of the dopant concentration and the quality of crystal structure for the thin layers. However, what is the magnetic behavior of the ZnO based DMS and their origin are still rather controversial. While some groups have reported ferromagnetism in (Zn,TM)O systems with T_c ranging from 30 to 550 K [20,65,73-79], others have reported that the magnetic properties are antiferromagnetic and spin-glass behavior [80-85]. The type of transition metal doped inside the host ZnO is also an issue that needs to be addressed.

However, for DMS which can be applied for spintronic devices, it refers to the fact that some fraction of the atoms in the non-magnetic semiconductor host, such as Zinc cations inside ZnO to be replaced by magnetic ions. An important question which almost all researchers are concerned with is whether the magnetic ions are indeed located at the host cations site, and if they are uniformly distributed, or have formed clusters, precipitated or formed second phases which are responsible for the magnetic properties observed. Table 2.1 summarizes recent reports of magnetic properties of transition metal doped ZnO.

The probable reason for the controversy in the magnetic properties of ZnO-based DMS may be due to the inadequate characterization techniques available for the samples. In the theoretical understanding, the origins of magnetic behavior inside a DMS material are complex and appear to depend on a number of factors, such as magnetic cation to magnetic cation space, the carrier density and types. These factors will affect the band structure and electronic properties of the DMS materials, which may result in different magnetic properties. At the same time, the sample preparation procedure may be different, such as the type of equipment used, pressure controlled, deposition temperature, or any precursors used. Thus, it is necessary to study each case differently, and assign the correct mechanism or mechanisms to the particular case. This can only be achieved by a careful correlation of the measured magnetic properties, with the use of characterization method, in that whether it is capable to detect other phases or precipitates. Furthermore, if the magnetic properties of the samples are quite weak, more magnetic and temperature sensitive measuring equipment such as SQUID is also needed. Table 2.2 lists some second phase precipitates which were reported in TM-doped ZnO.

Table 2.1: Summary of recent reports for DMS

Compound	TM content	Substrate (for thin film) or bulk	Fabrication Method	Growth Temp (^{o}C)	Oxygen pressure (Torr)	TC (K)	Notes	Reference
(Zn,Mn)O	<0.35	*c*-sapphire	PLD	600	5×10^{-5}			[72]
(Zn,Mn)O	0.36	*c*-sapphire	PLD	600	5×10^{-5}		Spin glass	[81]
$Zn_{1-x}TM_xO$		*c*-sapphire	PLD	500-600	1×10^{-9} to 10^{-6}			[82]
(Zn,Mn)O	0.01~0.36	*c*-sapphire	PLD	610	5×10^{-5}		paramagnetic	[83]
(Zn,Mn)O	0-0.3	*c*-sapphire	PLD			>30-45	0.15-0.17 μ_B/Mn	[73]
(Zn,Mn)O	<0.04		Sintered pellets	500-700	Air, 1 atm	>425	0.16 μ_B/Mn	[20]
(Zn,Mn)O	0.0221	Fused quartz	PLD	400	0.2	>425	0.05 emu/g single phase	[20]
(Zn,Mn)O	0.04-0.09	*c*-sapphire	Reactive sputtering	200-380		>400	3 μ_B/Co	[86]
(Zn,Mn)O	0.07	*a*-sapphire	Sputtering	400	0.06		paramagnetic	[87]
(Zm,Mn)O	0.03 & 0.2	GaAs (001)	sputtering	500 - 600	8×10^{-4} in Ar			[21]
ZnO:(Mn,Sn)	0-0.3		Implantation			250	Ferromagnetic	[74]
ZnO:(Mn,Sn)	Mn 0.03 Sn <0.1	*c*-sapphire	PLD	400-600	0.02	>300	ferromagnetic	[79]
ZnO:(Co, Mn, Cr,or Ni)	0.05~0.25	*c*-sapphire	PLD	350-600	$2\text{-}4 \times 10^{-5}$	280-300	2 μ_B/Co	[77]
ZnO:(Mn,Co)	0.02 –0.15		Crystalline precursor				antiferromagneteic	[84]
ZnO:(Mn,Co)	<0.05		Melt-growth				paramagnetic	[85]
(Zn,Co)O	0.03-0.05	bulk ZnO	Ion implantation			>300	Co nanocrystals	[90]
(Zn,Co)O	0-0.25	*c*-sapphire	Sol-gel	<350		>350	0.56 μ_B/Co	[74]
(Zn,Co)O	0.015		PLD	650	5×10^{-5}	>300	Ferromagnetic	[91]
ZnO:(Co, Al)	0.04-0.12	Glass	rf sputtering		1×10^{-2} in Ar	>350	0.21 μ_B/Co	[92]
(Zn,Co)O	0.02~0.5	*c*-sapphire	PLD	300-700	1×10^{-6} to 10^{-1}		Spin glass	[80]
ZnO:Co	0.1	O face ZnO	PLD				Antiferromagnetic	[93]
ZnO:Co	<0.35	*r*-sapphire	MOCVD	300-650	40	>350	ferromagnetic	[94]

To be continue

Table 2.1 continue

Compound	TM content	Substrate (for thin film) or bulk	Fabrication Method	Growth Temp (oC)	Oxygen pressure (Torr)	TC (K)	Notes	Reference
ZnO:(Co, Fe)	<0.15	SiO2/Si	Magnetron sputtering	600	2×10^{-3}	>300	12-15 emu/cm^3	[75]
ZnO:(Cu,Fe)	Fe < 0.07 Cu < 0.01	Bulk	Solid-state reaction	897		550	0.75 μ_B/Fe	[76]
(Zn,Ni)O	0.01-0.25	*c*-sapphire	PLD	300-700	1×10^{-5}		Super para-or	[78]
(Zn,V)O	0.05-0.15	*r* - sapphire	PLD	300	10^{-5} to 10^{-3}	>350	0.5 μ_B/Co	[79]
ZnO:Mn	0.1	*r* - sapphire	PLD	650	0.1		0.075 μ_B/Mn	[95]
ZnO:(Mn,Cu)	Mn 0.1, Cu 0.05	*r* - sapphire	PLD	650	0.1	400	0.1 μ_B/Mn	[95]
ZnO:(Sc, Ti, V, Fe, Co, Ni)	0.05	*r* - sapphire	PLD	600	0.1 to 750	>300	2.6 μ_B/Co 0.5 μ_B/Ti 0.3 μ_B/Sc	[88]
ZnO: Mn ZnO:Co	0.002		Sol-gel	145		>300	1.3 μ_B/Mn	[96]
$Zn_{1-x}Mn_xO$	X = 0.02, 0.03, 0.05		Solid-state reaction	500	air		paramagnetic	[97]
Co^{2+}:ZnO			Sol-gel			300	ferromagnetic	[98]

Although X-ray diffraction measurements play an important role in detecting any impurity phases, its sensitivity may not be good enough to identify all precipitates in the samples. This is because the amount of magnetic dopants is quite small, and the precipitates will be even much smaller. A small amount of these clusters or precipitates is sufficient to create the magnetic properties which are observed by some of the measurement equipment. Thus, other characterization techniques are needed, such as Scanning Electron Microscope (SEM), Reflection High Energy Electron Diffraction (RHEED), Transmission Electron Microscope with High Resolution and Diffraction pattern (TEM), Electron Probe Microanalysis (EPMA), and Secondary Ion Mass Spectrometry (SIMS).

Table 2.2: Reported second phases in TM-doped ZnO by different characterization method

Phase	**Nature of magnetism**	**Curie temperature or Neel temperature(K)**	**Reference**
Mn-O-Mn cluster			[106]
MnO	Anti-ferromagnetic	116	[73]
MnO_2	Anti-ferromagnetic	92	[97]
Mn_2O_3	Anti-ferromagnetic	76	[97]
Mn_3O_4	Ferromagnetic	43	[97]
Mn_3O_4 (distorted spinel)	Ferrimagnetic	46	[99]
Mn_3O_4 (Hausmannite)	Ferrimagnetic	40	[100]
$(Zn,Mn)Mn_2O_4$	Ferrimagnetic	40	[101]
$ZnMnO_3$ (cubic)	Spin-glass		[102]
Zn_3MnO_6 (hexagonal)			[102]
Co	Ferromagnetic	1373	[90]
CoO	antiferromagnetic	291	[77][103]
CuO (monoclinic)	antiferromagnetic	230	[104]
Cu cluster	antiferromagnetic	154	[104]
FeO (cubic)			[76]
$(Zn, Fe)_3O_4$	Ferromagnetic	440	[103]
$ZnFe_2O_4$ (bulk)	Nonferromagnetic		[105]
$ZnFe_2O_4$(invert spinel)	Ferromagnetic		[105]

X-ray photoemission scanning (XPS) may also be used to identify clusters which may be in the nano scale. At the same time, the uniformity of dopant distribution in the host material needs to be investigated. Fukumura *et. al* gave a detailed review of the characterization techniques for oxide-based DMS [107], but pointed out another factor which can affect the results. In the case of magnetic measurement of a thin film on a substrate, the measured signal, which is in proportion to the sample volume, includes the magnetic moment not only from the film but also from the substrate (which is in general diamagnetic) owing to the much larger volume of substrate than that of film (normally the thickness of substrate is much larger than the thickness of the thin films). Therefore, the magnetic properties analysis must be done carefully, and taking note the contribution from the substrate, which can mask completely the real signal from the DMS thin films. If the magnetic moment per magnetic ion in the sample is calculated, it would be much more useful. Despite the controversy surrounding the origin of ferromagnetism in ZnO-based DMS reported in the literature, the experimental results of cobalt doped ZnO will be discussed in the following section.

2.4.2 Properties of Co-doped ZnO

Initially, the existence of ferromagnetic property in Co-doped ZnO samples has been theoretically assigned to the double exchange interaction [41,108] or the RKKY interaction between Co ions [109]. However, a calculation later showed that the ground state of Co-doped ZnO is spin glass due to the short range interactions between transition metal atoms [110]. In order to verify the predictions, experimental studies have been carried out. Ueda *et al* investigated $Zn_{1-x}TM_xO$ films [*n*-type (x = 0.05 – 0.25) and TM=Co, Mn, Cr, Ni] grown on *c*-sapphire substrates by using the PLD technique [77]. The maximum solubility limit of the Co-doped ZnO films is around 50%. It is the first group to report room temperature ferromagnetic ordering in $Zn_{1-x}Co_xO$. However, the reproducibility of the sample was extremely low. Further XRD, TEM and magnetic circular dichroism (MCD) measurements on these samples showed ferromagnetic metal behavior, which indicates that the observed ferromagnetism may have originated from Co-related ferromagnetic precipitates (cobalt clusters) [104]. The ferromagnetism observed in (Zn,Co)O fabricated by ion implantation of Co into (110)-oriented Sn-doped ZnO substrates has also been shown to be due to the Co nanoclusters inside the samples prepared [90]. In a systematic study of magnetism in TM-doped (from Sc to Cu) ZnO, Ventatesan *et. al* reported that the magnetic moment of Co, 1.9 μB per Co, is the largest among all other transition metal elements in (Zn,TM)O with 5 % of TM, as reported in Figure 2.10 [88].

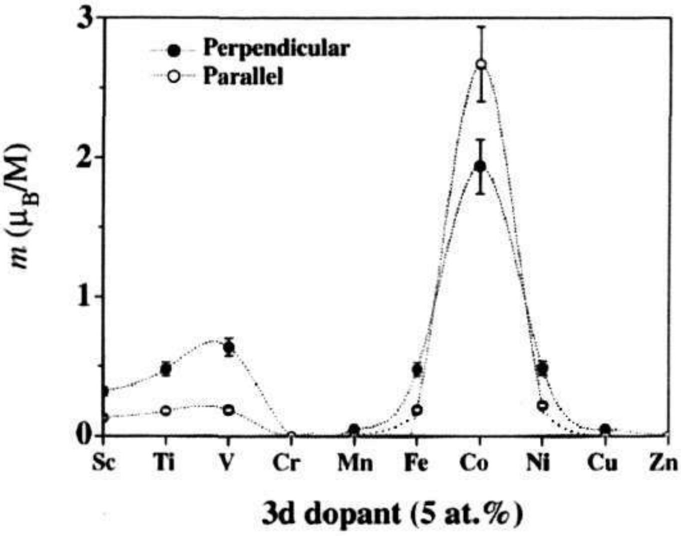

Figure 2.10: Ms for different TM doped ZnO at 5% atomic % [88].

The films were grown by PLD on *R*-cut sapphire substrates. Lee *et. al* reported that $Zn_{1-x}Co_xO$ with x = 25% fabricated by sol-gel method exhibits ferromagnetic behavior with T_C higher than 350 K [74]. The film is insulating with n-type carrier concentration in the 10^{17} cm^{-3} range. In samples with x = 20 and 25%, both magnetization and carrier concentration increase with temperature. It is argued that a higher Co concentration could enhance the "trapping" of the electrons, which may induce the ferromagnetic spin-spin interaction between Co atoms. The peculiar increase of magnetization with temperature is similar to what was reported for Mn-doped ZnO by Heo *et. al*, which has been explained by the effect of randomness and disorder on percolating FM clusters [111]. Tuan *et. al* grew epitaxial $Zn_{1-x}Co_xO$ (x < 35%) films on *R*-cut sapphire by MOCVD, and a weak ferromagnetic behavior persists even above 350 K [94]. The conductivity was observed to reduce with post-growth annealing in vacuum instead of Al-doping. The increase in the saturation magnetization with conductivity or carrier concentration observed in these reports seem to agree with some theoretical predications that electron doping is necessary to induce ferromagnetism in (Zn,Co)O [74,94,110]. Several other groups have also reported the observation of ferromagnetism in (Zn,Co)O with 10 to 40 % of Co [91,112,113]. On the other hand, just like Mn-doped ZnO, there are many reports about the absence of ferromagnetism in Co-doped ZnO as well. Kim *et. al* reported spin-glass behavior for homogeneous $Zn_{1-x}Co_xO$ films and room temperature ferromagnetism was found only in inhomogeneous films, which led the authors to attribute their observations to the presence of Co clusters [63]. Kane *et. al* investigated bulk $Zn_{1-x}Co_xO$ and $Zn_{1-x}Mn_xO$ fabricated by a melt-growth method, and found no evidence of ferromagnetic behavior in any of these nominally non carrier-doped samples which can be explained by diluted magnetic semiconductor mean-field [68].

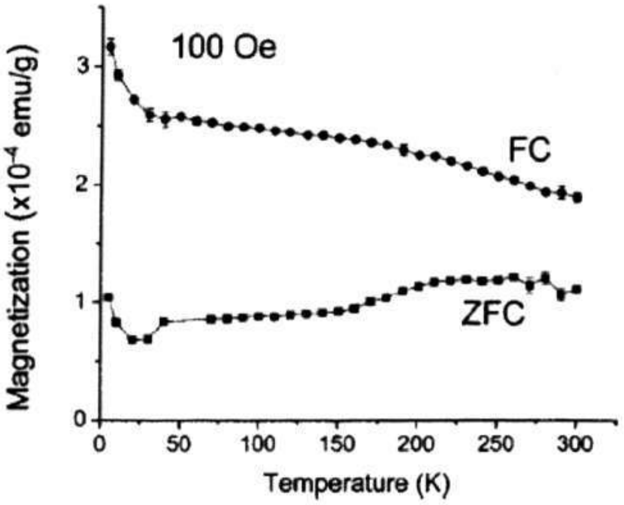

Figure 2.11: Difference in the field-cooled (FC) and zero-field-cooled (ZFC) magnetization vs. the temperature plots taken at 100 Oe for $Zn_{1-x}Co_xO$ (x=0.01) sample. Note that the extrapolated slopes versus the temperature are of opposite signs in the ZFC and FC curves and there is a significant deviation in these two values. This indicates a super paramagnetic cluster-type behavior [68].

The magnetic properties showed paramagnetic behavior for $Zn_{1-x}Mn_xO$ dominated by an anti-ferromagnetic Mn–Mn exchange interaction at low temperatures [68]. Although $Zn_{1-x}Co_xO$ showed ferromagnetic properties, the zero field cooling (ZFC) and field cooling (FC) magnetization, which is shown in Figure 2.11, revealed that the hysteresis was due to nanoscale paramagnetic Co clusters embedded in a diamagnetic ZnO matrix. The authors concluded that in the bulk single-crystal form, intrinsic and non carrier-doped $Zn_{1-x}TM_xO$ is not ferromagnetic, thus creative processing and doping techniques are necessary to achieve practical ferromagnetism in these materials. Paramagnetic behavior has also been observed to be dominant in polycrystalline $Zn_{1-x}Co_xO$ ($x < 0.15$) and bulk $Zn_{1-x}Co_xO$ ($x < 0.1$) [67,114].

Consistent with some theoretical predications, Lin *et. al* argued that additional Cu doping into bulk $Zn_{0.98}Co_{0.02}O$ grown by standard solid-state reaction method is essential to achieve room-temperature ferromagnetism [115,116]. Cu can be doped up to 1 % ($Zn_{0.97}Cu_{0.01}Co_{0.02}O$) without forming a secondary phase as confirmed by HRTEM. The saturation magnetization at 300 K increased with Cu concentration as shown in Figure 2.12. Photoluminance showed increasing peak intensity was at 518 nm, which was attributed to the defects in ZnO due to the incorporation of Cu and Co, but the UV emission peak diminished with Co or Cu with Co co-doping.

Substitution of cobalt cations in the tetrahedral sites of the wurtzite structure was confirmed by optical spectroscopy. In its neutral charge state, the Co^{2+} ion has an [Ar] *3d7* electron configuration. The atomic 4F ground state splits under the influence of the tetrahedral component of the crystal field into a 4A2 ground state and 4T2 + 4T1 excited states. The smaller trigonal distortion and spin-orbit interaction split the ground 4A2 state into E1/2 + E3/2. The existence of the Co^{2+} oxidation state has been verified by a series of characteristic optical absorption bands in both the infrared and visible bands that have been correlated to *d-d* transitions of the high-spin Co^{2+} *3d7* (4F) ions in the tetrahedral oxygen coordination. The absorption in the visible band was thought to derive from the

4A2 (4F) →2E (2G) and 4A2 (4F) →4T1 (4P) transitions, and those in the infrared from the 4A2 (4F) → 4A1 (4G) transition [103]. These d – d adsorption levels of Co^{2+} ions have been reported to be around 570, 620, and 660 nm, which corresponds to 2.18, 2.00, and 1.88 eV, respectively [60,68,112,113,117,118].

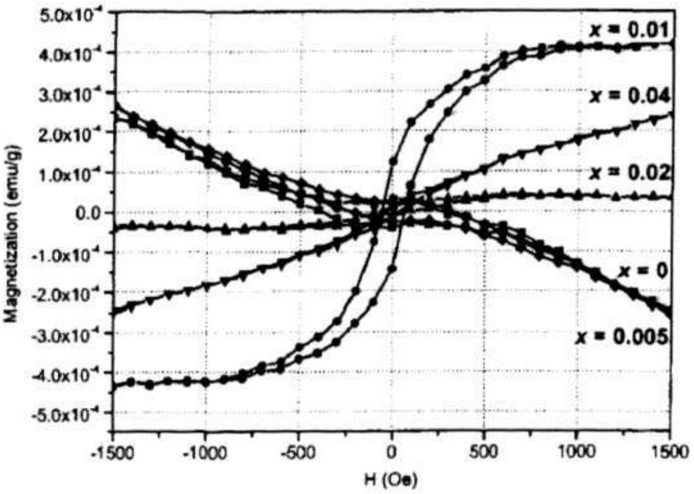

Figure 2.12: Hysteresis curves measured at room temperature of bulk $Zn_{0.98-x}Cu_xCo_{0.02}O$ samples [116].

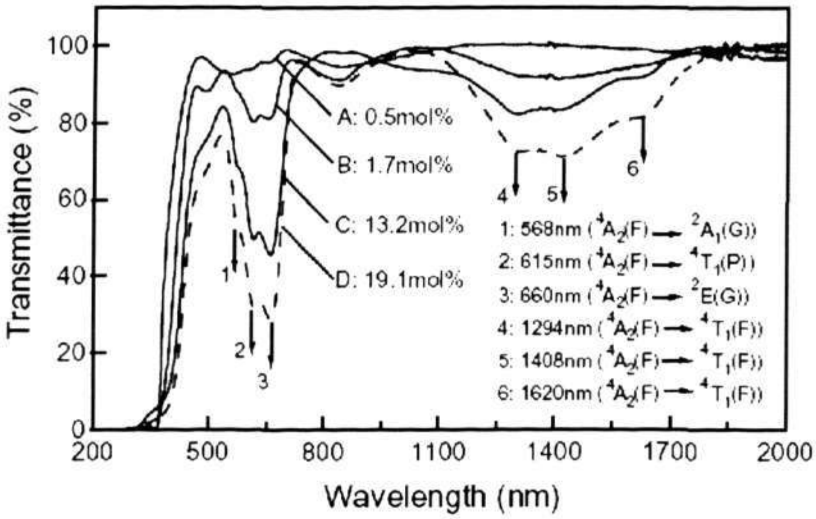

Figure 2.13: Optical transmission spectrum of $Zn_{1-x}Co_xO$. The assignment of the absorption peak is also shown. The dashed line corresponds to the sample showing the solubility limit [118].

Figure 2.13 shows the optical transmission spectrum for $Zn_{1-x}Co_xO$ with x = 0.05

to 0.19 [118]. The evidence of Co^{2+} state in ZnO lattice has also been obtained from EPR [93] and XPS [94] measurements.

2.5 Summary

In summary, it is not an overstatement that the expected advantages of ZnO-based spintronics are truly exciting although the efforts in materials science and devices are still in their embryonic stage. However, there are many challenges which have to be addressed, including whether high ferromagnetic transition temperature (for high temperature working devices) and carrier-mediated ferromagnetism (for controlling ferromagnetism) can be realized. In addition to a ferromagnetic semiconductor, successful operation of spintronic devices also requires the support of spin-polarized transport in the device and the amplification and detection of spin polarization (or spin current). With accelerated research efforts towards room temperature ferromagnetism in ZnO and other oxides based DMS materials, it might be possible to realize semiconductor magneto electronics. Perhaps the "real" utilization of the spin degree of freedom is spin-based all-semiconductor multifunctional devices such as spin-FETs, spin-LEDs, spin resonant tunneling device (RTD), sensitive magnetic sensor, high density nonvolatile memory, and quantum bits for quantum processing.

Chapter 3 Experiment Details

This chapter presents an overview of the synthesis methods for the growth of DMS thin films, nanodots and core-shell nanowires by pulsed laser deposition (PLD), and the characterization techniques employed in this research.

3.1 Pulsed Laser Deposition

3.1.1 Deposition Chamber

DMS thin films, nanodots and core-shell nanowires were synthesized in a high vacuum stainless steel deposition chamber. The deposition chamber was first pumped with a diffusion pump to achieve a base pressure of 4×10^{-7} Torr. Pure O_2 (99.99%) was then introduced slowly into the deposition chamber. By controlling the gas flow rate introduced into the chamber, the deposition pressure could be adjusted. Typically, the chamber pressure was maintained between 5×10^{-7} to 5×10^{-3} Torr during the growth of the DMS thin films, nanodots or core-shell nanowires. The chamber has a quartz window through which the focused laser beam is able to pass through. The laser beam is incident on a rotating target with a loss of less than 20%, as there is an antireflection coating film on the surface of this window. The angle between the incident laser beam and normal to the target surface was 45°. The deposition time ranged from 40-80 mins. A schematic and photograph of the deposition chamber are shown in Figure 3.1 and Figure 3.2, respectively.

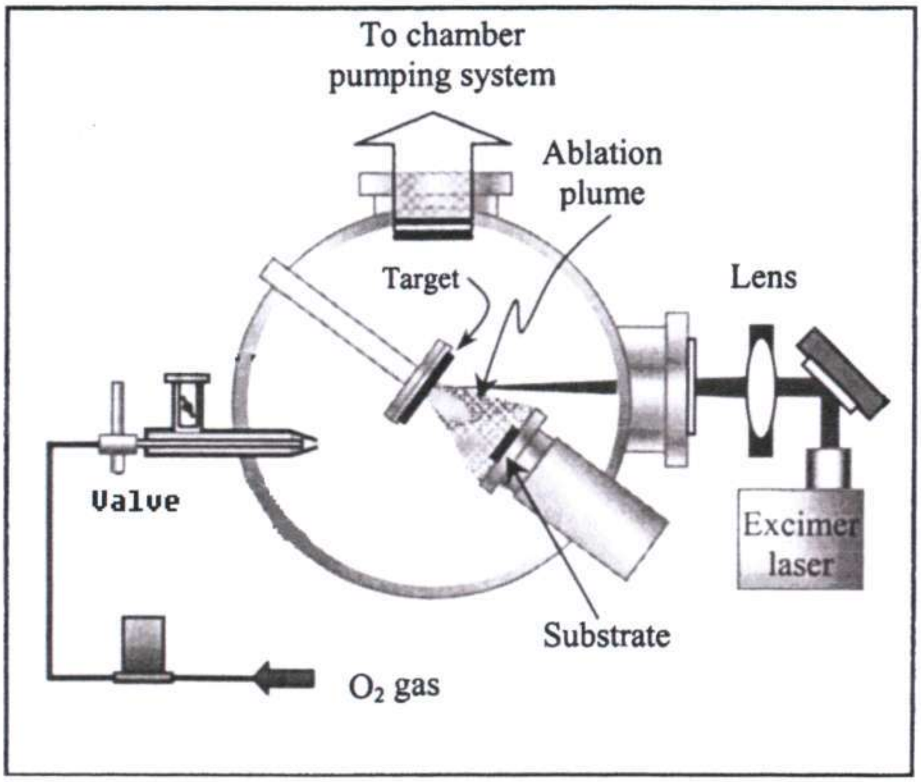

Figure 3.1 Schematic of a Pulsed laser deposition system.

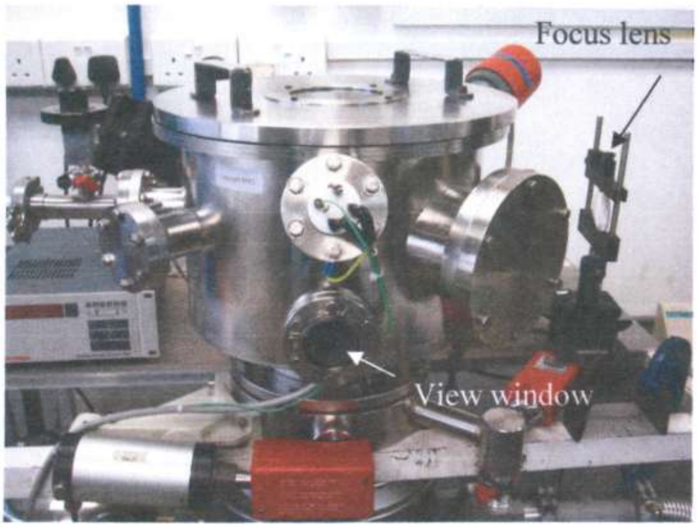

Figure 3.2 Photograph of the pulsed laser deposition chamber.

3.1.2 Laser

A KrF excimer laser (LAMBDA PHYSIK, Compex Pro 102) operating at a wavelength of 248 nm and frequency of 10 Hz was used to irradiate the DMS target at laser energies between 100-200 mJ/pulse, as shown in Figure 3.3. The laser fluence is calculated by measuring the energy of the laser beam just before the entrance to the deposition chamber with a power meter, subtracting the losses associated with transmission through the quartz window and dividing this by the area of the spot on the target.

Figure 3.3 Photograph of the KrF excimer laser.

3.1.3 Target and Substrate Handling

The target was fabricated by cold pressing the ZnO with Co_3O_4 powder (Sigma Aldrich 99.99% purity) at a force of 10 tons at room temperature into a solid disc with 1 inch diameter. Before this cold pressing, the two chemical powders were ball milled and mixed for 24 hours. The target was placed into a furnace and sintered up to 1200°C for 12 hours. After sintering, the target was placed 6-11 cm away from the substrate inside the high vacuum deposition chamber. The dimension of the focused laser spot that irradiated on the target was approximately 0.03 cm^2.

N-type (100) silicon was used as the substrate for the deposition of DMS thin films, nanodots and core-shell nanowires. Prior to deposition, the substrates were cleaned using SC1, SC2 and HF.

The substrate heater is a 7 cm x 7 cm alloy plate with a Pt alloy filament wounded behind the plate. The filament is resistively heated by applying a constant voltage, which can be adjusted to achieve the desired temperature. Temperature is measured on the surface of the heater with a thermocouple, embedded in a solidified ceramic paste. The samples were attached directly onto the substrate heater. For the DMS thin films, PLD was carried out at different temperatures from room temperature to 600°C.

The synthesis of DMS nanodots and core-shell nanowires was more involved. For the nanodots, an anodic aluminum oxide template was placed on top of the silicon substrate before putting into PLD chamber. For the core-shell nanowires, aligned ZnO nanowires were first grown vertically on top of the silicon substrate instead. The laser ablation of the target lasted between 5-20 mins and DMS nanodots and nanowires were grown on the substrate as a result. More details about the experiments are described in chapter 7.

3.2 Characterization Techniques

After the synthesis, in order to study the crystal structure of DMS thin films, nanodots, and core-shell nanowires, Field Emission Scanning Electron Microscopy (FESEM), Transmission Electron Microscopy (TEM) including High Resolution TEM (HRTEM) and Selected Area Electron Diffraction (SAED), X-Ray Diffraction (XRD), X-Ray Photoelectron Spectroscopy (XPS) and Photoluminance Spectroscopy (PL) were used to carry out the characterizations. Finally, the magnetic properties of DMS materials were characterized using Superconductor Quantum Interface Detector (SQUID).

3.2.1 Field Emission Scanning Electron Microscopy

As synthesized ZnO nanowires and ZnO/$Zn_{0.95}Co_{0.05}O$ core-shell nanowires were viewed under a field emission scanning electron microscope (FESEM, JEOL JSM 6340F). In the FESEM characterizations, the working voltage was 5 kV, and the working distance was 8 cm. The operating principle of a scanning electron microscope is to focus an electron beam as a spot on the sample to be investigated, and scanning this spot across the sample. Each point that is struck by the electron beam produces a response (secondary electrons), which is collected and displayed to give an image. The nanodots and nanowires were scanned to determine their lengths, diameters and size distributions. The FESEM is also equipped with an energy dispersive X-ray (EDX) spectrometer that was used to determine the elemental composition of the nanomaterials. However, there is a spatial limitation in the area from which the detection can be made. In a typical SEM coupled with EDX, the smallest specimen area from which the X-rays can be sampled is 3 μm x 3 μm. In addition, there is a limitation in determining the precise concentration of elements lighter than oxygen. Thus, due to the lower detection limits and orders of magnitude difference in the EDX spot size, higher resolution imaging and compositional analyses were carried out in a Transmission Electron Microscope.

3.2.2 Transmission Electron Microscopy

The composition, phase and crystal structure of the DMS thin films and nanostructures were studied under a transmission electron microscope (TEM, JEM2010). TEM is a powerful technique for crystal structure characterization with real space imaging resolution of 1 Å. The TEM operates on the same fundamental principles as an optical microscope but uses electrons instead of light. TEM uses electrons as the light source and the small wavelength of the electrons causes the atoms in a crystal to act as diffracting centers. Thus, the electron beam provides information about the lattice spacing in a crystal. The underlying principle of TEM is built upon this idea and uses a beam of highly focused electrons to be directed towards a thinned sample to gather information about the sample. The electron beam is focused into a small, thin and coherent beam by the use of two condenser lenses and a condenser aperture before passing through the sample. The condenser aperture helps in knocking out any of the high angle electrons. The highly energetic incident beam then interacts with the atoms in the sample to produce both diffracted and transmitted electrons. The sample needs to be thinned enough to allow the electrons to be transmitted through the sample, much like light being transmitted through the materials in a conventional optical microscope.

The transmitted portion of the electrons is focused to form an image by the objective lens. The objective aperture is placed after the objective lens to knock out any high angle diffracted electrons. This helps in enhancing the contrast of the image. The electrons then pass through a series of two intermediate lenses and a projector lens to form the magnified image of the sample on a phosphor screen. There is also a selected area aperture present right after the objective aperture, which can be taken out or put into the path of the transmitted beam, enabling the user to get diffraction information from the sample. The highly energetic incident electrons interacting with the atoms in the sample and producing both diffracted and transmitted electrons can provide valuable information about the material phase, size, shape and compositional information of the materials. X-ray diffraction (XRD) is a complementary technique to TEM. It provides the user with diffraction information of the sample, from which the phase of the material can be discerned. The working of XRD is similar to TEM but differs in the mechanism in which the X-rays interact with the material.

In the TEM characterizations, our specimens were prepared by hand grinding. Usually, the thickness of samples was in the range of 40 μm -50 μm. After the samples were grinded, ion milling was used with double beam to further thin down the samples.

3.2.3 X-Ray Diffraction

In this research, a general purpose X-ray diffractometer (Shimadzu, LabX XRD-6000) was used to identify and study the crystalline phases in DMS thin films and nanostructures.

XRD is a versatile and non-destructive technique that reveals detailed information about the chemical composition and crystallographic structure of natural and manufactured materials. X-rays are electromagnetic radiation whose wavelength is of the order of 1 Å. Max Von Laue was the first person to hit upon the idea that a crystalline solid consisting of a regular array of atoms form a natural diffraction grating for the X-rays whose wavelengths are about the same dimensions to atomic diameters. The atomic planes of a crystal cause an incident beam of X-rays to interfere with one another as they leave the crystal and form a characteristic interference pattern. This phenomenon is called X-ray diffraction. Diffraction occurs at different angles for different planes. The diffraction condition is satisfied by Bragg's law, which is given by

$$\lambda = 2d \sin\theta \tag{3.1}$$

where λ is the wavelength of the X-ray, d is the interplanar spacing and θ is the Bragg's angle (angle of incidence equals to angle of diffraction).

The diffraction pattern which is formed by diffracted or reflected beams can be used to study the interplanar spacings of various crystal planes. The intensities of distinct peaks from different materials vary for different interplanar spacings and each diffraction angle has corresponding Miller indices (hkl).

In our experiments, 2θ mode was used to characterize the DMS thin films. Incident angle was fixed at 2°, and detectors were rotated during the measurement. The step size used was 0.20°, with a slow scan speed of 0.08°/min.

3.2.4 X-Ray Photoelectron Spectroscopy

The chemical composition of as deposited DMS materials were investigated using a scanning ESCA (Electron Spectroscopy for Chemical Analysis) microprobe (PHI Quantum 2000). When a material is exposed to electromagnetic radiation of sufficiently high energy, the emission of electrons is observed. This phenomenon is known as the photoelectric effect. A high energy photon, which $h\nu$ is significantly in excess of the threshold energy $h\nu_{o,}$ may be capable of separating one photon/one electron photoionization event by ionizing different species of electrons having various ionization energies $I_k < h\nu$. One photon may eject a very loosely bound electron, imparting high kinetic energy to it, while another photon of the same energy might ionize a more tightly bound species of electron and produce a photoelectron of lower kinetic energy. Since the energy levels occupied by electrons are quantized, the photoelectrons have a kinetic energy distribution $n(E)$, consisting of a series of discrete bands that essentially reflect the 'shell' form of the electronic structure of the sample. The experimental determination of $n(E)$ by a kinetic energy analysis of the photoelectrons constitutes photoelectron spectroscopy. Ejection of photoelectrons is a very direct way of obtaining information and characteristics of atoms. If high enough excitation energy is provided, core level spectra can be obtained for all elements in the periodic table except H and He, and the determined binding energies of these core levels are sufficiently unique for their unambiguous identification. XPS will give valuable information about the surface functionalities, compositions and chemical states of the material.

3.2.5 Photoluminescence Spectroscopy

Photoluminescence (PL) spectra were obtained with a fluorescence spectroflurophotometer (Shimadzu RF-5301PC) at room temperature. Optical excitation was provided by a 150 W Xenon arc lamp dispersed by a monochromator. The luminescence spectra were recorded by a secondary monochromator. Photoluminescence spectroscopy is a contact free, non-destructive method of probing the electronic structure of materials. When light of sufficient energy is incident on a material, photons are absorbed and electronic excitations are created. The excess energy that is transferred to the material atoms caused the electrons to be excited from the valence band to the conduction band. This process is called photo-excitation. Since the atoms are disturbed from their equilibrium states, the absorbed energy can be dissipated through the radiative recombination of the excess electrons and holes, which emits light. The intensity and spectral content of the luminescence provides information on the relative rates of radiative and non-radiative recombination and the electronic energy levels of the samples.

3.2.6 Superconductor Quantum Interface Device

The magnetic properties of DMS thin films and nano structures were measured by Superconductor Quantum Interface Device (SQUID). This device can be used to measure extremely weak magnetic signals. A device called Josephson junction is used inside the SQUID to detect the change of energy. The Josephson junction is made up of two superconductors, separated by an insulating layer so thin that electrons can pass through.

Tiny loops of superconductor employing Josephson junctions is integrated inside SQUID to achieve superposition, such that each electron moves simultaneously in both directions. Because the current is moving in two opposite directions, the electrons have the ability to perform as qubits. If SQUID works in Reciprocating Sample Option (RSO) mode, an oscillating current is applied to an external circuit, whose voltage changes as an effect of the interaction between itself and the ring. The magnetic flux is then measured. If it is in the DC mode, it can be much more sensitive to the magnetic flux.

Chapter 4 Co-Doped ZnO Dilute Magnetic Semiconductor Thin Films

4.1 Introduction

Dilute magnetic semiconductors (DMS) have been intensely researched in the last few years due to their promising application in spintronics devices [120, 121]. Many reports on the observation of ferromagnetism in DMS thin films at room temperature have been published, such as Mn-doped GaN with a high Curie temperature of 940 K [124]. Fabrication of group II-VI DMS such as Co-doped ZnO [77,112] and V-doped ZnO [79] has also been reported. ZnO has attracted researchers' interest due to its' optic properties. Co^{2+} and Zn^{2+} has almost same ion radius. Co-doped ZnO DMS thin films will have the same crystal structure of ZnO. The substitution of Zn cations with Co cations would be much easier to occur as compared to substitution with big ionic radius elements such as rare earth ions.

In the earlier 21st century, DMS thin films were deposited by various methods, such as molecular beam epitaxy (MBE) growth, metal organic chemical vapor deposition (MOCVD), sputter deposition, pulsed laser deposition (PLD) and sol-gel method. Among these methods, PLD is a preferred method as it is an easily controllable method to grow thin films and the film quality is comparable with pulse laser assisted molecular beam epitaxy (PL-MBE).

In our experiments, we employ the PLD method to deposit Co-doped ZnO thin films on Si substrates.

4.2 Experimental Details

In this experiment, the target was prepared in the same way as discussed in chapter 3. The Si substrate was cleaned by the standard SC1, SC2 and HF. In order to calibrate the growth rate at different conditions, two sets of experiments were carried out:

1. The pulsed laser power, the frequency of the pulsed laser and the substrate temperature was fixed at 225mJ, 10Hz and 450°C respectively. The oxygen partial pressure was adjusted from 5×10^{-6} Torr to 1×10^{-3} Torr.
2. The frequency of pulsed laser, the substrate temperature, and the oxygen partial pressure was fixed at 10 Hz, 450°C and 5×10^{-6} Torr respectively. The pulsed laser power was changed from 200 mJ to 280 mJ.

Among these two experiments, we used 225 mJ, 10Hz, and 450°C for laser power, frequency and substrate temperature respectively to fabricate DMS thin films with desired thickness (160nm). The oxygen partial pressure was set at 5×10^{-6} Torr. This DMS thin film was characterized by various structural and magnetic measurement equipments.

4.3 DMS Thin Films Growth Rate Calibration

The growth rate of the Co-doped ZnO thin films was characterized at different oxygen partial pressure and pulsed laser powers. The thickness of the samples was measured by a surface profiler after each deposition. Figure 4.1 shows the relationship between the film growth rates with different oxygen partial pressure during the deposition. The substrate temperature was set at 450°C and the pulsed laser power was fixed at 225 mJ with a frequency of 10 Hz. This is the first experiment condition. The relationship between the growth rate and the PLD output powers for samples deposited at 450°C and 5×10^{-6} Torr oxygen partial pressure is plotted in Figure 4.2.

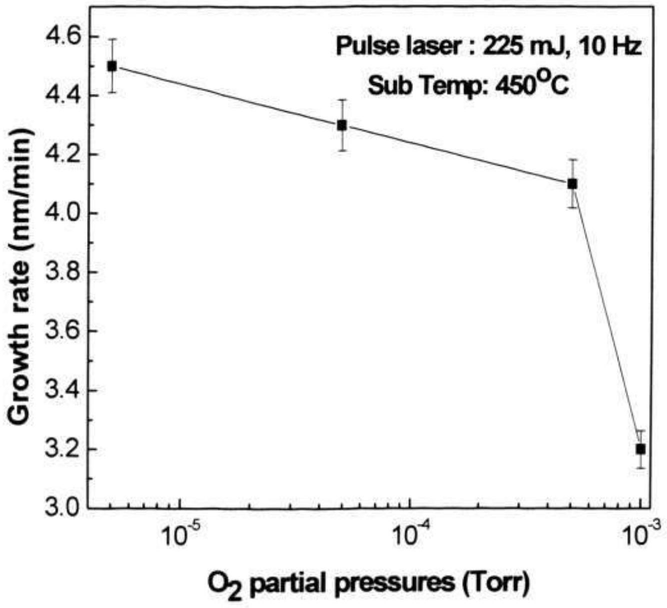

Figure 4.1: Co-doped ZnO thin film growth rate dependence on oxygen partial pressure.

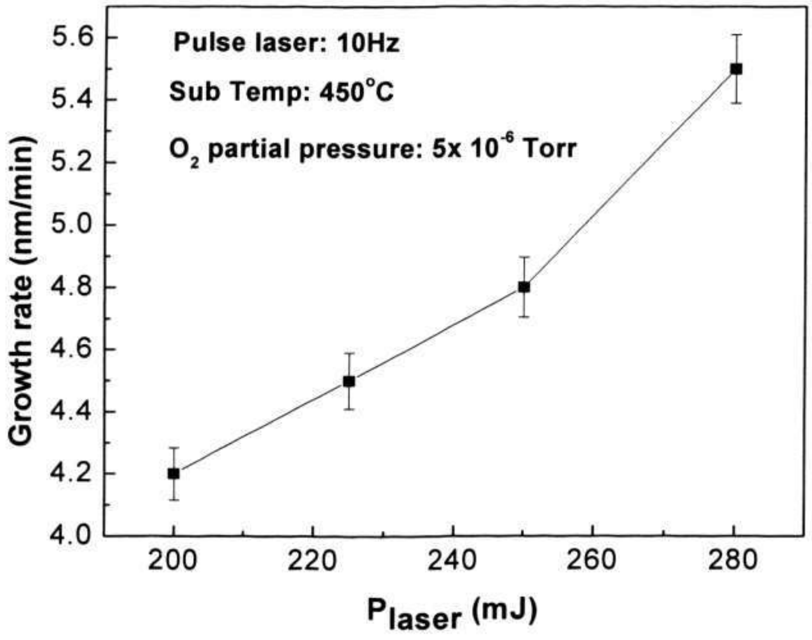

Figure 4.2: Co-doped ZnO thin film growth rate dependence on output laser power.

As observed from the figures, the growth rate of these DMS thin films is extremely low as compared with sputtering. If the output laser power is kept at 225 mJ, frequency of 10 Hz with an oxygen partial pressure of 5×10^{-6} Torr, and the substrate is at 450°C, the growth rate will be 4.5 nm/min, which is equivalent to 0.75 Å/s. The reason for this extremely low deposition rate is because the distance between the target and substrate is quite large at 11 cm. The dependence of PLD deposition rate is similar with that of sputter deposition. It could be explained simply by the following equation:

$$R = m\lambda \tag{4.1}$$

Here, R denotes the deposition rate, m is the amount of plume generated during the pulsed laser ablation and λ is the mean free path of the plume. The amount of plume generated is directly proportional to the pulsed laser power and frequency. The mean free path of the plume is inversely proportional to the chamber pressure. So equation 4.1 could be rewritten as:

$$R = k(P_{laser} \times f_{laser})/P_{chamber} \tag{4.2}$$

Where k is the deposition rate constant, P_{laser} is the pulsed laser power, f_{laser} is the frequency of pulsed laser and $P_{chamber}$ is the chamber pressure.

At a higher vacuum level, the chamber pressure is lower and the growth rate will be higher. The mean free path of the plume is larger as fewer collisions between the plume and ambient gases would occur. As a result, more DMS atoms will reach the substrate in a shorter time, such that a higher deposition rate will be observed. If a higher laser power is applied, the growth rate will be higher as well. This is shown in Figure 4.2. This is because at higher output power, there would be more energy transfer to the target. Thus, the volume of plume generated by the laser would be larger, which will provide more source atoms for the deposition. For subsequent sample preparation, the frequency used would be fixed at 10 Hz for the output pulsed laser. This is because if the frequency is too low, the system will be unstable, and the power will experience a larger fluctuation.

The power used for subsequent samples preparation is 225 mJ, which is 1.4 J/cm^2 in power density. This is because if a much higher power is used, there would be an increased possibility of obtaining clusters during the deposition, such that the structural quality of the samples will be reduced. On the other hand, if a lower power is applied, due to the large distance between target and substrate, the deposition rate would be too small. Thus, the output power was optimized in this experiment for future research.

4.4 DMS Thin Films on Si Substrate

Using the fixed pulsed laser power at 1.4 J/cm^2 with a frequency of 10Hz, the DMS thin films were prepared. The substrate to target distance was fixed at 11 cm.

Figure 4.3 (a) shows an AFM image of the as-grown ZnO:Co thin film on a Si substrate. The root mean square roughness of the surface is 0.56 nm while the grain size is about 30 nm. Both grazing incidence and θ-2θ methods employed in XRD investigations showed that all films were single phase with wurtzite structure. Furthermore, it is clear from the results of the θ-2θ method that the ZnO:Co thin film has (002) preferential orientation. The grazing incidence x-ray diffraction (GIXRD) results of the Si substrate and the ZnO:Co thin film is presented in Figure 4.3 (b). An illustration of calculating DMS thin film preferential orientation is shown in Figure 4.3 (c). The incidence angle θ was fixed at 2°. A (103) enhanced intensity peak is evident at θ =31.38°, which is very close to the calculated interplane angle of 31.66° between (103) and (002) in wurtzite structure. This further indicates a (002) preferential orientation.

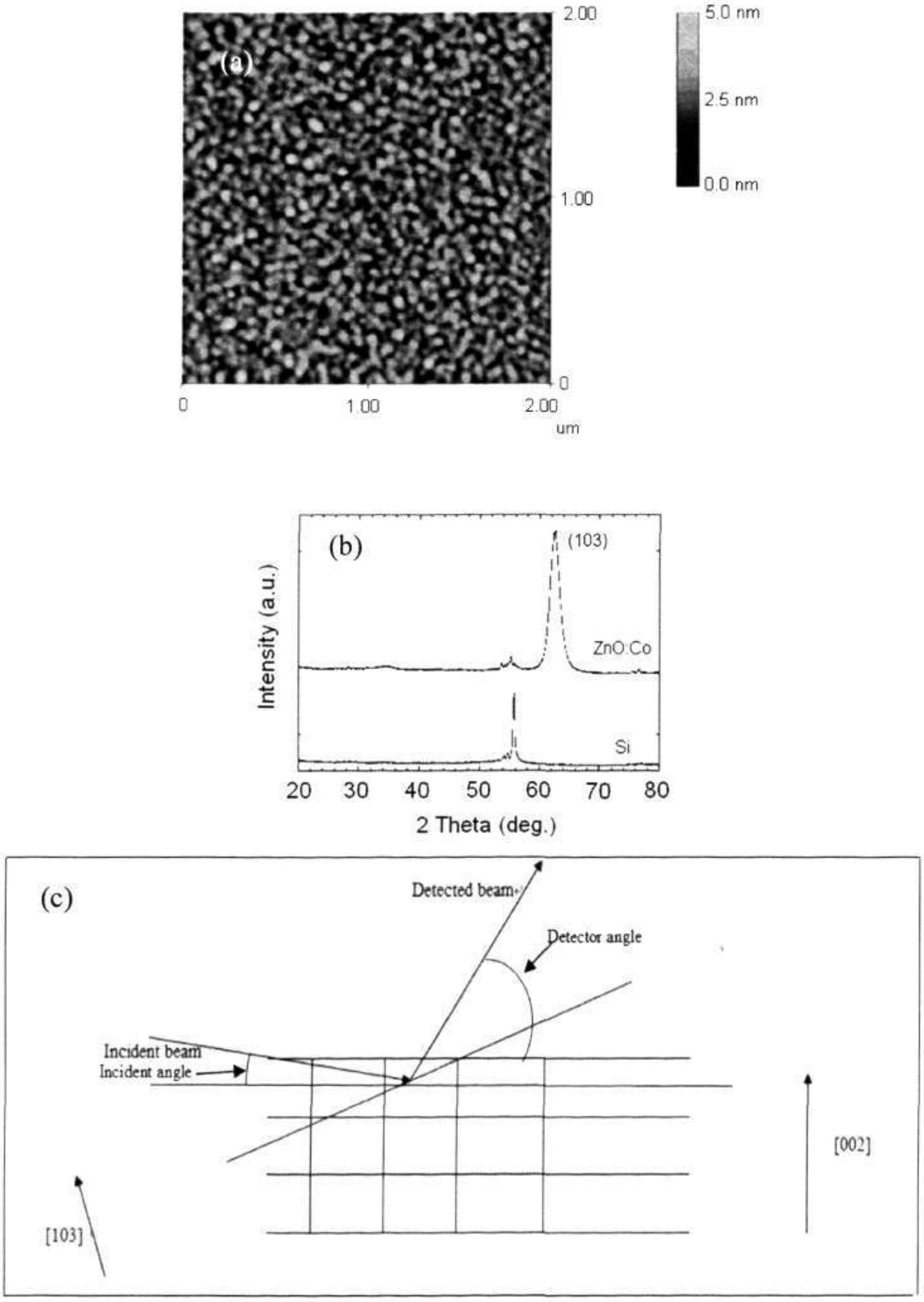

Figure 4.3 (a) An atomic force microscopy (AFM) image of the ZnO:Co thin film on a Si substrate. (b) Grazing incidence x-ray diffraction (GIXRD) patterns of the Si substrate and the ZnO:Co thin film. (c) Illustration of calculating DMS thin film preferential orientation.

Figure 4.4 shows typical cross-section HRTEM images of the ZnO:Co thin film. It is clear in Figure 4.4 (a) that the ZnO:Co thin film has a thickness of about 100 nm. Numerous defects were evident in the film at higher magnifications. The higher magnification in Figure 4.4 (b) shows the interface between ZnO:Co and Si where an amorphous SiO_2 layer of a thickness of about 4 nm is clear. It is found that the there are some shaded areas that originate from just above this SiO_2 layer and extend to the ZnO:Co thin film. These could be due to variation in thickness, strain, or defects. Figure 4.4 (c) is a further magnification of Figure 4.4 (b), showing lattice fringes of the single-phase ZnO:Co wurtzite structure. The distance between neighboring lattice fringes was measured to be 0.26 nm, which equals the (002) interplanar spacing in ZnO. Since these fringes are parallel to the interface with the substrate, this further confirms that the film has a (002) preferential orientation, i.e., grows along the [001] direction. Metallic cobalt precipitates or nanoclusters were not observed in the TEM images. However, edge dislocations were observed, two of which are marked by the white arrows in Figure 4.4 (c). The inset in Figure 4.4 (c) is a selected area electron diffraction (SAED) pattern of the ZnO:Co thin film. Its zone axis is [100]. The diffraction pattern again demonstrates that the ZnO:Co film grows preferentially along [001] direction. It may be due to the lowest binding energy in the [001] direction of ZnO. It must be noted from the SAED that the ZnO:Co thin film is not homoepitaxial like films on sapphire substrate but still has the (002) preferential orientation. This is in agreement with the XRD observations. The edge dislocations are probably caused by the lattice distortion induced through Co doping to ZnO and the non-epitaxy with the SiO_2 /Si substrate.

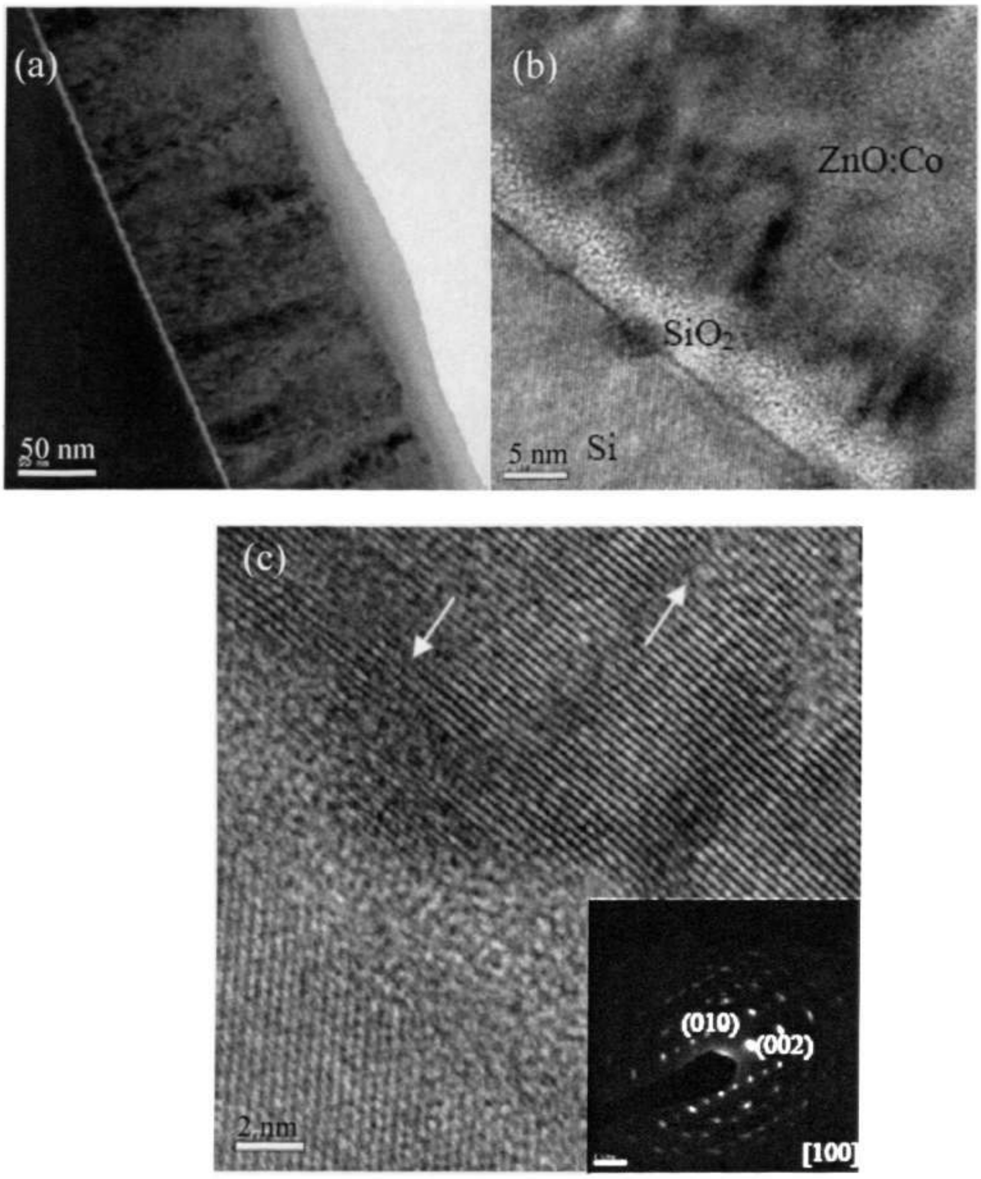

Figure 4.4 (a) A low magnification cross-section high resolution transmission electron microscopy (HRTEM) image of the ZnO:Co thin film. Scale bar: 50 nm. (b) A high magnification HRTEM image of the interface between ZnO:Co and SiO_2/Si. Scale bar: 5 nm. (c) A HRTEM image of the ZnO: Co/SiO_2/Si thin film. The white arrows mark the edge dislocations. Scale bar: 2 nm. Inset is the corresponding selected area electron diffraction (SAED) pattern of the ZnO:Co thin film. Scale bar: 1 1/nm.

The XPS spectrum of Figure 4.5 shows that the Co ion in the ZnO:Co thin film is in the +2 formal oxidation state. The peaks for Co $2p_{3/2}$ and $2p_{1/2}$ and their shakeups were fitted using Gaussian method and the resulting Co $2p_{3/2}$ and $2p_{1/2}$ core levels for Co–O bonding were found to be at 780.07 and 796.07 eV, respectively, which is comparable to the results reported by Lee *et al.*[74]. This further excludes the possibility of the Co cluster formation because the Co $2p_{3/2}$ core level for the Co metal cluster is at 778.3 eV and the energy difference between Co $2p_{3/2}$ and $2p_{1/2}$ core levels for metallic Co is 14.97 eV [125]. Such peaks were not observed.

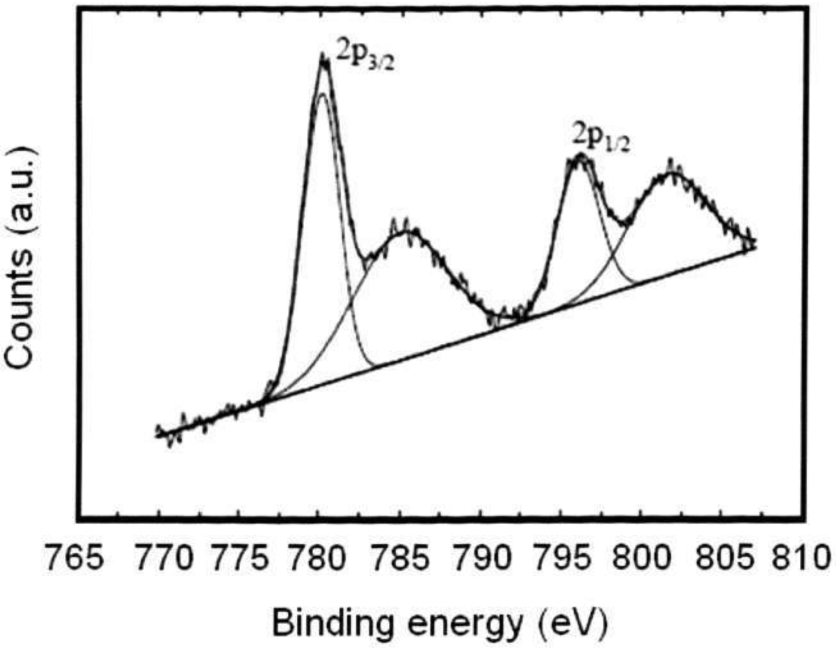

Figure 4.5 X-ray photoelectron spectroscopy (XPS) studies of Co $2p_{3/2}$ and $2p_{1/2}$ peaks for the ZnO:Co thin film.

Figure 4.6 shows a ferromagnetic behavior in the curve of magnetization versus field for the ZnO:Co thin film at room temperature. Using the actual Co content measured by XPS in the ZnO:Co thin film, the saturation moment was computed to be 0.86 μ_B/Co, which is higher than 0.7 μ_B/Co reported for highly crystallized ZnO:Co thin films deposited by alternating pulsed laser ablation of pure metals of Zn and Co [126]. It must be noted that the saturation moment obtained is much lower than 1.7 μ_B/Co for metallic Co, suggesting the dominance of Co^{2+} ions.

Figure 4.7 shows a ferromagnetic behavior in the curve of magnetization versus field for the ZnO:Co thin film at 5 K. Using the actual Co content measured by XPS in the ZnO:Co thin film, the saturation moment was computed to be 0.98 μ_B/Co.

Figure 4.8 shows zero field cooling (ZFC) and field cooling (FC) curves. From these magnetization versus temperature results, no spin glass states was detected, and no superparamagnetism was detected either. By combining the M-H curves at low and room temperature and this ZFC-FC measurement, it is shown that the magnetic properties in the DMS thin films prepared by the above mentioned method is ferromagnetism, and the Curie temperature is above the room temperature.

The claims of this room temperature ferromagnetism for DMS thin films still remain contentious. There are some research groups who claimed that the ferromagnetic properties could be due to the metallic cobalt nanoclusters in the DMS thin films, and these nanoclusters are localized and difficult to be detected by current characterization technology. Besides this, there are some other explanations for the ferromagnetism, such as double-exchange interaction [98], Ruderman–Kittel–Kasuya–Yosida indirect exchange [77] and donor impurity band exchange [88, 126]. The crucial role of defects has now been recognized in the nature of magnetic interactions for transition metals doped ZnO [141].

In the double exchange model, when the magnetic ions are ferromagnetically aligned, the kinetic energy of the carriers hopping between magnetic sites is minimized, and a large exchange coupling forces the spin of the carrier to be parallel to the local magnetic moment. This model is usually applicable for those materials that are metallic and ferromagnetic. The ferromagnetic critical temperature in the double exchange model depends on the concentration of carriers [98]. In our DMS thin films, it is an oxide based material. Its conductivity is not as high as metallic materials. Therefore, the double exchange model is not a suitable mechanism to explain the room temperature ferromagnetism of DMS thin films. However, when the effective exchange coupling is larger, the double exchange model would be appropriate for the low Curie temperature DMS materials [98].

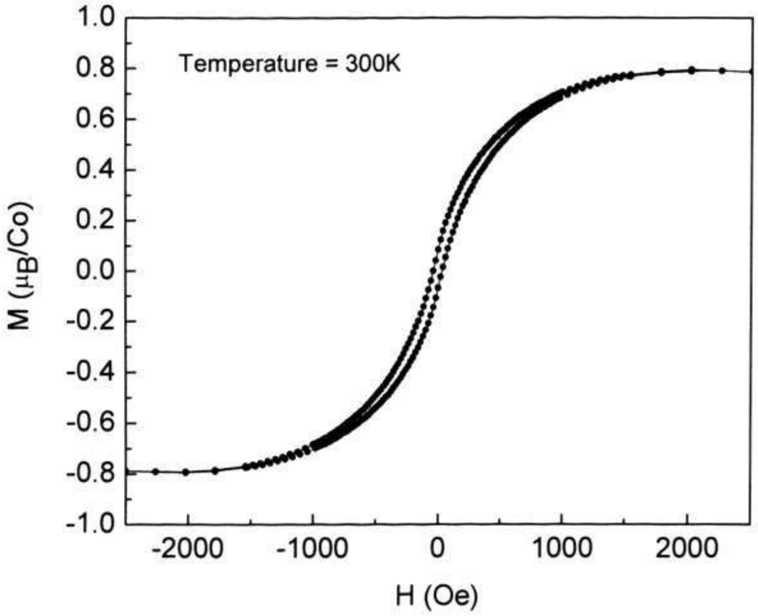

Figure 4.6 Magnetization as a function of field for the ZnO:Co thin film at room temperature.

The possible mechanisms for the room temperature ferromagnetism of our thin films could be narrowed down to (1) metallic cobalt nanoclusters, (2) bound magnetic polarons, or (3) RKKY indirect interaction.

Metallic cobalt nanoclusters could have been formed in the thin films, although the XRD, TEM and XPS data show that no metallic Co was detected in the structure of our thin films. This can be due to the instrument's limitations. For example, the TEM only examines a small area of the samples. On the other hand, XPS will only detect the surface of the thin film and can not give information on the whole thickness of the thin films. Thus, further investigations and characterizations are required to verify this point.

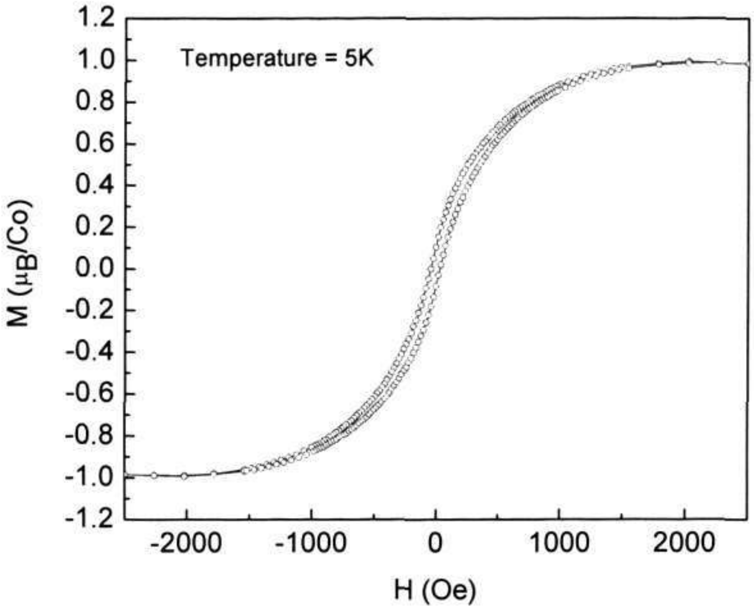

Figure 4.7 Magnetization as a function of field for the ZnO:Co thin film at 5 K.

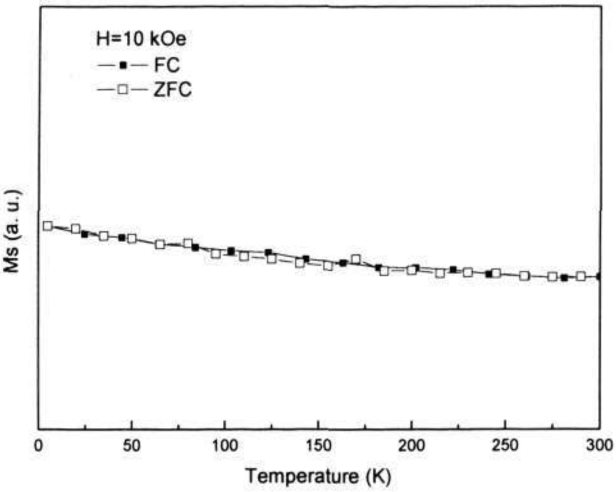

Figure 4.8 ZFC-FC curves for the DMS thin films measured with an external field at 1 T.

Donor impurity band exchange can be another possible mechanism which explains the ferromagnetism in the thin films. In this model, localized carriers associated with the defects form bound magnetic polarons. In this polaron, the magnetic ions will interact with the localized electrons, such that the magnetic ions will try to be aligned. These polarons with aligned magnetic ions will overlap with each other, such that a long range magnetic alignment will be achieved. Our ZnO-based DMS material forms defects quite easily, such as zinc interstitials and oxygen vacancies, and these defects are shallow donors. It donates localized carriers inside the cobalt doped ZnO thin films, which can give rise to long range ferromagnetic interactions. In this model, the oxygen vacancies density and magnetic cation concentrations are the two parameters that decide the magnetic properties of the DMS thin films. Further investigation of this model will be discussed in chapter 5.

RKKY exchange is the third possible mechanism. This interaction occurs through the conduction electrons. This interaction is always ferromagnetic at low electron densities. At higher electron densities, the interaction will provide equal negative and positive exchange bond, such that the system will become a spin glass. This interaction is operative even when the Fermi level lies below the mobility edge, which provides the separation of magnetic cation neighbors that are less than the localization length. In our DMS thin films, no spin glass state was observed. It shows that the room temperature ferromagnetism may be due to delocalized electrons generated by the defects inside the DMS thin films interacting with the magnetic cations. It can be seen that the amount of delocalized carriers and amount of magnetic cations would play an important role in the ferromagnetic properties of oxide based DMS materials.

According to the discussion above, the effective magnetic model Hamiltonian for interacting impurity moments and the interaction of magnetic cations M with the hydrogenic electrons in the impurity band can be expressed in equation 4.3. The contribution of the metallic cobalt is not considered in this Hamiltonian.

$$H = \sum_{ij} J_F(r_{ij}) S_i \cdot S_j + \sum J_{AF} S_i \cdot S_j + \sum J_F^{'} S \cdot s \tag{4.3}$$

The first term on the right of this Hamiltonian is the ferromagnetic coupling between the magnetic cations through delocalized carriers. Here, J_F indicates the ferromagnetic coupling parameter, r_{ij} is the spatial separation between randomly located substitutional Co pair in the ZnO lattice and S_i, S_j are the impurity spins. The second term on the right is the antiferromagnetic coupling due to the direct interaction between magnetic cations, where J_{AF} is the antiferromagnetic coupling parameter. The third term describes the ferromagnetic interaction between the localized donors with the magnetic cations. J'_F is the ferromagnetic coupling parameter for the impurities and localized carriers.

By focusing on these three contributions, the origins of the ferromagnetism inside the cobalt doped ZnO would be investigated further, and experiments would be introduced to investigate the above mentioned mechanisms in the subsequent chapters.

4.5 Summary

In summary, ZnO:Co diluted magnetic semiconducting thin films with (002) preferential orientation have been deposited on (001) Si substrates by pulsed laser ablation. Single-phase wurtzite ZnO:Co was obtained without any Co nanoclusters although numerous edge dislocations were formed during film growth. A saturation magnetization of 0.86 μ_B/Co and a coercivity of 25 Oe were achieved at room temperature. The room temperature ferromagnetic properties in the oxide-diluted magnetic semiconductor could be due to three contributions: (1) metallic cobalt nanoclusters formed inside the thin film, (2) the interaction between delocalized electrons generated by the defects (eg. oxygen vacancies, zinc interstitials) with magnetic cations, and (3) the delocalized electrons due to the thermal excitation of shallow defects generated donors inside the thin films interacting with the magnetic cations.

Chapter 5 Origins of Ferromagnetism in Co-Doped ZnO Thin Films

5.1 Introduction

After years of research, the origin of ferromagnetism in DMS materials is still under debate as mentioned in the previous chapter [79]. One point of contention is whether observed magnetic property is due to the presence of cobalt microclusters in the cobalt doped-ZnO thin films, and it has been a challenge to rule out the contribution of cobalt nanodots to the ferromagnetism observed in DMS [55, 80, 131].

In order to explore the impact of metallic cobalt on the ferromagnetic behavior in Co-doped ZnO thin film, two systems were designed. (1) ZnO thin films doped with a low concentration (5%) of Co and (2) ZnO thin films embedded with Co nanodots were grown using pulsed laser deposition technique at oxygen partial pressures of 5×10^{-7} Torr and 5×10^{-4} Torr. The structural and magnetic properties of these two systems were then studied and compared.

Besides the contribution of metallic cobalt nanoclusters, further experiments are required to address the origins of ferromagnetism behavior in Co-doped DMS thin films. According to the effective magnetic Hamiltonian discussed in chapter 4, one contributing factor to the ferromagnetism in Co-doped ZnO thin films is the coupling between localized electrons and magnetic cations inside the bound magnetic polarons. In ZnO, the formation energy is different for different defects. Zinc interstitials and oxygen vacancies have lower formation energy than the other defects. Thus, zinc interstitials and oxygen vacancies are the two types of defects that are formed most easily in ZnO [179, 180]. Oxygen vacancies affect the concentration of localized electrons. It is expected that different oxygen partial pressure would lead to different magnetic properties due to the different oxygen vacancies concentrations. In order to investigate this hypothesis in depth, cobalt-doped ZnO single phase thin films were deposited at different oxygen partial pressure, such that the amount of oxygen vacancies generated during the deposition could be varied. The corresponding magnetic and structural properties of the thin films were then characterized. After that, the thin films were annealed in oxygen rich ambient to reduce the oxygen vacancies, and the magnetic properties were characterized again.

In addition to the BMP model, the origins of room temperature ferromagnetism DMS materials that were discussed in chapter 4 has another two components: (1) RKKY indirect interaction through delocalized carriers, and (2) direct interaction between magnetic cation which will give anti-ferromagnetism. In the RKKY model, the carrier concentration effects will be investigated in this chapter. However, another factor that may affect the magnetic properties in DMS thin films is the mean free path of the free carriers. In this chapter, the carrier induced ferromagnetism in cobalt-doped ZnO single phase thin films on a Si substrate would be demonstrated by adjusting the substrate deposition temperature, and characterizing the magnetic and structural properties of the thin films.

5.2 Experiment Details

In this chapter, three sets of experiment were carried out. The laser system used for these three experiments were kept the same as the one mentioned in the previous chapter. The deposition conditions and target were changed accordingly. The details of these three sets experiment are shown below:

1. For the fabrication of Co nanodots embedded ZnO thin films, the target consisted of one piece of high-purity (99.95%) ZnO (diameter D = 25 mm) round target and a square piece of single crystal of Co (about 3 mm in length). The Co target was glued onto the surface of the ZnO target, making a two-material assembly with only

physical, but not chemical, contact between them. During the pulsed laser deposition (PLD) process, to form the nanodots embedded in the ZnO matrix, the Co–ZnO target assembly was set to spin slowly about its central axis and the laser beam vaporized the two component materials alternately. The deposition and growth of the films on the substrate were carried out in a high vacuum system with an oxygen partial pressure of about 5 x 10^{-7} Torr or 5 x 10^{-4} Torr, with the target rotating at about 20 rounds/min at room temperature. By controlling the area ratio of ZnO and Co areas exposed to the laser ablation, along with the target rotation speed, Co nanodots embedded in polycrystalline ZnO thin films were produced. At meantime, the same DMS thin films preparation method in chapter 4 was used to prepare the DMS thin films samples in this experiment.

2. $Zn_{0.95}Co_{0.05}O$ thin films were grown directly on n-type (100) Si substrates by pulsed laser deposition (PLD) technique with the oxygen partial pressure varied between 5×10^{-6} Torr and 5×10^{-3} Torr for 40 minutes at 450°C. The target and the deposition system is the same as discussed in chapter 4. In order to introduce oxygen vacancies into the film, a low oxygen partial pressure was applied during the deposition. To further increase the concentration of oxygen vacancies, an *in-situ* cooling down process was carried out after the deposition. After the characterization of structural and magnetic properties, the thin films were annealed in oxygen rich conditions to reduce the oxygen vacancies. The magnetic properties and optical properties were characterized again.
3. The target was prepared by using the same method mentioned in the experimental chapter. $Zn_{0.95}Co_{0.05}O$ thin films were grown directly on n-type (100) Si substrates by pulsed laser deposition (PLD) technique with the substrate temperature between 320°C to 500°C. The deposition was carried out with an oxygen partial pressure of 5

× 10^{-6} Torr for 40 minutes. To introduce the oxygen vacancies into the deposited films, an *in-situ* cooling down process was carried out after the deposition.

5.3 Contribution of Metallic Co Nanoclusters to Ferromagnetic Property

Figure 5.1 shows the XRD patterns of (a) a cobalt nanodots embedded ZnO matrix, (b) a cobalt-doped ZnO DMS thin film, and (c) a pure ZnO film. All three samples were prepared under the same condition, such that the thickness of these films was all approximately 160 nm. In the cobalt nanodots embedded ZnO matrix system, the ZnO matrix is polycrystalline and a second phase which corresponds to hexagonal *metallic* cobalt peak located at 43.98° was detected. Compared to the pure ZnO thin film, the full widths at half maximum (FWHM) of ZnO films embedded with nanodots are much larger. This larger FWHM could be due to the smaller grain size or micro strain inside the Co nanodots embedded system.

The XRD pattern of the 5% cobalt-doped ZnO DMS thin film indicates that the DMS thin film is polycrystalline. Compared to the cobalt nanodots embedded system, it shows that the FWHM of the DMS is relatively smaller, which may be due to less defects, as the ionic radius of cobalt and zinc is almost the same.

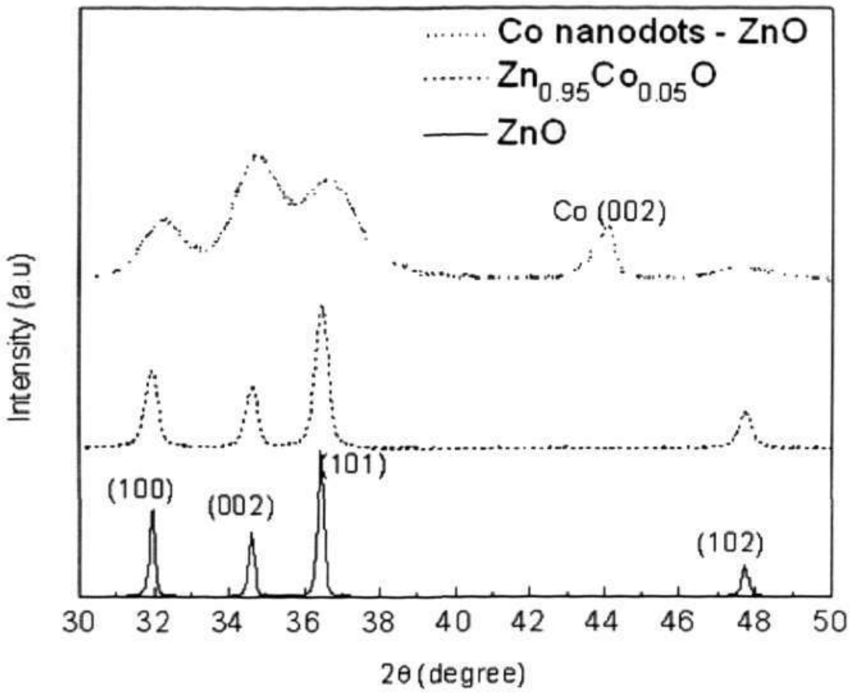

Figure 5.1 XRD patterns for (a) cobalt nanodots embedded ZnO matrix, (b) $Zn_{0.95}Co_{0.05}O$ thin film, and (c) pure ZnO thin films prepared under room temperature at 5 × 10^{-7} Torr.

Figure 5.2 (a) and 5.2 (b) show the planar TEM image of the synthesized Co nanodots embedded ZnO film under different magnification, with its corresponding high resolution TEM images shown in Figure 5.2(c) and 5.2(d). Figure 5.2(c), which is region (1) that is indicated by a square box in Figure 5.2(b), shows that the distance of the lattice fringes in region A is around 0.20 nm, which corresponds to the hexagonal cobalt (002) inter-plane distance. In region B of the HRTEM image, the lattice fringes distance is approximately 0.26 nm, which corresponds to a (002) orientation of the ZnO. Figure 5.3 shows the selected area diffraction pattern and it was matched against a simulated diffraction pattern for ZnO and Co generated using a TEM simulator, Java electron microscopy simulation (JEMS), software. Comparing the experimental and simulated diffraction patterns, it can be deduced that the nanodots are metallic Co with a hexagonal structure. Figure 5.4 shows the distribution of the nanodots' size, which was obtained by carefully measuring each distinguishable particle. A Gaussian distribution was fitted, which approximately yielded values of an average diameter D of 4.47 nm and standard deviation σ of 0.78 nm for the nanodots. The average area density of the nanodots is estimated to be about 1×10^{12} cm^{-2}.

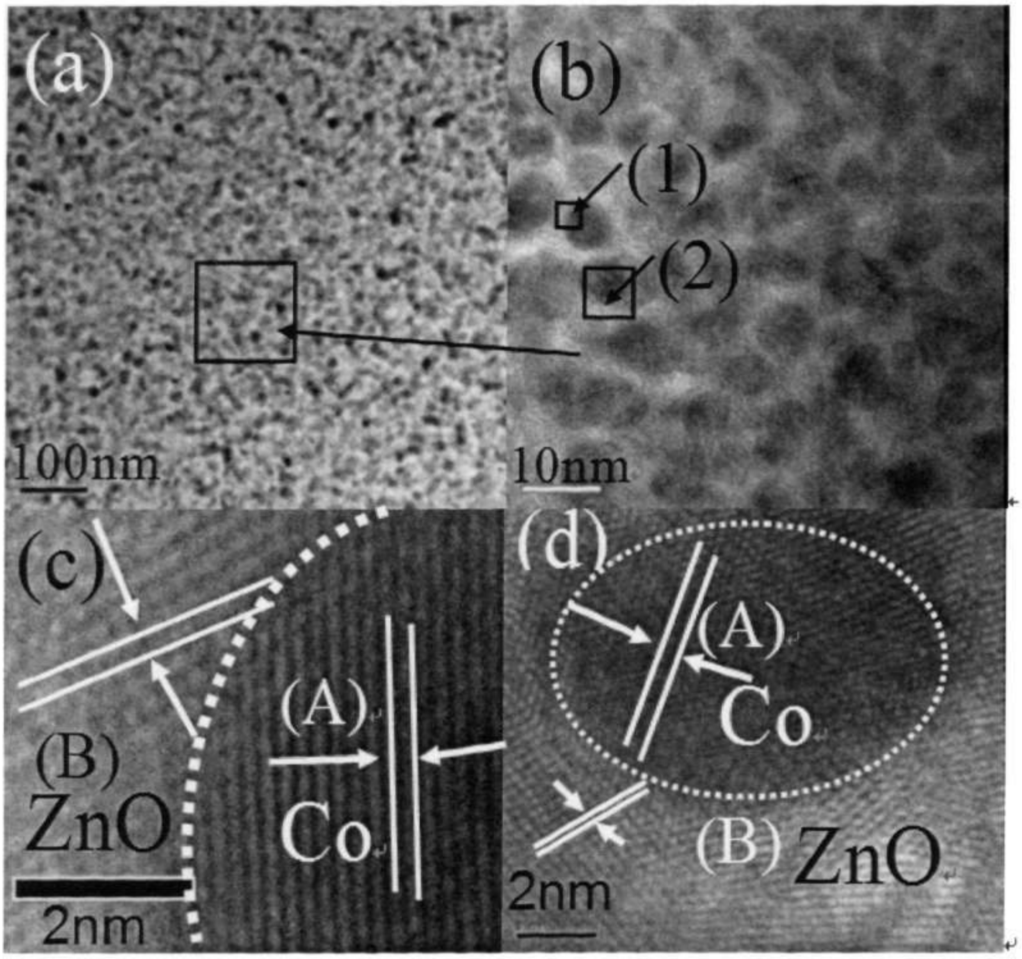

Figure 5.2 (a) Planar TEM image of the synthesized Co nanodots embedded in ZnO matrix films, (b) higher magnification of planar TEM image, (c) HRTEM of region 1 in (b), (d) HRTEM of region 2 in (b).

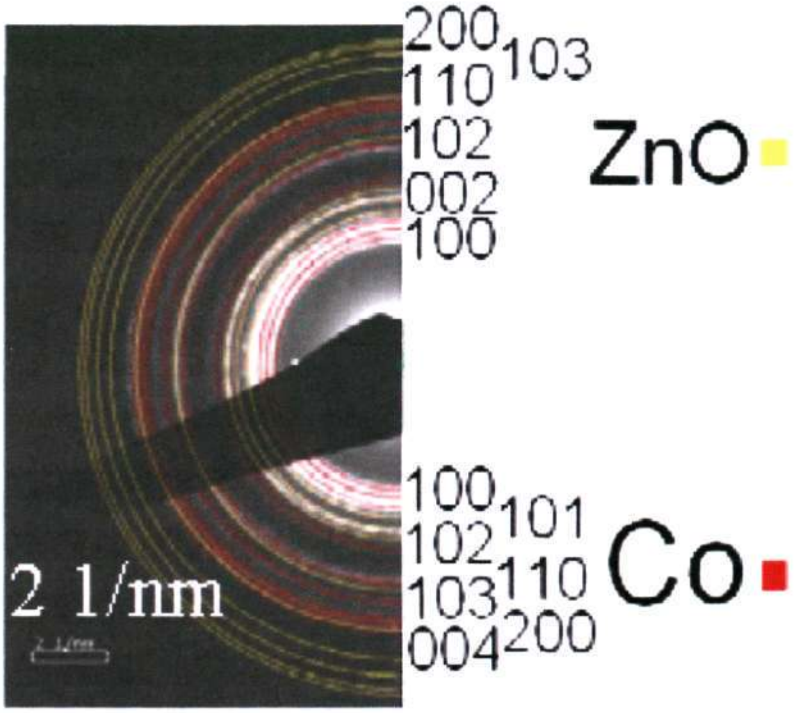

Figure 5.3 Electron diffraction pattern of Co nanodots embedded ZnO matrix films with JEMS fitting.

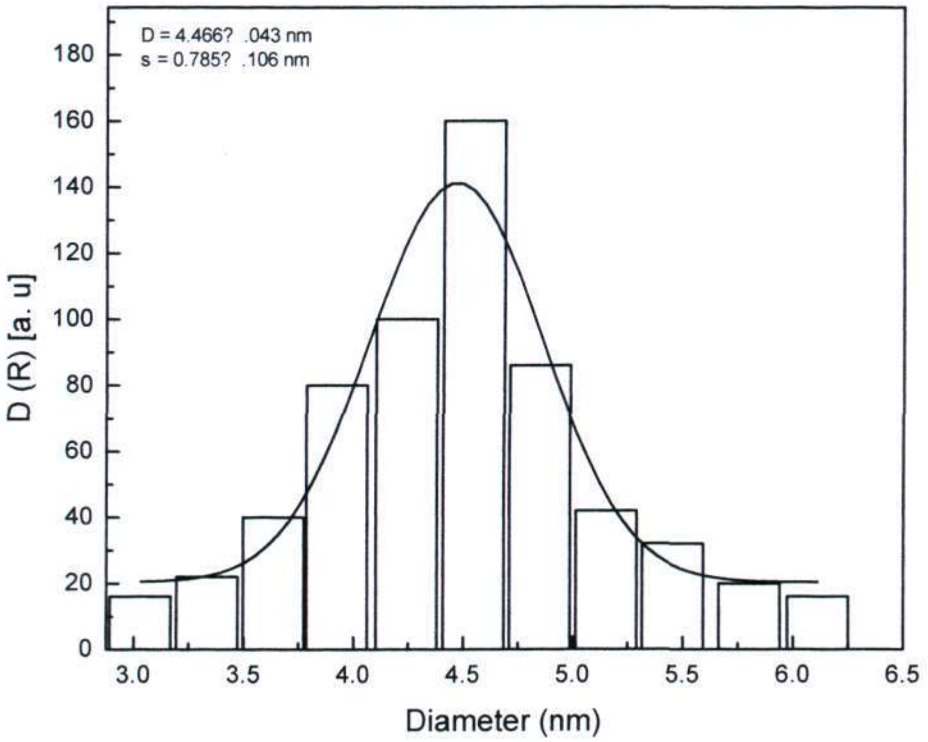

Figure 5.4 Gaussian distribution fit for the nanodots size.

Figure 5.5 shows the room temperature M-H curves for the DMS thin films and ZnO thin films embedded with cobalt nanodots fabricated under the same condition. Room temperature ferromagnetism can be observed in both the DMS thin film and cobalt nanodots embedded system. From the measurements, we observe that the saturated magnetization of DMS thin films is around 0.4 μ_B/Co, which is much smaller than the cobalt nanodots embedded system. For nanodots embedded systems, the saturation magnetization is around 1.1 μ_B/Co, which is comparable with that of the metallic cobalt. This indicates that the room temperature ferromagnetism is due to the metallic cobalt nanodots. It is also observed that the DMS thin film will reach a saturation condition when the external field is around 1500 Oe. However, for the nanodots embedded system, the magnetization is saturated only when the external field was increased to 3000 Oe.

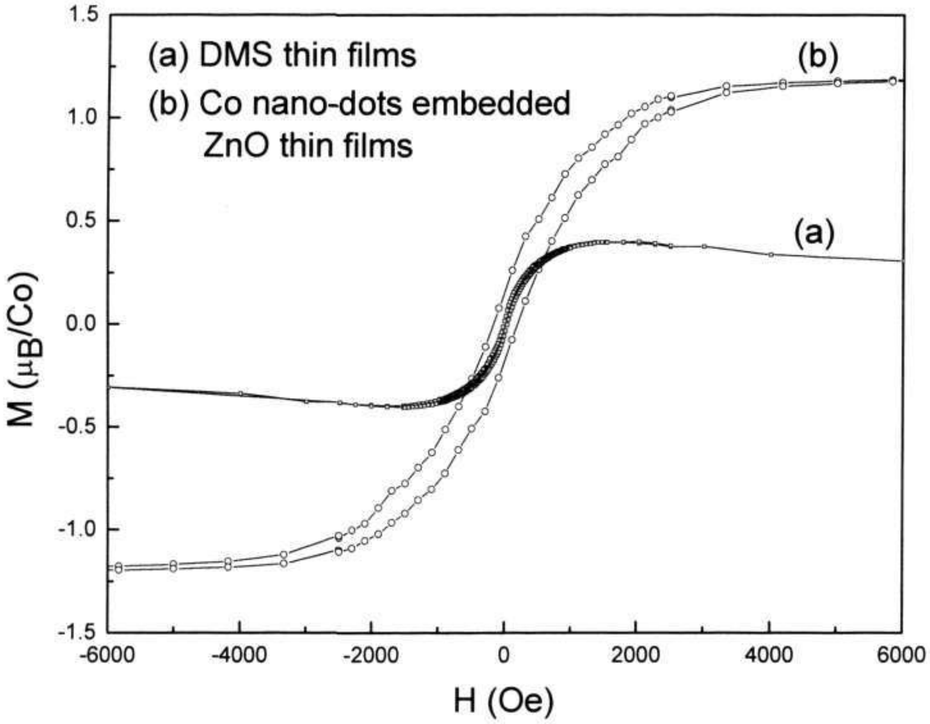

Figure 5.5 M-H curve for (a) DMS thin films, and (b) cobalt nanodots embedded ZnO thin films deposited at 5 x 10^{-7} oxygen partial pressure under room temperature.

Furthermore, Figure 5.6 shows the room temperature M-H curves for (a) a DMS thin film, and (b) a cobalt nanodots embedded ZnO thin film which was prepared at an oxygen partial pressure of 5 x 10^{-4} Torr with other parameters the same. Room temperature ferromagnetism was observed in the DMS thin film. However, the cobalt nanodots embedded system shows paramagnetism. This may be due to the oxidation of Co during the PLD deposition. From the nanodots embedded ZnO system, the magnetization curve indicates that the cobalt is not likely to be metallic, which implies that the cobalt was fully oxidized. The XRD data shown in Figure 5.6(c) supports this hypothesis, as it indicates that the embedded cobalt nanodots inside the ZnO matrix were in the form of cobalt oxide, and it has a peak of (200) which is located at 42.44°. The proposed oxidation behavior is shown in Figure 5.7. In the DMS thin films, even if a cobalt nanocluster was formed during the deposition, it would most likely be oxidized as well at such a high oxygen partial pressure. Thus, the room temperature ferromagnetism observed in our DMS thin films fabricated at 5 x 10^{-4} Torr is not likely due to the presence of metallic cobalt clusters.

Another observation made from Figure 5.6 is that the saturation magnetization of the DMS thin films is around 0.3 μ_B/Co. According to equation 5.1:

$$0.3 = (1.72 \times x\%) \quad \rightarrow x\% = 17.5\% \tag{5.1}$$

Where $x\%$ is the percentage of the cobalt that is doped inside DMS thin films in the form of metallic cobalt nanocluster.

If the saturation magnetization is indeed due to the presence of metallic cobalt nanoclusters in the films, it will require around 17% of the cobalt that is doped inside the ZnO to form the nanoclusters, taking the average magnetic moment of bulk Co to be 1.72 μ_B/Co. However no such high density of nanoclusters was detected from our TEM and

XPS data as shown in Figure 5.8 and Figure 5.9, respectively. Figure 5.8 (a) and (b) shows two different randomly chosen areas from the DMS thin films. It shows that there are no cobalt clusters as observed from these TEM results. Figure 5.9 shows the XPS data of the DMS thin films. From the XPS data, cobalt was found to be in the +2 formal oxidation state. The peaks of Co $2p_{3/2}$ and $2p_{1/2}$ core levels were at 780.09 and 796.09eV, respectively, which further excludes the possibility of the cobalt cluster formation. This is because the cobalt $2p_{3/2}$ core level for the cobalt metal cluster is at 778.3eV and the energy difference between cobalt $2p_{3/2}$ and $2p_{1/2}$ core levels is 14.97eV, which were discussed in previous chapter.

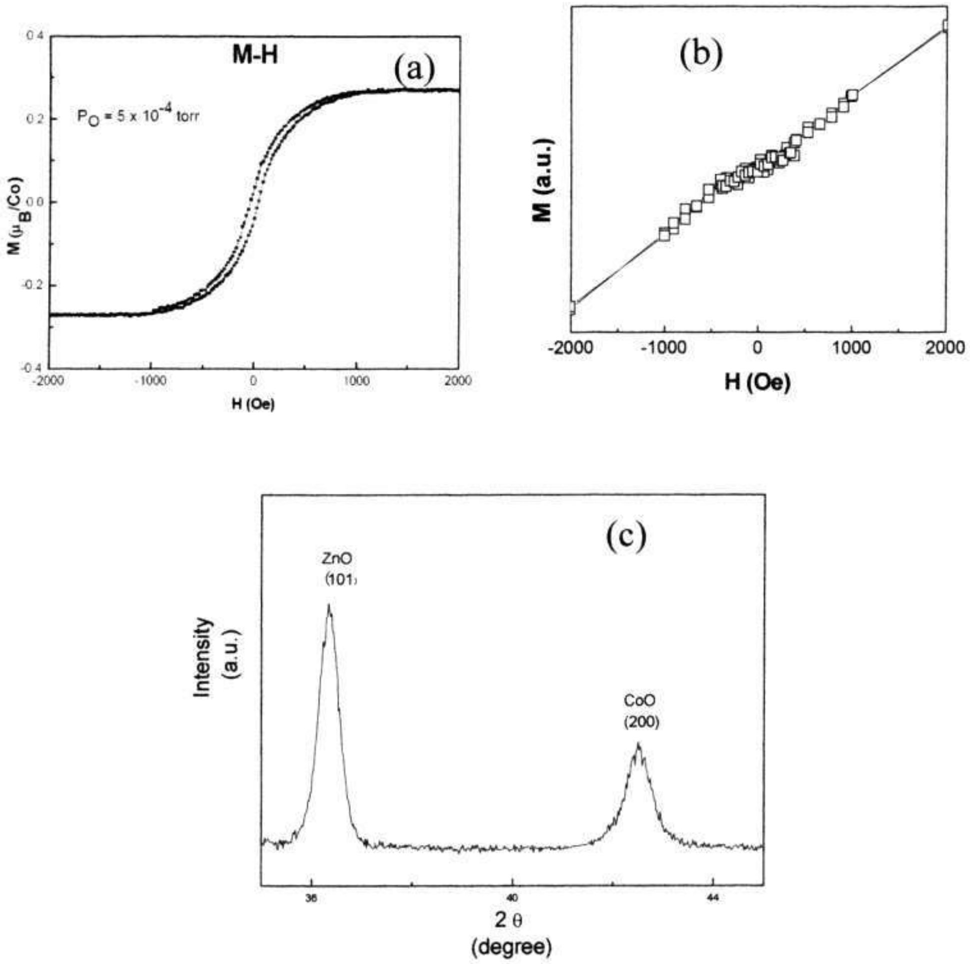

Figure 5.6 M-H curves for (a) a DMS thin film, and (b) a cobalt nanodots embedded thin film prepared at 5 x 10^{-4} oxygen partial pressure under room temperature with its XRD result shown in (c).

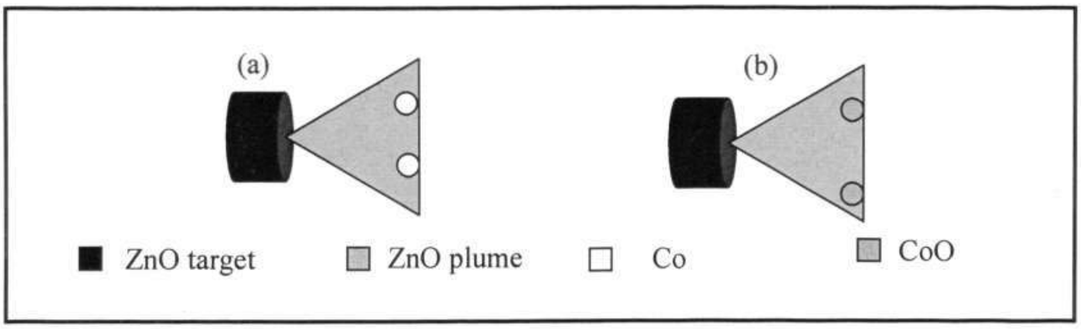

Figure 5.7 Oxidation of cobalt in the cobalt nanodots embedded ZnO system (a) at low oxygen partial pressure, and (b) at higher oxygen partial pressure.

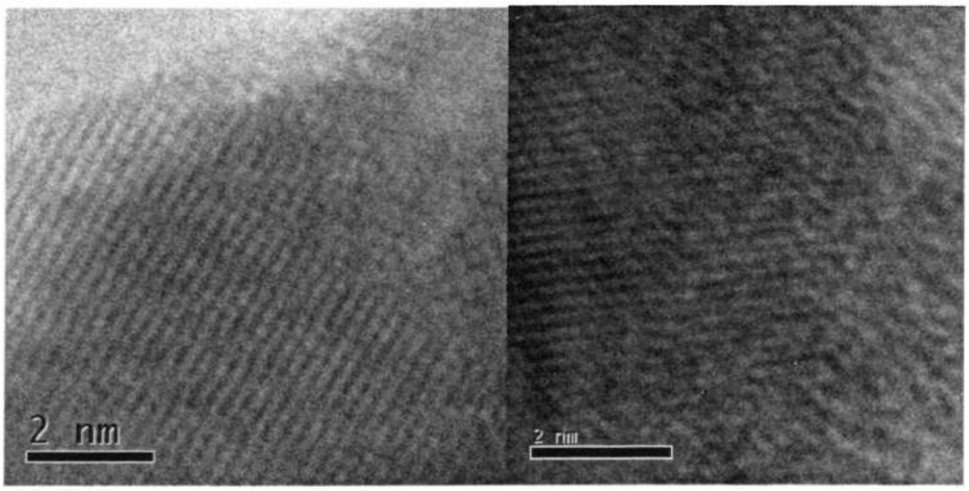

Figure 5.8 High magnification of cross-section TEM image in two different regions of DMS thin films. Scale bar: 2 nm.

From the experiments demonstrated above, it shows that oxygen partial pressure would affect the ferromagnetic property of DMS thin films. In order to study further this factor, samples deposited at different oxygen partial pressure were investigated. The results will be discussed in the next section.

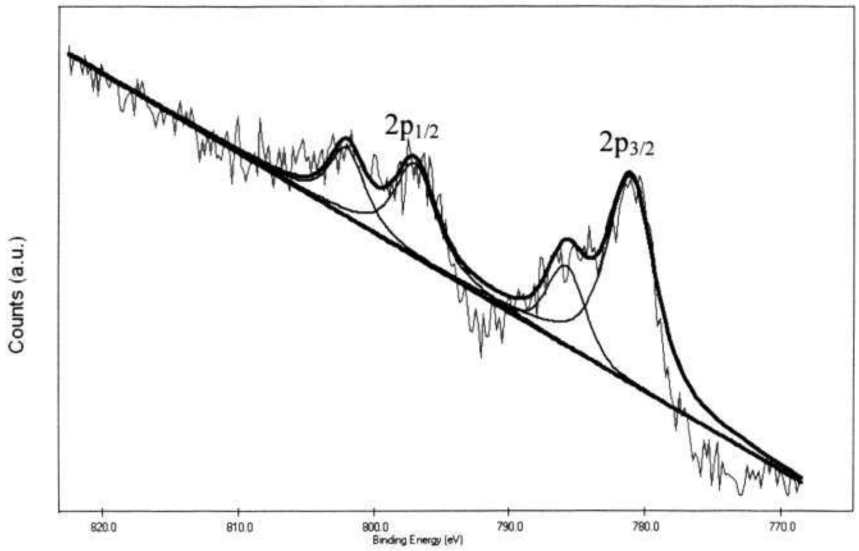

Figure 5.9 X-ray photoelectron spectroscopy (XPS) studies of Co $2p_{3/2}$ and $2p_{1/2}$ peaks for the DMS thin film.

5.4 Effects of Oxygen Partial Pressure – BMP Model

Figure 5.10 (a) shows the XRD patterns of the $Zn_{0.95}Co_{0.05}O$ thin films deposited on silicon substrates at 5 x 10^{-3} Torr, 5 x 10^{-4} Torr, 5 x 10^{-5} Torr and 5 x 10^{-6} Torr oxygen partial pressures with the substrate temperature fixed at 450°C. The XRD results indicate that all the samples deposited are single phase with wurtzite structure. Moreover, a (103) intensity peak is located at $\theta = 31.34^{\circ}$, which is very close to the calculated inter-plane angle of 31.66° between (103) and (002) planes in the wurtzite structure, indicating that the $Zn_{0.95}Co_{0.05}O$ thin films have (002) preferential orientation as mentioned in section 4.4.

Figure 5.10 (b) shows the full width at half maximum of the DMS thin films prepared at different oxygen partial pressure. It shows than when the oxygen partial pressure increased from 5 x 10^{-6} Torr to 5 x 10^{-3} Torr, the FWHM decreased from 0.38 ° to 0.31 °. There are two factors which affect the FWHM. One is grain size, and the other is oxygen deficiency. For samples prepared in lower oxygen partial pressure, oxygen deficiency would be the main reason for this increase in FWHM. The oxygen deficiency would affect the crystal symmetry, such that it broadens the peaks. Therefore, at lower oxygen partial pressure, more oxygen deficiency was generated in the DMS thin films. This would imply that the number of oxygen vacancies would be higher for samples that were prepared at lower oxygen partial pressure.

Figure 5.11 shows the cross section HRTEM images of $Zn_{0.95}Co_{0.05}O$ thin film deposited at 450°C under various oxygen partial pressures. The thickness of the films was around 160 nm. From Figure 5.11, the $Zn_{0.95}Co_{0.05}O$ lattice fringes are observed to be in parallel, which shows that the $Zn_{0.95}Co_{0.05}O$ thin films deposited on silicon substrate are single phase with wurtzite structure. The distance between neighboring lattice fringes was measured to be 0.26 nm, which is the (002) inter-plane spacing in wurtize ZnO, confirming that the $Zn_{0.95}Co_{0.05}O$ thin film has a (002) preferential orientation. There are some defects such as edge dislocations, which are indicated with white arrows in the TEM results. It was easier to observe defects in samples deposited at a relatively lower oxygen partial pressure. In order to study the crystal structure clearly, selected area electron diffraction (SAED) patterns of the $Zn_{0.95}Co_{0.05}O$ thin films were carried out as shown in Figure 5.12. Its zone axis is [100], and the diffraction pattern shows that the $Zn_{0.95}Co_{0.05}O$ thin films grew along the [001] direction. For the defects observed in the $Zn_{0.95}Co_{0.05}O$ thin films, they could be formed due to the difference in ionic radius between cobalt (0.75 Å) and zinc (0.74 Å), as well as the low oxygen pressure which resulted in more oxygen vacancies formation.

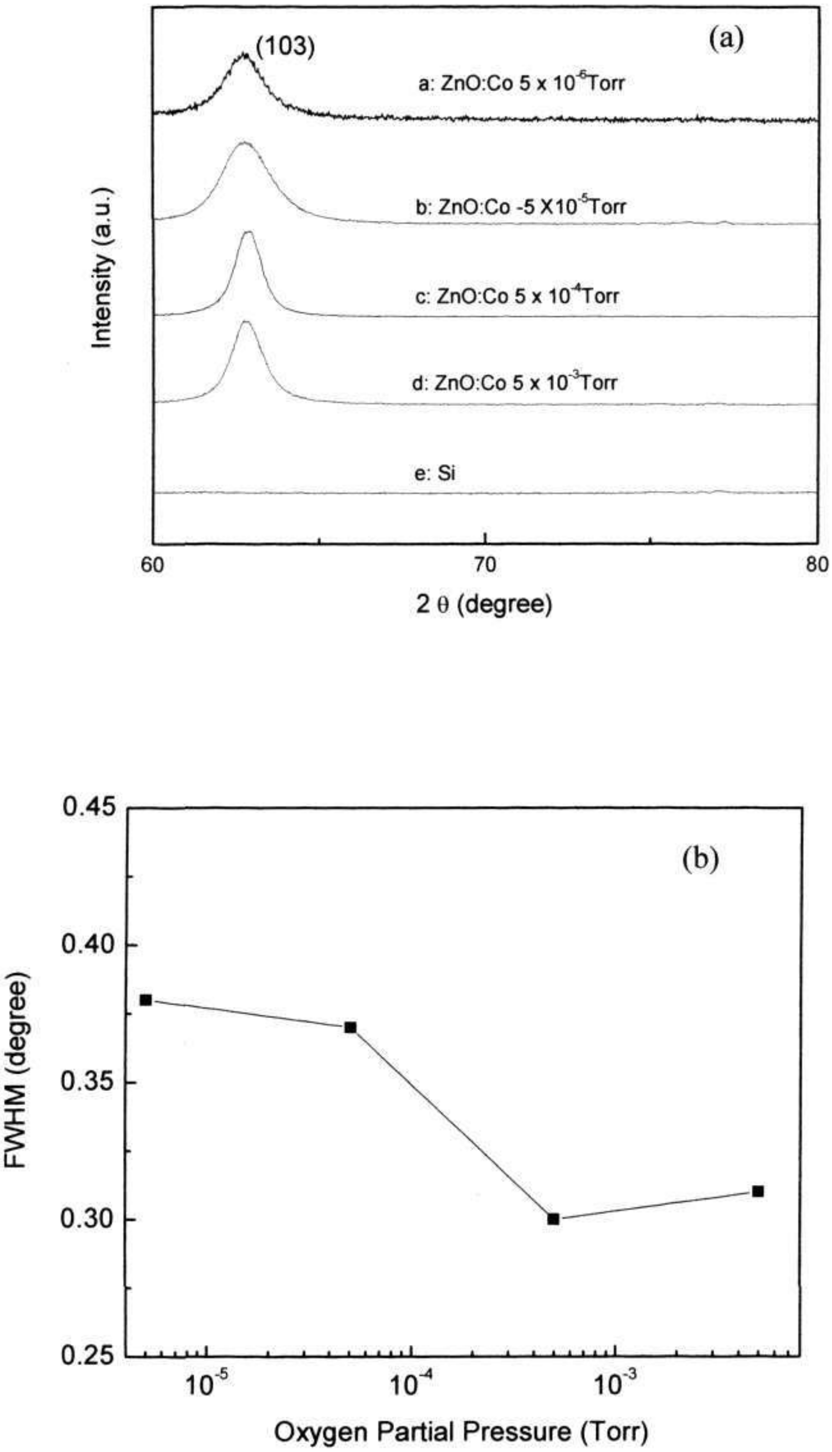

Figure 5.10 (a) X-Ray diffraction patterns of Si substrate and $Zn_{0.95}Co_{0.05}O$ thin films deposited at 5 x 10^{-3} Torr, 5 x 10^{-4} Torr, 5 x 10^{-5} Torr and 5 x 10^{-6} Torr. (b) FWHM of $Zn_{0.95}Co_{0.05}O$ thin films shown in (a).

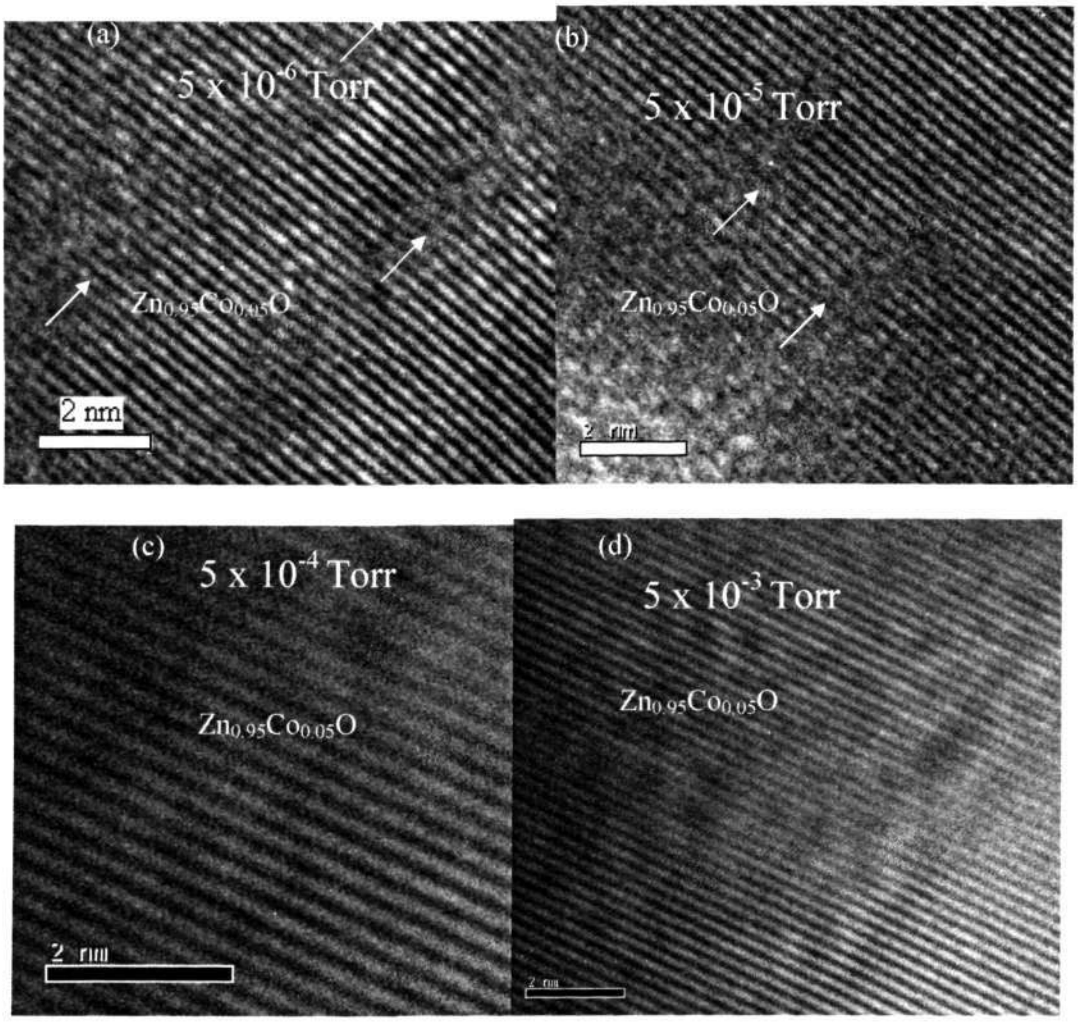

Figure 5.11 HRTEM images of $Si/SiO_2/Zn_{0.95}Co_{0.05}O$ thin film prepared at (a) 5 x 10^{-6} Torr, (b) 5 x 10^{-5} Torr, (c) 5 x 10^{-4} Torr, and (d) 5 x 10^{-3} Torr.

Figure 5.13 shows the XPS measurements for samples prepared at different oxygen partial pressure. No difference is observed among these samples prepared at different oxygen partial pressure. All the peaks in the XPS measurement data show that the cobalt in the $Zn_{0.95}Co_{0.05}O$ thin film has bivalence charge state. The core level for *metallic* Co $2p_{3/2}$ is at 778.3 eV and the energy difference between Co $2p_{3/2}$ and $2p_{1/2}$ is 14.97 eV. However, no peak was detected at 778.3 eV. Instead, the peaks are located at 780.09 eV and 796.09 eV for cobalt $2p_{3/2}$ and $2p_{1/2}$ respectively, which correspond to Co-O bonds. These results are comparable to the ones reported by Lee *et al.* [74].

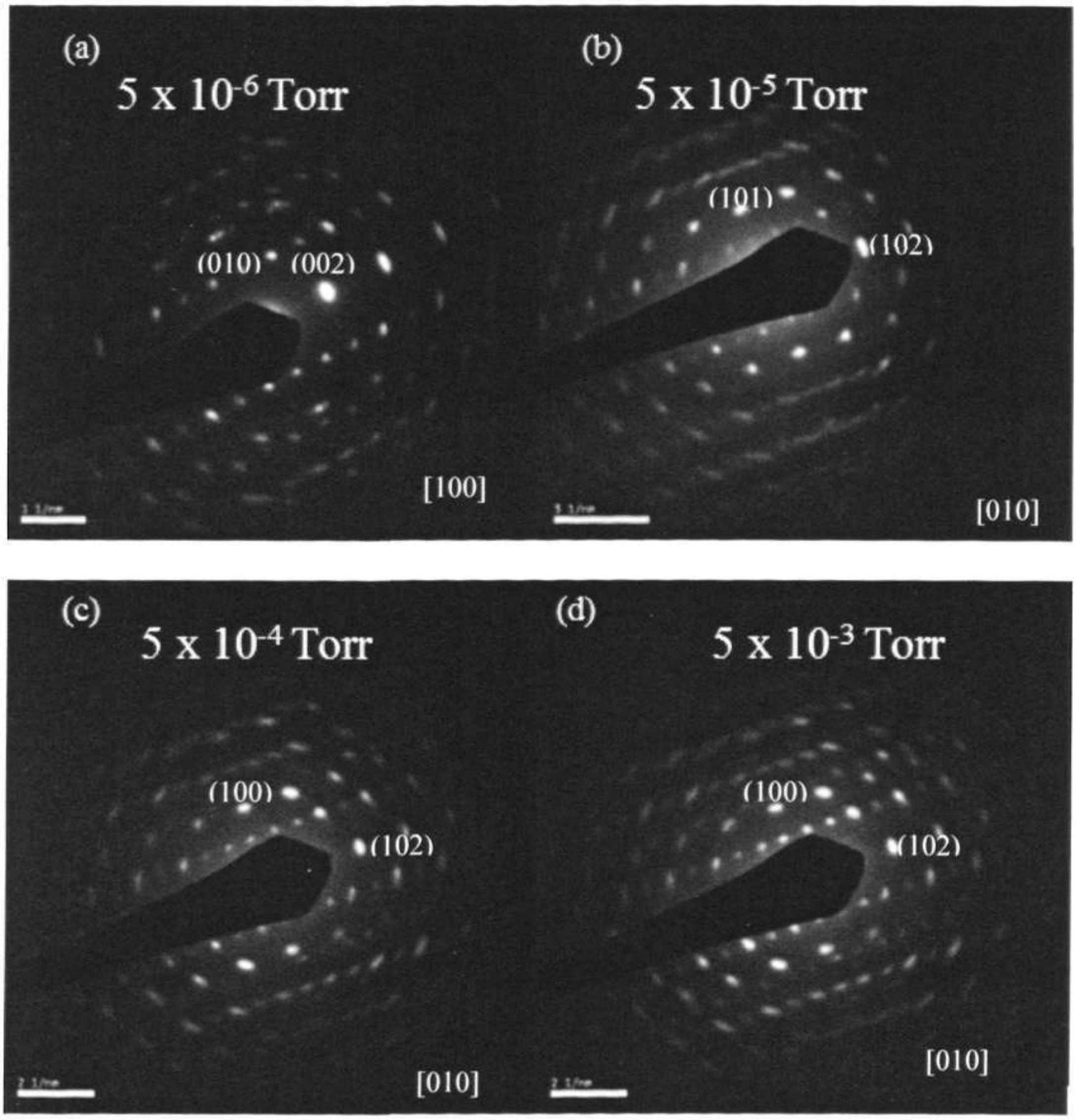

Figure 5.12 Selected area diffraction patterns of $Zn_{0.95}Co_{0.05}O$ thin film prepared at (a) 5 x 10^{-6} Torr, (b) 5 x 10^{-5} Torr, (c) 5 x 10^{-4} Torr, and (d) 5 x 10^{-3} Torr.

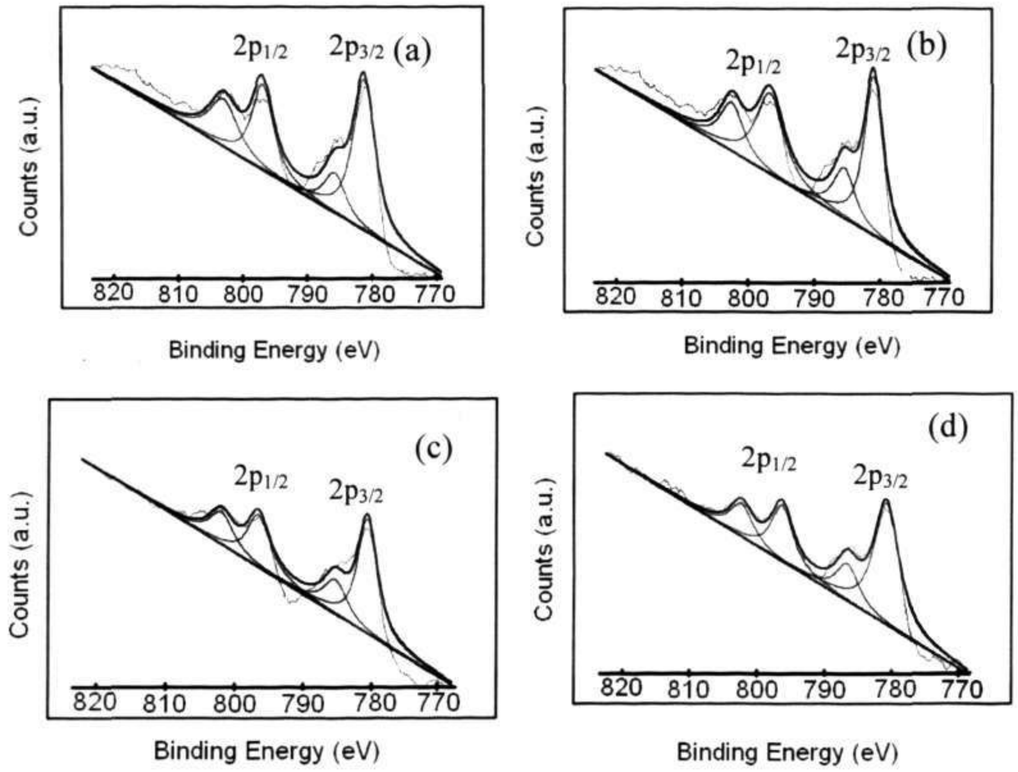

Figure 5.13 XPS analysis of core levels for cobalt $2p_{3/2}$ and $2p_{1/2}$ peaks in $Zn_{0.95}Co_{0.05}O$ thin film prepared at (a) 5 x 10^{-6} Torr, (b) 5 x 10^{-5} Torr, (c) 5 x 10^{-4} Torr, and (d) 5 x 10^{-3} Torr oxygen partial pressure.

In order to demonstrate the presence of oxygen vacancies and further investigate their impact more directly, PL characterization was carried out first. The samples were then post-annealed in an oxygen rich ambient, followed by measuring the M-H curves. Figure 5.14 shows the PL measurements before post-annealing. From this PL result, it shows that before annealing, a peak around 525 nm, which corresponds to the oxygen vacancies, was observed [140]. It has been reported in Ming-Kwei Lee's group that PL intensity is related to the volume of the material activated. In ZnO, normalized intensity of 525 nm (normalized to intensity at 378 nm) corresponds to the normalized total oxygen vacancies (normalized to activated ZnO volume) [181]. By comparing the intensity of peaks at 525 nm with the band emission at 378 nm, the relative height increased when the oxygen partial pressure was reduced. It indicates that the amount of oxygen vacancies was increased.

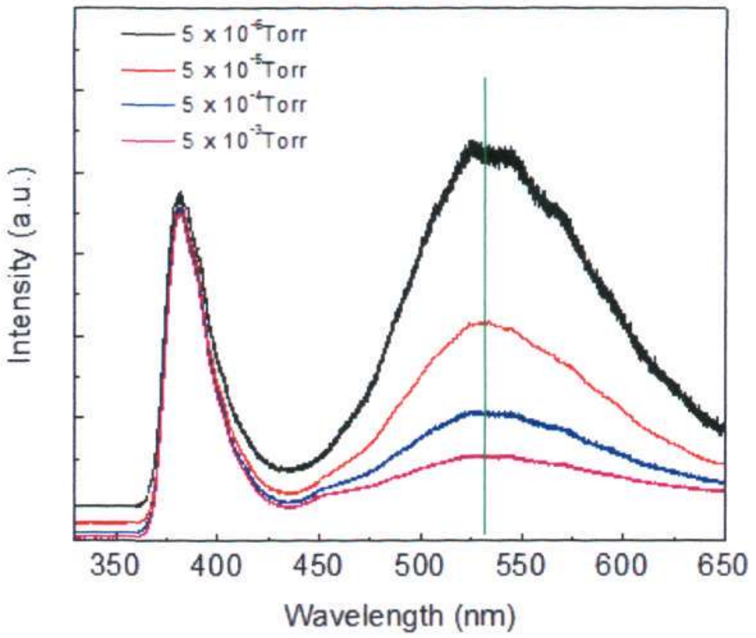

Figure 5.14 PL for Co-doped ZnO thin films prepared at different oxygen partial pressure.

Figure 5.15 (a) shows the magnetization versus field curves measured by SQUID for $Zn_{0.95}Co_{0.05}O$ thin film deposited at different oxygen partial pressure with the substrate temperature fixed at 450°C. Figure 5.15 (b) shows the corresponding saturation magnetization of the $Zn_{0.95}Co_{0.05}O$ thin films deposited at different oxygen partial pressure. A highest saturation magnetization of 0.86 μ_B/Co (normalized by the actual Co content as measured from XPS) was observed for $Zn_{0.95}Co_{0.05}O$ thin film deposited at 5 x 10^{-6} Torr. Moreover, it clearly shows that at lower oxygen partial pressure, M_s is much larger than the films deposited at relatively higher oxygen partial pressures. Nevertheless, the highest saturation moment observed is still smaller than the saturation moment of metallic cobalt, which is 1.7 μ_B/Co. It has been discussed in previous section that the room temperature ferromagnetism is not due to the metallic cobalt clusters. According to the HRTEM result and XPS data, it further proves that no cobalt clusters was observed. It also revealed that the cobalt detected in the $Zn_{0.95}Co_{0.05}O$ thin films is Co^{2+} ions from XPS data.

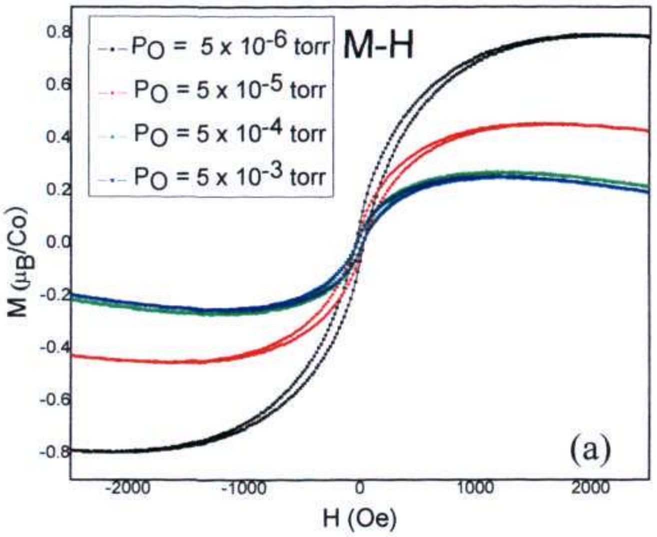

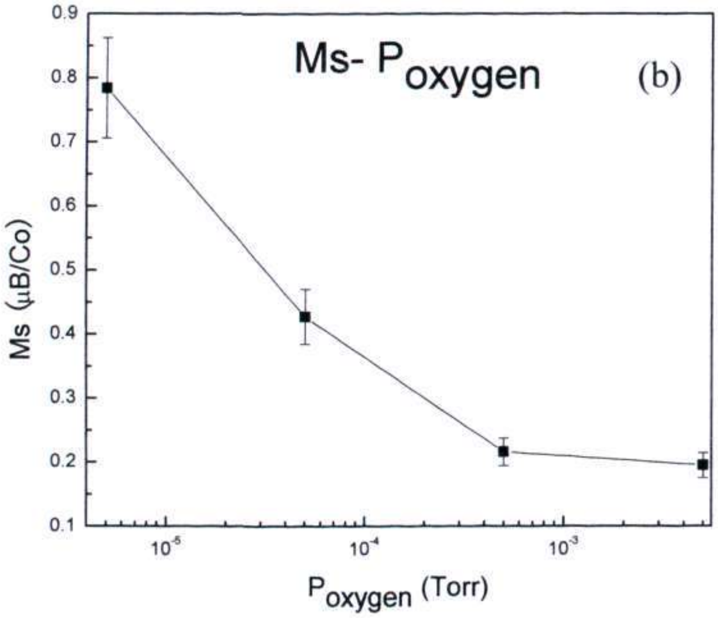

Figure 5.15 (a) SQUID measurement for ferromagnetic behavior under room temperature. (b) Saturation moment as a function of deposition oxygen partial pressure.

Figure 5.16 shows the PL measurement results after annealing the samples in oxygen at 450°C. Form the PL data, it shows that after annealing in high oxygen pressures, the amount of oxygen vacancies would reduce. It also shows that the peak at 375 nm due to the band edge is still strong, and the full width at half maximum is smaller, which implies better crystal quality. The peak that is due to the oxygen vacancies at 525 nm cannot be detected clearly.

Figure 5.17 shows the M-H loop measured after post annealing. From these data, it shows that the saturation magnetization was much smaller than those prepared as deposited. This is because less oxygen vacancies remained in the DMS thin films after the samples were annealed in the oxygen-flowed ovens. The contribution of metallic cobalt to the room temperature ferromagnetism of DMS thin films has been ruled out previously. There is a possibility that the cobalt was in the form of cobalt nanoclusters after the annealing. In this case, there are two possibilities: 1) They form metallic cobalt nanoclusters. However, the saturation magnetization of these films after annealing are much smaller than the DMS thin films before annealing, which shows that the oxygen vacancies would affect the magnetic properties in these samples. 2) They form Co^{2+}-O-Co^{2+} nanoclusters. Although some groups reported that the magnetic properties in Co^{2+}-O-Co^{2+} nanoclusters are due to the uncompensated moment on the surface, the low temperature magnetization does not exceed $0.05\mu_B$/Co at 2 T, which is lower than the saturation magnetization in our DMS thin films after annealing [182]. Oxygen vacancies also play a role for the ferromagnetic properties. Thus, the oxygen vacancies have been shown to play an important role.

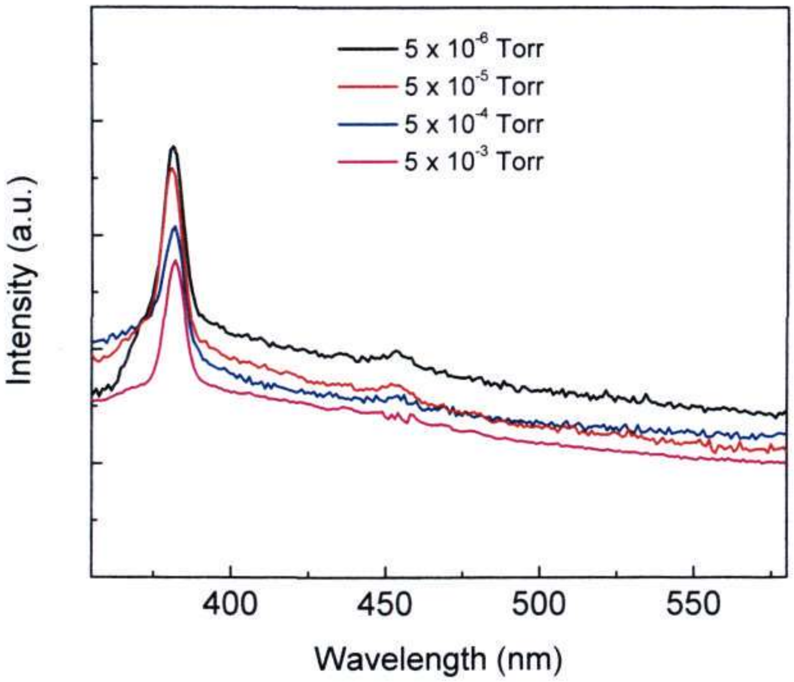

Figure 5.16 PL for the samples after being annealed in an oxygen rich ambient.

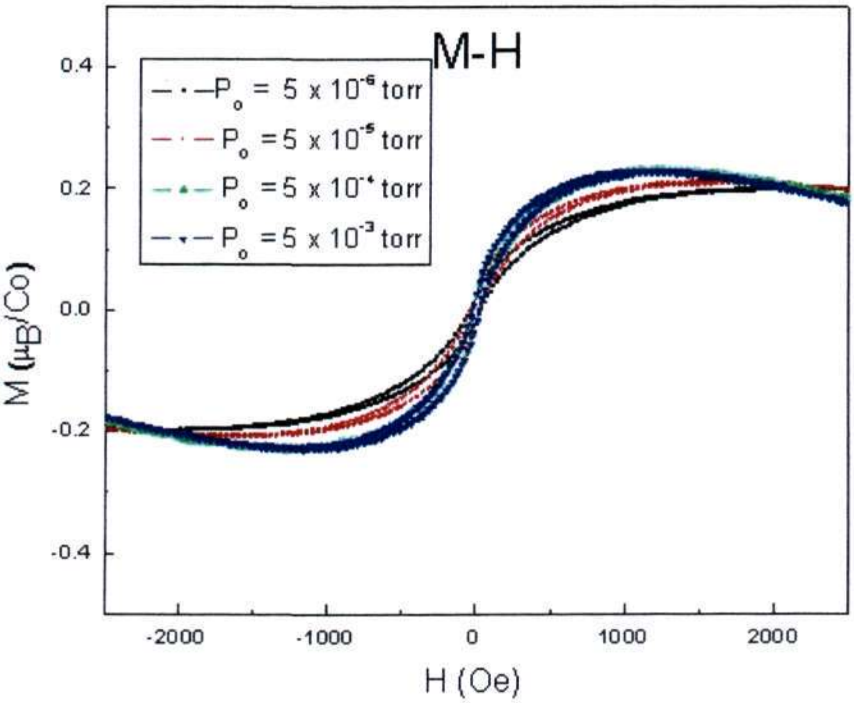

Figure 5.17 M-H curves for samples after being annealed in an oxygen rich ambient.

By studying the samples prepared at different oxygen partial pressures, it was found that the oxygen partial pressure affect the magnetic properties of DMS thin films. Bound magnetic polarons (BMP) model [127] could be the mechanism which explains the observed room temperature ferromagnetism in DMS thin films. In this model, ferromagnetism is mediated though localized donor electrons in the impurity band. In order to obtain long range ferromagnetism order, a sufficiently large number of BMP is required, as the magnetic ions within the polaronic radius interact ferromagnetically. The important parameter in this model is the critical defect concentration ($N_{\square}^{c}$) for establishing the percolation threshold for long range ferromagnetism order. According to reference [127], $N_{\square}$ can be estimated from γ^{3} ($N_{\square}^{c}$ /$N_{\circ}$), where $N_{\circ}$ is the oxygen density for ZnO, and $\gamma = \varepsilon$ (m/m^{*}), where ε is the high frequency dielectric constant, m is the electron mass, and m^{*} is the effective mass of the donor electron. For ZnO, γ value is around 14, such that $N_{\square}^{c}$ is estimated to be around 3.8×10^{18} cm^{-3}. In order to give long range order, the critical defect density should be above the percolation value calculated above. The number of defects that interacts with a particle magnetic cation is directly related to the critical defect density in the form of $(4/3)\ \pi r_{H}^{3}\ N_{\square}$.

In our DMS thin films, the sample prepared at a relatively low oxygen partial pressure of 5×10^{-7} Torr has a sheet resistance of 32 mΩ·cm, while it is 93 mΩ·cm for the samples prepared at 5×10^{-4} Torr. From the Hall measurements, the defect density of these two samples is 2.5×10^{17}cm^{-3} and 3.2×10^{16}cm^{-3} respectively. From the SQUID measurement, it shows that the DMS sample prepared at 5×10^{-7} Torr oxygen partial has a M_s that is slightly larger than the DMS thin films prepared at 5×10^{-4} Torr oxygen partial pressure. This is due to the larger defect density (mainly are oxygen vacancies) in DMS samples prepared at 5×10^{-7} Torr oxygen partial pressure. However from our calculation, we find that the experimental density of defects is one order less than the estimated critical defect density. This is because the BMP model is based on the hard sphere approximation, such that a lower value would be expected in practice, and the threshold is also temperature dependent [55].

Besides the critical defect density, another important parameter is the magnetic cations percolation threshold. In this case, ferromagnetism only occurs when the defect density is above the critical defect density, and the magnetic cations concentration is less than the cation percolation threshold. From the BMP model, if the magnetic cations concentration is less than the percolation value, antiferromagnetic super exchange cannot create a long range order. At the most, it will interact with the nearest neighbor to give a local antiferromagnetic interaction, which will reduce the average moment per cation [127]. In our nanodots embedded ZnO thin films discussed in section 5.3, the interfacial layer between the cobalt nanodots and ZnO should be in the form of DMS Zn_xCo_yO. However, long range order was not detected, which may be due to the cation percolation. At the interfacial layer, the amount of doped Co would be much larger than the cation percolation threshold of 0.18 [127], which would result in local antiferromagnetic super exchange, such that the ferromagnetism properties were not detected.

The effective magnetic Hamiltonian as discussed in the previous chapter can be shown by the equation below.

$$H = \sum_{ij} J_F(r_{ij}) S_i \cdot S_j + \sum J_{AF} S_i \cdot S_j + \sum J_F^{'} S \cdot s \tag{5.1}$$

According to the above discussions, the third term at the right, which refers to the bound magnetic polaron model, can be expressed as:

$$\sum J_F^{'} N_f(r) S \cdot s \tag{5.2}$$

$$N_f = \frac{4}{3}\pi L^3 n_j^{v_o^{\bullet\bullet}} n_i f(r) \tag{5.3}$$

Here, N_f is the density of magnetic elements aligned, $n_j^{v_o^{\bullet\bullet}}$ is the density of oxygen vacancies related defects, n_i is the magnetic doping concentrations, L is the polarons radius, r is the distance between localized carriers and magnetic elements, and $f(r)$ denotes the effective interaction between magnetic cations with the localized donor electrons. If the amount of oxygen vacancies is increased, the number of aligned magnetic cations would increase as well. Saturated magnetization would then increase as a result.

However, one point that should be noted is that the RKKY and BMP model could coexist in the DMS system. As long as oxygen vacancies are present in the thin film, a certain amount of localized electrons would become delocalized due to thermal activation, such that the RKKY indirect interaction would be involved as well. When the amount of the oxygen vacancies are further increased, the amount of these delocalized electrons will correspondingly increase, and reflected in an increase in the RKKY ferromagnetic interaction. It has been shown that when the oxygen partial pressure increased from 5 x 10^{-6} Torr to 5 x 10^{-3} Torr, and assuming that all the defects gave delocalized carriers, the carrier concentration would change from 10^{17}cm^{-3} to 10^{16}cm^{-3}. Comparing this amount with the magnetic cation concentration of 10^{20}cm^{-3}, the carrier concentration is still much less than the magnetic cations concentration, such that the spin glass state will not be involved. It has been reported that if carriers' concentration increases, RKKY oscillation will occur. This would be the root cause for the spin glass properties [183]. The ferromagnetism alignment will not be suppressed due to this amount of delocalized carriers.

5.5 Effects of Substrate Temperature - RKKY Mechanism

Figure 5.18(a) shows the XRD patterns of the $Zn_{0.95}Co_{0.05}O$ thin films deposited on silicon substrates at 320°C, 400°C, 450°C and 500°C with an oxygen partial pressure of 5×10^{-6} Torr. The XRD results indicate that all the samples deposited are single phase with wurtzite structure. Moreover, a (103) intensity peak is located at $\theta = 31.38°$, which is very close to the calculated inter-plane angle of 31.66° between (103) and (002) planes in the wurtzite structure, indicating that the $Zn_{0.95}Co_{0.05}O$ thin films have (002) preferential orientation. Figure 5.18(b) shows that the full width at half maximum (FWHM) increased from 0.36° to 0.47° when the substrate temperature decreased from 500°C to 320°C. This may be due to smaller crystal sizes resulting from a lower deposition temperature, or the strains in the film and crystal symmetry that were affected by the substrate temperature during the deposition process. When the crystal size is reduced, the higher surface to volume ratio can lead to more surface related defects. During the sample deposition process, some defects could arise from the laser ablation. These defects could be physical and chemical, such as deviations in stoichiometry, film impurities, microcracks and pinholes which would affect the carrier transport [135]. In this case, more defects would be generated during the lower deposition temperature. At the same time, these samples were prepared under the same conditions except substrate temperature, so the strains contributed by other factors, except substrate temperature, should be the same in these samples. However, samples fabricated at substrate temperature ranging from 400°C to 500°C shows comparable strain in the thin films with thickness of 100 nm [178]. Therefore，overall at lower deposition temperature, more defects would be generated.

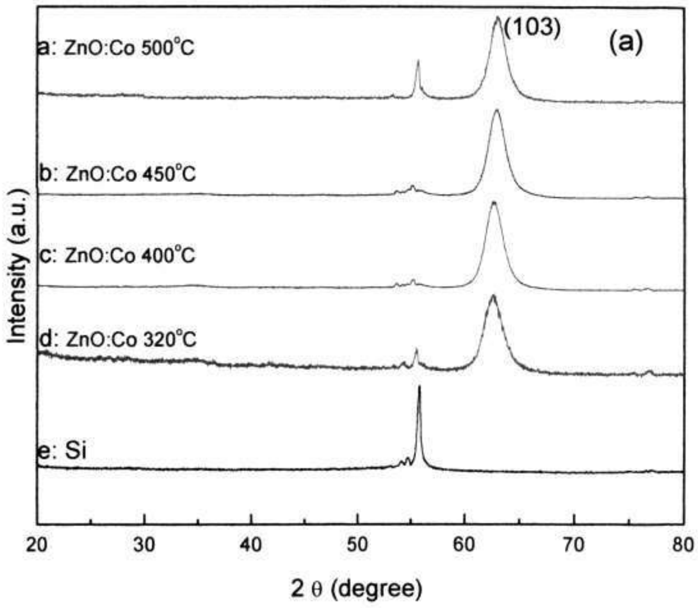

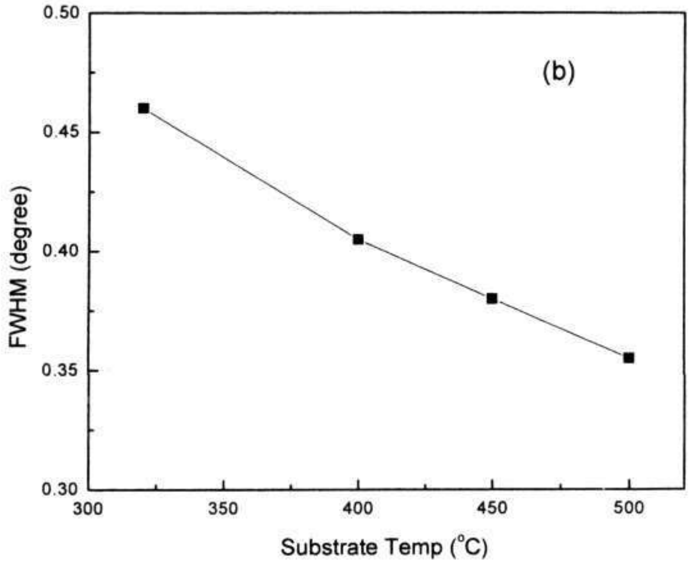

Figure 5.18 (a) X-Ray diffraction patterns of Si substrate and $Zn_{0.95}Co_{0.05}O$ thin films deposited at 320°C, 400°C, 450°C and 500°C. (b) FWHM of $Zn_{0.95}Co_{0.05}O$ thin films in (a).

Figure 5.19 (a), (b), (c) and (d) show the cross section TEM images of $Zn_{0.95}Co_{0.05}O$ thin films deposited at 320°C, 400°C, 450°C and 500°C, respectively with the oxygen partial pressure at 5×10^{-6} Torr. The thickness of the films was around 150 nm. The image shows an approximately 3 nm-thick layer of native SiO_2 between the silicon substrate and the $Zn_{0.95}Co_{0.05}O$ thin film. The difference in the intensity of the HRTEM image is due to the numerous defects formed during the thin film growth. Based on a limited number of TEM results, it can be calculated that the number of defects would be in the order of several per 100 nm^2. Figures 5.20 (a) and (b) show the HRTEM images of DMS thin films prepared at 320°C and 450°C. One observable defects is a dislocation as shown in the magnification in Figure 5.20 (b). It is observed that there are ten and eleven atomic layers on the left and right of the highlighted region respectively, indicating an edge dislocation in between. From Figure 5.19 and Figure 5.20, the $Zn_{0.95}Co_{0.05}O$ lattice fringes are observed to be in parallel, which shows that the $Zn_{0.95}Co_{0.05}O$ thin films deposited on the silicon substrate are single phase with wurtzite structure. The distance between neighboring lattice fringes was measured to be 0.26 nm, which is the (002) inter-plane spacing in wurtize ZnO, confirming that the $Zn_{0.95}Co_{0.05}O$ thin film has a (002) preferential orientation. In order to observe the crystal structure clearly, a selected area electron diffraction (SAED) pattern of the $Zn_{0.95}Co_{0.05}O$ thin film was carried out as shown in the Figure 5.20 (c). Its zone axis is [100], and the diffraction pattern shows that the $Zn_{0.95}Co_{0.05}O$ thin film grew along the [001] direction. For the defects observed in the $Zn_{0.95}Co_{0.05}O$ thin film, they may be formed due to the lattice mismatch between the silicon substrate with native oxide and the thin film,, ionic radius difference between cobalt (0.75 Å) and zinc (0.74 Å), as well as the low oxygen ambient pressure which resulted in more oxygen vacancies formation.

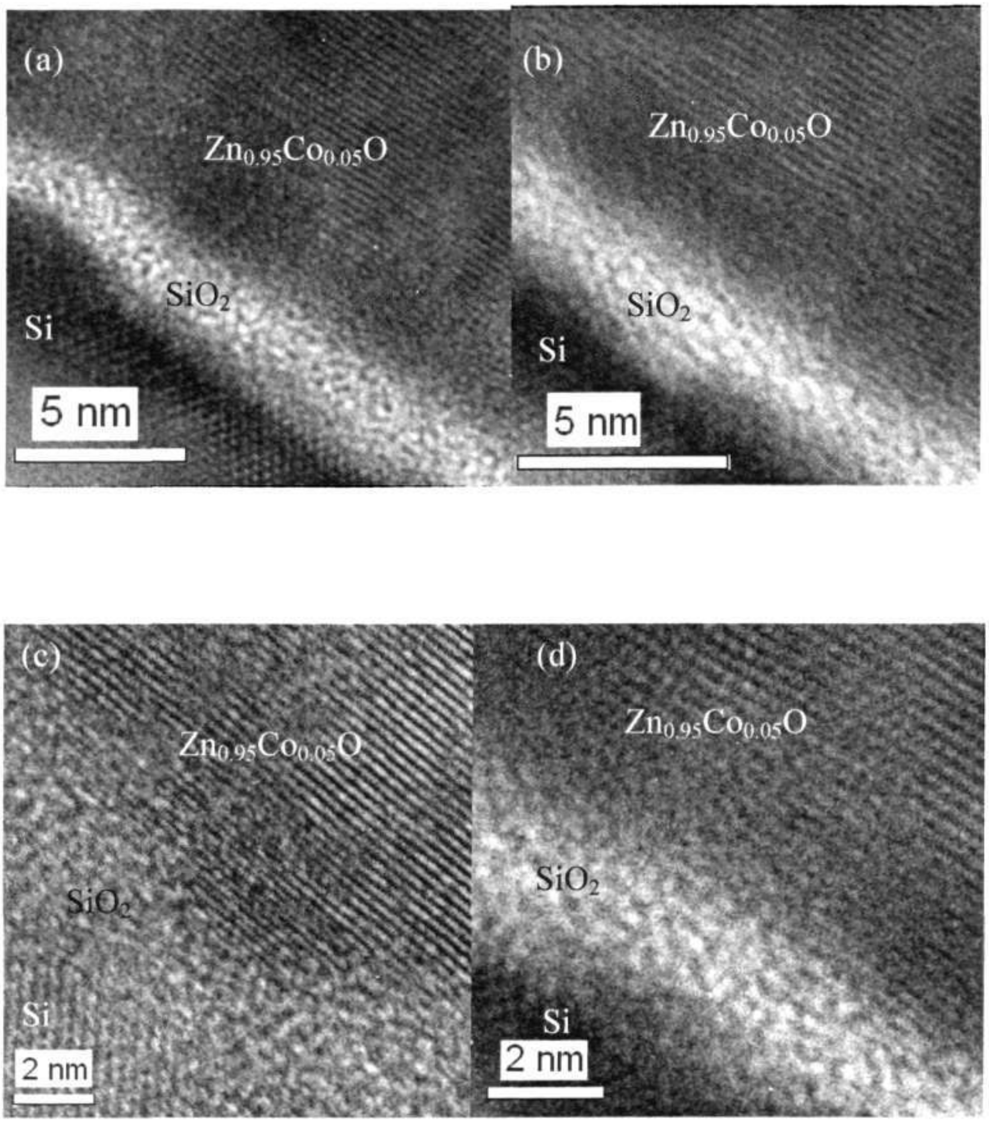

Figure 5.19 Cross-sectional TEM images of Si/SiO_2/$Zn_{0.95}Co_{0.05}O$ at different substrate temperature: (a) 320°C, (b) 400°C, (c) 450°C, (d) 500°C.

Figure 5.21 (a) shows magnetization versus field curves measured by a SQUID for $Zn_{0.95}Co_{0.05}O$ thin film deposited at different substrate temperatures with the oxygen partial pressure fixed at 5×10^{-6} Torr. Figure 5.21 (b) shows the corresponding saturation magnetization of the $Zn_{0.95}Co_{0.05}O$ thin films deposited at different temperature. A highest saturation magnetization of 0.80 μ_B/Co (normalized by the actual Co content measured from XPS which as discussed in the previous chapter) was observed for $Zn_{0.95}Co_{0.05}O$ thin film deposited at 450°C. Moreover, it shows that at low deposition temperature, M_s is much smaller than the films deposited at a relatively higher temperature. Furthermore, the highest saturation moment observed is still smaller than the saturation moment of metallic cobalt of 1.7 μ_B/Co. XPS data has revealed that the cobalt detected in the $Zn_{0.95}Co_{0.05}O$ thin film is Co^{2+} ions.

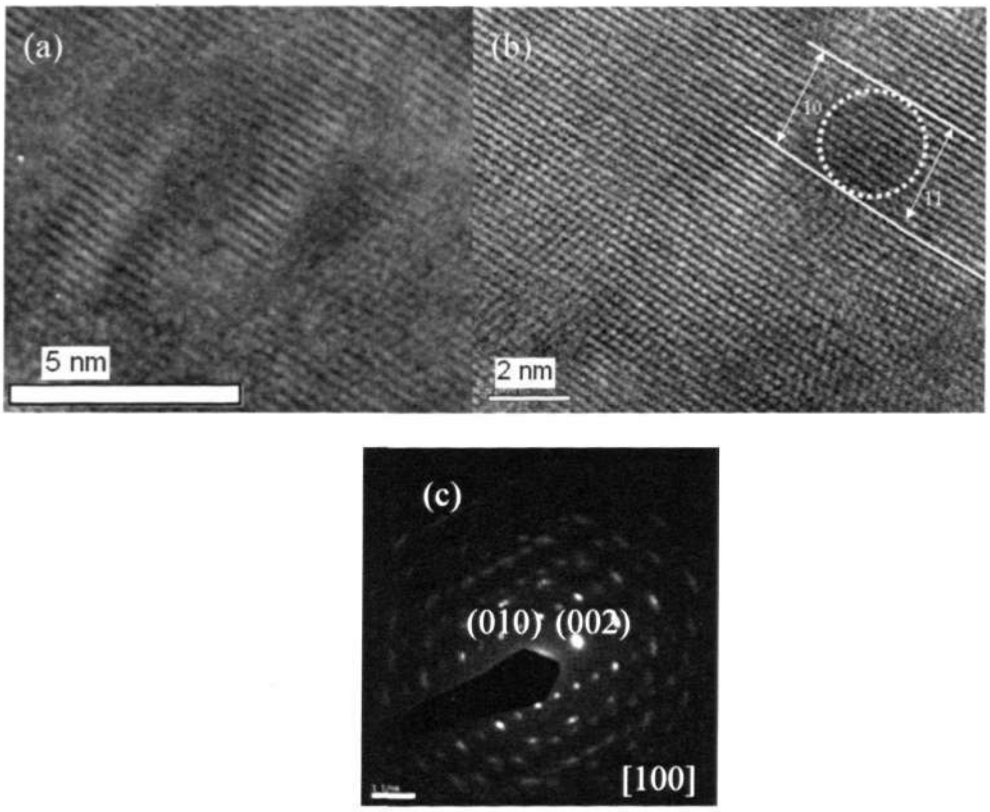

Figure 5.20 (a) and (b) HRTEM of $Zn_{0.95}Co_{0.05}O$ thin film prepared at 320°C and 450°C, the numbers indicate the number of atomic layers within the two lines. (c) SAED of the thin films prepared at 450°C.

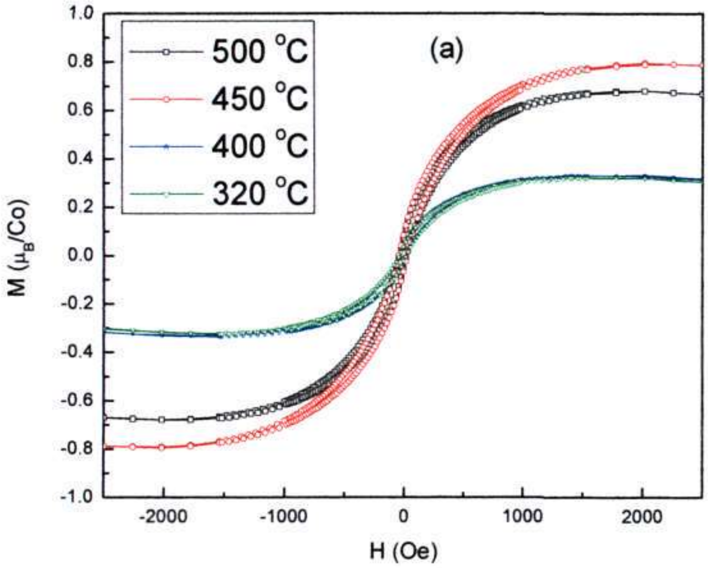

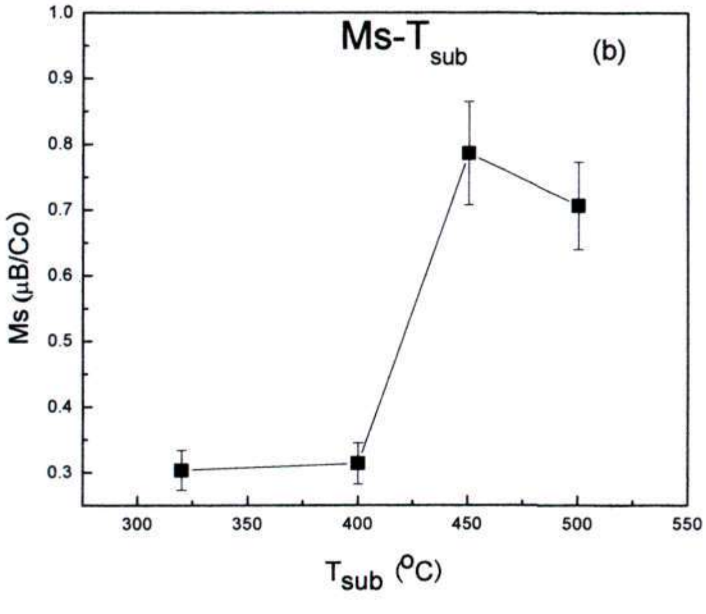

Figure 5.21 (a) SQUID measurements for ferromagnetic behavior under room temperature. (b) Saturation moment as a function of substrate deposition temperature.

The explanation of this room temperature ferromagnetism has been discussed in chapter 4, which comprise two contributions, the indirect interaction between magnetic cations through the delocalized carriers, and the interaction between localized electrons inside bound magnetic polarons with magnetic cations. By changing the substrate deposition temperature, $Zn_{0.95}Co_{0.05}O$ thin films deposited at relatively lower temperature (which are at 320°C and 400°C) have lower saturation moments than those $Zn_{0.95}Co_{0.05}O$ thin films deposited at higher temperature, as shown in Figure 5.21(b). According to the theoretical calculation, zinc interstitials, Zn_i, and oxygen vacancies, O_v, have relatively lower formation energies than other defects such as zinc vacancies and oxygen interstitials [136]. Some articles [137-139] have reported that high temperature treatment of ZnO or ZnO with Ga or Al doping under vacuum condition would give a higher resistivity of ZnO films, according to equations (5.4) and (5.5). Zinc interstitial- and oxygen vacancies-related free carrier concentrations were reduced as the substrate deposition temperature was increased.

$$Zn_{\mathrm{Zn}}^{\ x} \rightarrow Zn_i^{\bullet\bullet} + 2e^{'} \tag{5.4}$$

$$O_o^x \rightarrow \mathrm{V}_o^{\bullet\bullet} + 2e' + \frac{1}{2}O_2(g) \tag{5.5}$$

where $Zn_{\mathrm{Zn}}^{\ x}$ and O_o^x denote neutral charge zinc and oxygen ions located at their lattice site respectively, $Zn_i^{\bullet\bullet}$ is a zinc interstitial ion with double positive charge, $\mathrm{V}_o^{\bullet\bullet}$ is an oxygen vacancy with double positive charge and e' is an electron.

At higher deposition temperatures, a smaller amount of zinc interstitials and oxygen vacancies related defects were formed in $Zn_{0.95}Co_{0.05}O$ thin films. By considering the BMP model, less localized electrons would be generated during the sample preparation, and the ferromagnetic alignment should become poorer. However, better crystal symmetry and less lattice defects were observed at higher temperatures as the FWHM is smaller. These one and two dimensional defects (such as edge dislocations) would affect the free carriers (electron and hole) transport in terms of its mean free path. At lower deposition temperature, the crystal quality is poorer, which will give a smaller mean free path for carriers. The smaller mean free path will affect the carrier-induced ferromagnetic RKKY coupling, and the ferromagnetic RKKY coupling is suppressed. The inter-impurity interaction has random sign, which leads to a type of disordered random glassy non-ferromagnetic ground state.

It is perfectly reasonable to improve the ferromagnetic properties by improving the mean free path with the fixed doping concentration and carrier concentration. However, in ZnO-based system, the free carriers are generated from the defects. If the mean free path is increased, the defects density would have to be reduced, and which would suppress the carrier mediated RKKY coupling and the localized electron coupling with the magnetic cations with the polarons. It is shown that in the RKKY model, besides the magnetic cation concentration and carrier concentration, another important parameter is the mean free path which plays a role in the room temperature ferromagnetism properties. Thus, both the free carriers concentration and transportation of these free carriers affect the observed carrier induced ferromagnetism. Due to the counter-balancing of these two effects, carrier induced ferromagnetism in $Zn_{0.95}Co_{0.05}O$ thin films deposited at 450°C gave the highest saturation magnetization.

5.6 Summary

In summary, ZnO thin films doped with low concentration (5%) of Co and ZnO thin films embedded with cobalt nanodots have been fabricated using pulsed laser deposition technique at different oxygen partial pressures (5×10^{-7} Torr and 5×10^{-4} Torr). The results indicate that the ferromagnetism observed in DMS thin films at room temperature at 5×10^{-4} Torr is not due to the presence of cobalt nano-clusters, but Bound Magnetic Polarons with localized donor electrons are more likely to produce the long range magnetic orders in the room temperature ferromagnetism in DMS thin films. The number of aligned magnetic cations can be determined by the defects density and cations doping level.

Different ferromagnetism behavior at different deposition oxygen partial pressure was observed. This phenomenon may be due to oxygen vacancies related defects in the samples. The bound magnetic polarons concentration would be much larger for the sample prepared at a relatively lower oxygen partial pressure. The carrier-induced ferromagnetism model was investigated further by studying the impact of different deposition temperature. The difference in ferromagnetism behavior may have arisen from the opposing temperature dependence of Zn interstitials and oxygen vacancies related defects concentration (free carriers concentration), and crystal symmetry and lattice defects (affecting the transportation of free carriers) in $Zn_{0.95}Co_{0.05}O$ DMS. Including the delocalized carrier concentration and magnetic cations concentration, the mean free path of the delocalized carriers also plays a role in the room temperature ferromagnetism.

Chapter 6 External Electric Field Control of Ferromagnetism

6.1 Introduction

Magnetic materials are used in the information technology for storage purposes. However, for conventional electronic devices, data can be stored by the electronic charge inside semiconductors, such that this data can be read or written by applying an external electric field. Therefore, the ability to externally control the ferromagnetic behavior of DMS materials would be useful for actual device applications. Here, we demonstrate electric field control of the ferromagnetism in Co-doped ZnO thin film, using an insulating gate field effect transistor (FET) structure. It will also be shown the effect of the carriers density to the ferromagnetism properties in the DMS thin films, which implies the indirect RKKY interaction mechanisms.

6.2 Experiment Details

To fabricate the metal-insulator-semiconductor structure, a gold layer was first sputtered on top of silicon substrate with titanium as a buffer layer. Next, layers of $Zn_{0.9}Al_{0.1}O$ and $Zn_{0.95}Co_{0.05}O$ were deposited on top of this gold layer using pulsed laser deposition technique. A KrF pulsed laser beam of 248 nm wavelength and energy density of 1.4 J /cm^2 with a frequency of 10 Hz was used to ablate the target in an ultra-high vacuum chamber. The deposition and growth of the films on the substrate were carried out in a high vacuum system with an oxygen partial pressure of about 5×10^{-7} Torr with the target rotating at about 20 rounds/min at room temperature. Co-doped ZnO and Al doped targets were prepared by using a solid state reaction process between ZnO and Co_3O_4 or ZnO and Al_2O_3 powders. High purity (>99.9%) ZnO, Al_2O_3 and Co_3O_4 powders were weighed and mixed. The powders were grounded with ethanol in an agate ball-milling machine for 12 hours to obtain a homogeneous mixture. The powder was then dried, cold pressed and sintered at 1200°C for 12 hours.

6.3 External Electric Field

Figure 6.1 (a) shows the cross-sectional TEM image of the metal-insulator-semiconductor (MIS) structure. The semiconductor structure is composed of 200 nm-thick dilute magnetic $Zn_{0.95}Co_{0.05}O$ and 180 nm-thick N-type $Zn_{0.9}Al_{0.1}O$. Al_2O_3 with different thickness act as the insulating layers. The 10 nm-thick dielectric layer between $Zn_{0.95}Co_{0.05}O$ and $Zn_{0.9}Al_{0.1}O$ serves as the tunneling layer, while the 90 nm-thick Al_2O_3 layer below the Au serves as an insulating layer. The lattice mismatch between Al_2O_3 and ZnO is expected to be quite small [77]. Figure 6.1 (b) is the high resolution image (HRTEM) of the $Zn_{0.95}Co_{0.05}O$ thin film layer. It shows that the DMS layer is polycrystalline. The crystal structure is the same as in previous samples which were deposited directly on silicon substrate [78]. No second phase was observed from the TEM image.

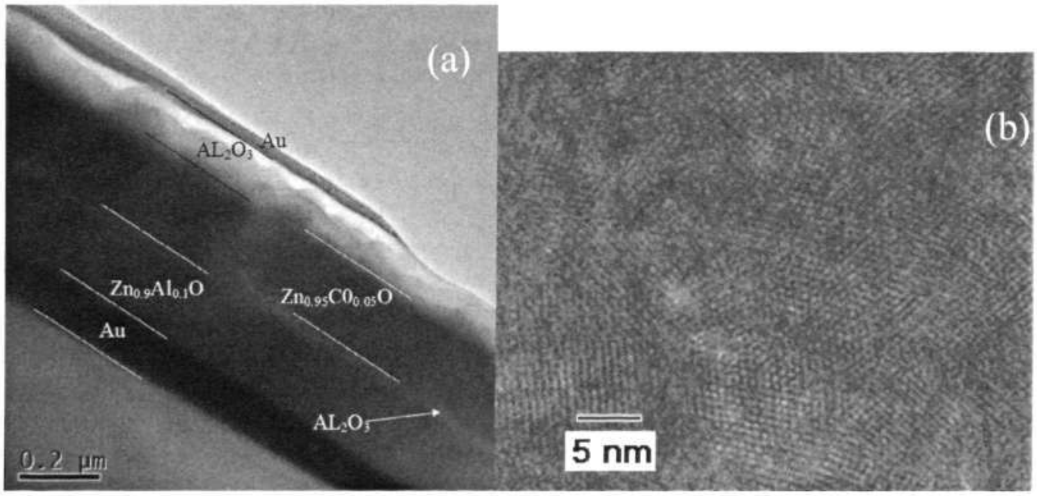

Figure 6.1 (a) Cross sectional TEM image of the metal-insulator-semiconductor structure. (b) Top view of the HRTEM image of the $Zn_{0.95}Co_{0.05}O$ layer.

Figure 6.2 (a) shows the M-H curves for the DMS layer measured at 5 K, while Figure 6.2(b) shows the saturated magnetization of this layer with error bars as a function of the external field. The saturated magnetization of this DMS layer was almost the same at different forward biases, which is approximately 0.5 μ_B/Co. It shows that the external forward field does not increase the magnetization at this low temperature. At such a low temperature, electrons have a low thermal energy, such that the electron movement will be less as compared to the movement at room temperature.

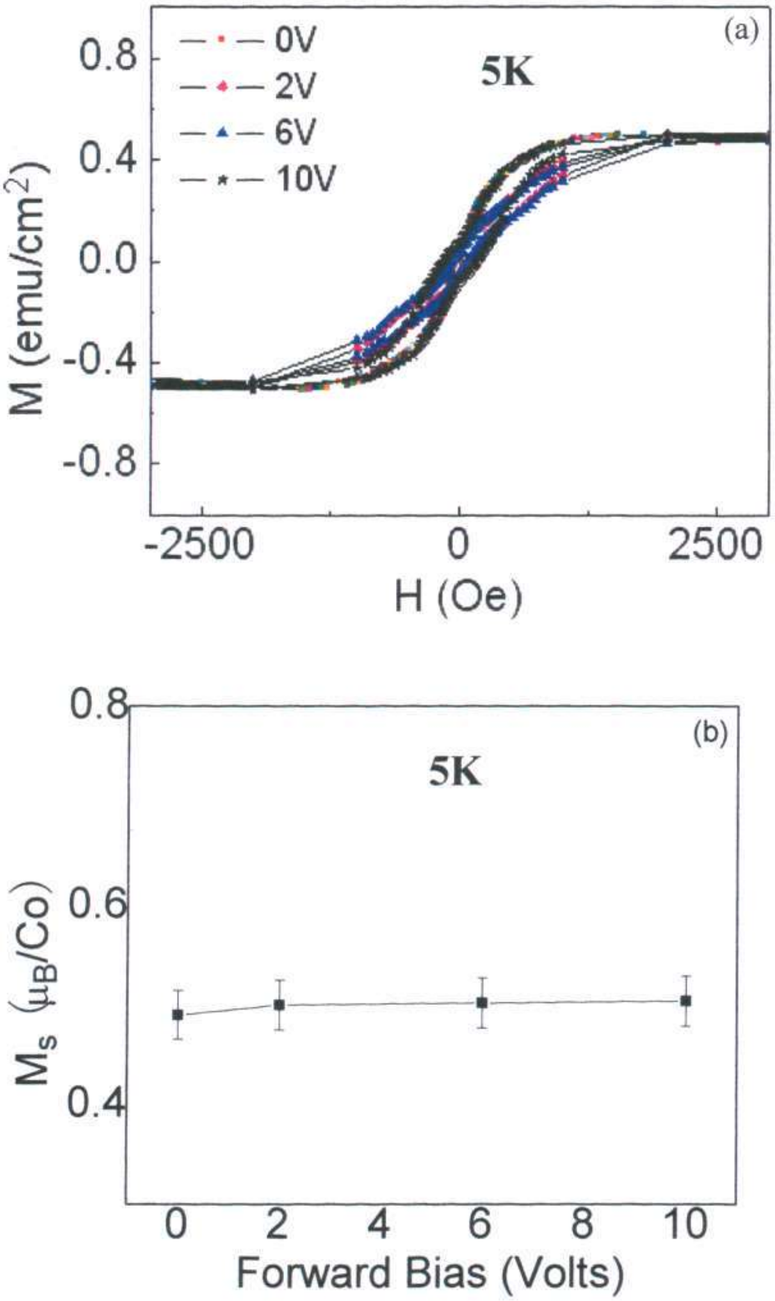

Figure 6.2 (a) Magnetization as a function of field (M-H curves) measured at 5 K by SQUID at different forward bias voltages; (b) Corresponding saturated magnetization as a function of applied forward voltages.

Figure 6.3(a) shows the room temperature M-H curves for the dilute magnetic semiconductor. Saturated magnetization of this DMS layer increases from 0.4 μ_B/Co to 0.50 μ_B/Co when the forward bias voltage increases from 0 V to 2 V. The inset shows the enlarged area of the highlighted region. It shows that H_c increased as well when the external applied voltage was increased. Figure 6.3(b) plots the saturated magnetization with error bars of this layer. It shows that the saturated magnetization increased with external applied electric field. In order to investigate the possible tunneling of the thin dielectric layer, a characterization of the MIM structure was carried out. From the I-V measurement shown in the inset of Figure 6.3 (b), the thin dielectric layer was tunneled through when the external field was at 2 V.

Figure 6.4 (a) shows the 400 K M-H curves for the dilute magnetic semiconductor. Saturated magnetization of this DMS layer increased from 0.3 μ_B/Co to 0.40 μ_B/Co when the forward bias voltage was increased from 0 V to 2 V. The inset again shows that the H_c increased as well when the external applied voltage was increased. However, for the initial three points, which has the bias voltage of 0V, 0,8V, 1.5V, the H_c are almost the same. Figure 6.4 (b) plots the saturated magnetization of this layer with error bars. It shows that with an external electric field, the magnetization would increase. Figure 6.5 (a) shows the 400 K M-H curves for the dilute magnetic semiconductor. Saturated magnetization of this DMS layer increased from 0.3 μ_B/Co to 0.46 μ_B/Co when the forward bias voltage increased from 0 V to 6 V. However, when the external field was increased further, the magnetic properties reduced from 0.46 μ_B/Co to 0.4 μ_B/Co. The inset shows the enlarged plot. It shows that the H_c increased when the external forward bias voltage increased from 0 V to 6 V. It reduced when the bias voltage further increased to 10 V. Figure 6.5 (b) plots the saturated magnetization of this layer.

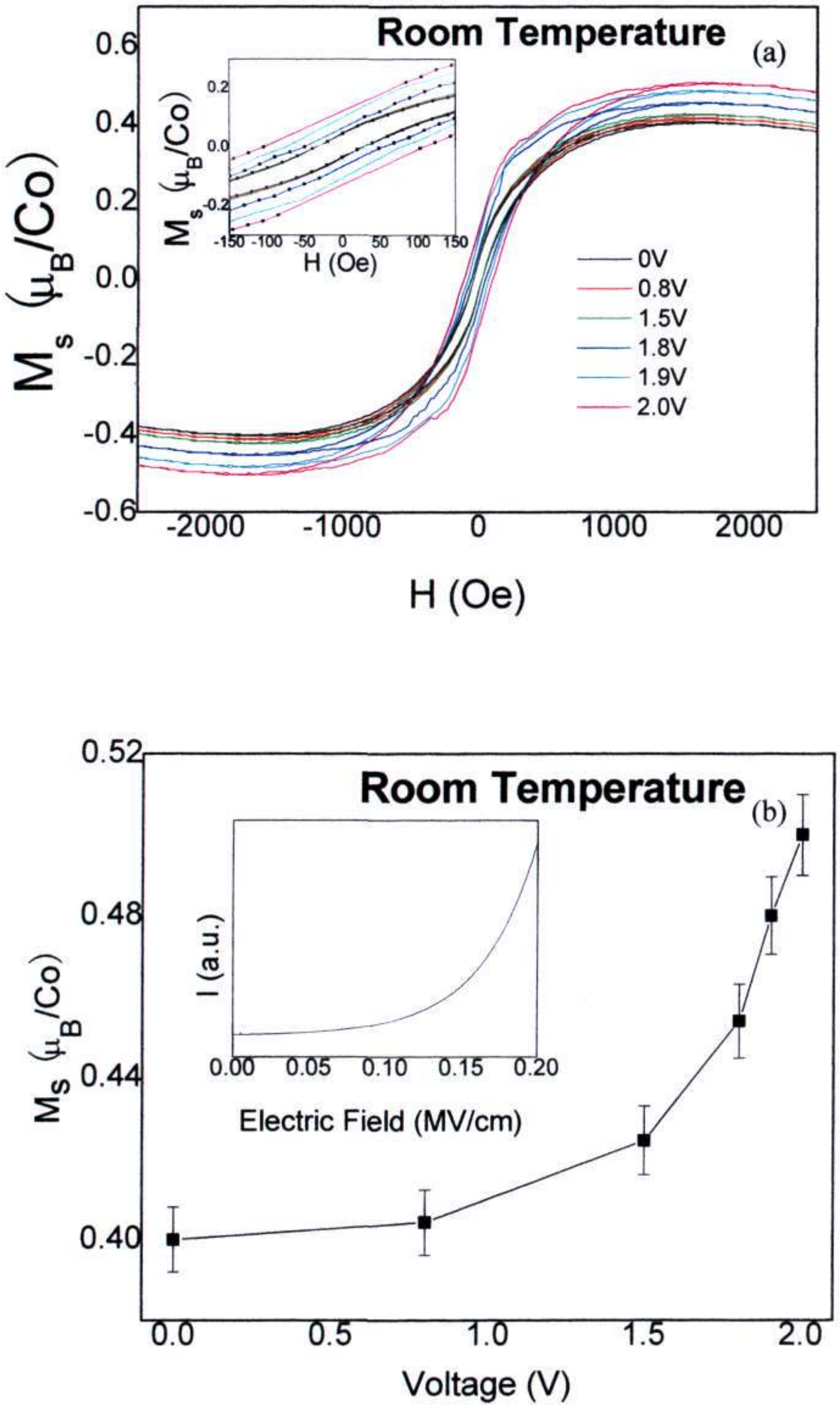

Figure 6.3 (a) Magnetization as a function of field (M-H curves) measured under room temperature by SQUID at different forward bias voltages; inset is the enlarged plot which shows the H_c clearly. (b) Corresponding saturated magnetization as a function of applied forward voltages. Inset is the break down current – electric field curve.

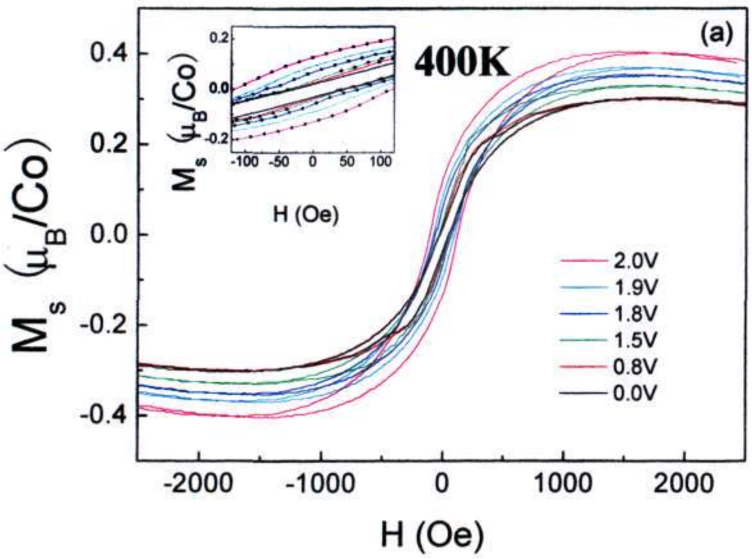

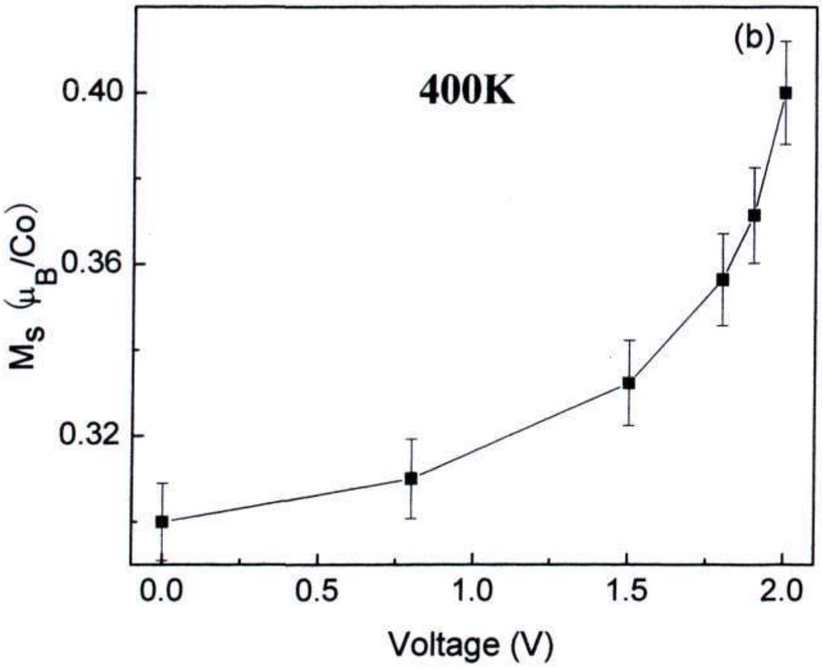

Figure 6.4 (a) Magnetization as a function of field (M-H curves) measured at 400K by SQUID at different forward bias voltages (from 0V-2V); inset is the zoom in plotting which shows the H_c clearly. (b) Corresponding saturated magnetization as a function of applied forward voltages from 0V to 2V.

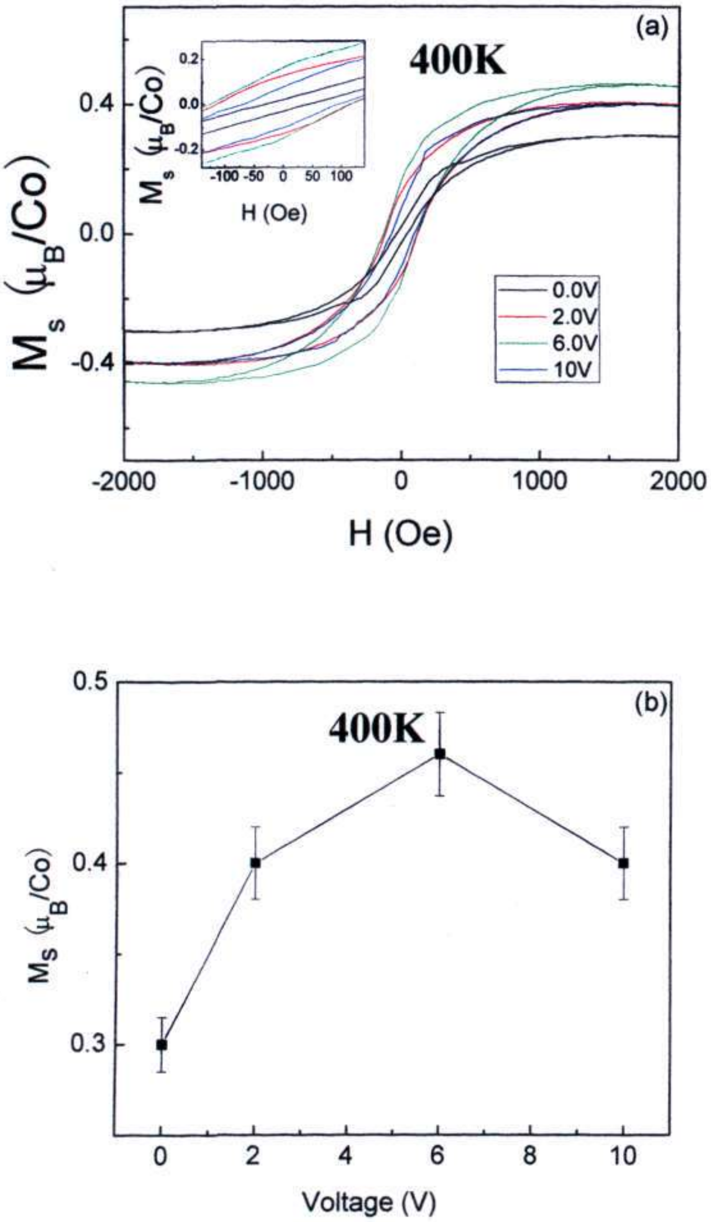

Figure 6.5 (a) Magnetization as a function of field (M-H curves) measured at 400K by SQUID at different forward bias voltages (from 2V-10V); inset is the zoom in plotting which shows the H_c clearly. (b) Corresponding saturated magnetization as a function of applied forward voltages from 2V to 10V.

Figure 6.6 shows the schematic diagram of the MIS structure under different biases. The external applied gate voltages are 2 V, 6 V and 10 V, such that the corresponding electric fields applied across the dielectric Al_2O_3 layers are 0.2 MV/cm, 0.6

MV/cm and 1 MV/cm, respectively. This high electric field allows tunneling to occur across the thinner dielectric layer [171]. The delocalized donor concentration in the magnetic semiconductor channels, which is schematically represented by empty circles in the diagram, would be controlled through this tunneling process. The amount of these delocalized donors would increase when the external electric field becomes stronger, as the free carriers in the $Zn_{0.9}Al_{0.1}O$ layer would have higher energies to tunnel into the DMS layer. The arrows schematically show the magnitude of the magnetization. When the amount of delocalized donor has increased, the magnitude of the magnetization would increase as well, which was shown experimentally in Figure 6.2.

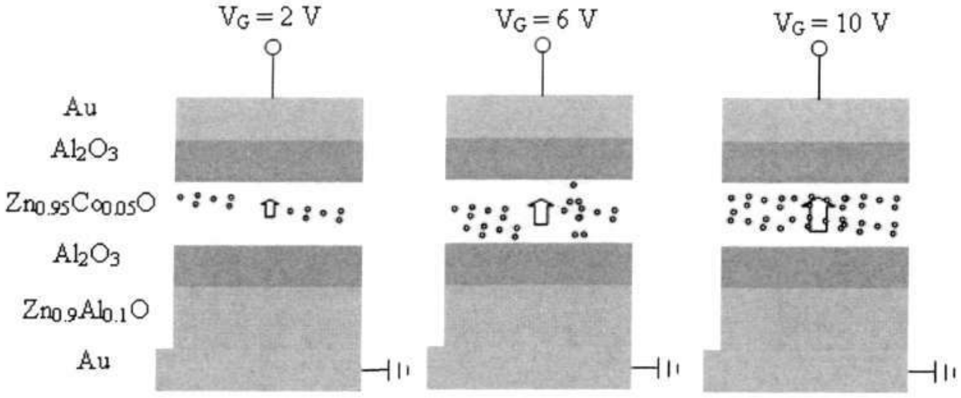

Figure 6.6 Schematic diagrams of the MIS structure under different forward biases. The circles show the donors (electrons) concentration while the arrows schematically represent the magnitude of magnetization.

Figure 6.7 is the band diagram of the MIS structure under forward bias. In the DMS thin film layer, some defects would be generated during the pulsed laser deposition process. These defects are mostly the oxygen vacancies, which would introduce additional energy states in the DMS thin films [132-134]. For the metal-insulator-semiconductor structure under forward bias condition, the majority carriers inside the N-type $Zn_{0.9}Al_{0.1}O$ layer would be attracted into the $Zn_{0.95}Co_{0.05}O$ layer, such that the number of shallow electrons would increase in this layer. At first, the electrons would be trapped in those energy states and remained localized, which is due to the influence of correlations and potential fluctuations in a narrow band. However, there is a critical donor concentration where the impurity band states become delocalized, and the conductivity will become larger [127].

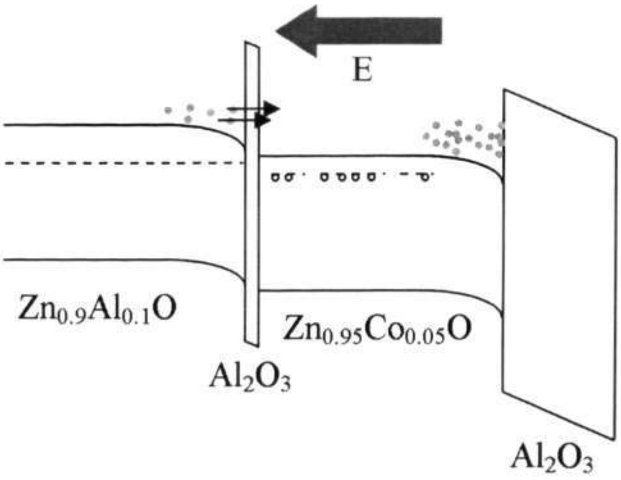

Figure 6.7 Band diagram of the metal-insulator-semiconductor under forward bias. The red arrows indicate the direction of electrons injection, empty dots are those electrons trapped at the extra energy states generated by the defects.

J. M. D. Coey *et. al.* had proposed the donor impurity band exchange mechanism in DMS materials. In the impurity band, the magnetic cations interact with hydrogenic electrons, and the donors which couple with the 3d moments of the ions within their orbits tend to form bound magnetic polarons [127]. According to this mechanism, there are two parameters for the magnetic phase diagram as discussed before, which are the polaron percolation threshold and the cation percolation threshold. In our metal-insulator-semiconductors structure, the amount of magnetic cation in the DMS layer is fixed at 0.05 for all the samples. This is less than the threshold value of 0.18 [127], such that long range order of direct coupling between neighboring magnetic cations cannot be created, which will result in restricting anti-ferromagnetism super exchange. When an external field is applied to this structure, the amount of magnetic cation will not be affected. However, the amount of carrier concentrations (donors) will increase. These donors would be trapped by the oxygen vacancies, such that inside the bound magnetic polarons, the localized electrons will interact with the magnetic cations, leading to ferromagnetic alignment. When the donor concentrations was further increased by increasing voltage, these donors would become delocalized, and the bound magnetic polarons assumption would fail. These delocalized carriers would interact with the magnetic cations as well, but this time it is not by the bound magnetic polarons model, but by the RKKY-Zener mechanism.

According to the discussion in chapter 4, the first term of the effective magnetic Hamiltonian shows the RKKY indirect interaction:

$$\sum_{ij} J_F(r_{ij}) S_i \cdot S_j \tag{6.1}$$

In this term, J_F can be expressed as:

$$J_F(r) = J_0\left[(2k_F r)\cos(2k_F r) - \sin(2k_F r)\right] \,/ (k_F r)^4 \tag{6.2}$$

Where J_0 is the fundamental ferromagnetic coupling parameter, k_F is the wave vector, and r is the separation between randomly located substitutional cobalt pairs in the ZnO lattice [1]. From this model, we can observe that at low carrier concentration, the coupling is always ferromagnetic, and in high carrier concentration, the oscillatory aspects of the RKKY interaction come into play.

When the external field is increased, the donor concentration will increase, and the possibility of interaction of these delocalized donors with the magnetic cations will increase as well. This will result in the increase of ferromagnetism in DMS. However, with further increase in the donor concentration, the carrier density may become larger than the magnetic cations concentration, and the oscillatory aspects of the RKKY interaction come into play, potentially suppressing DMS ferromagnetism. Thus, it is shown in the M-H curves at room temperature, the saturated magnetization will increase and then decrease.

At low temperature such as 5 K, the delocalized electrons would become localized, and the RKKY interaction would be suppressed. However, the bound magnetic polarons model still applies, as the electrons will be localized and form polarons, which can interact with the magnetic cations within those polarons. It is shown in the low temperature M-H curves, the saturated magnetization is almost the same at different external field, which implies that at different carriers concentration, the saturated magnetization will not be affected.

6. 4 Summary

In summary, a Metal-insulator-semiconductor structure was fabricated by the PLD deposition technique. By controlling the forward bias voltage, the amount of donor concentration inside the DMS layers could be controlled. The saturated magnetization of the DMS materials could be adjusted as well. The magnetic characterization shows that the origins of the ferromagnetism would be most likely due to the RKKY interaction and the bound magnetic polarons at room temperature. However, at low temperatures, the ferromagnetism would be mainly due to the localized donors interacting with the magnetic cations which is inside the bound magnetic polarons.

Chapter 7 DMS Nano-Structures

7.1 Introduction

In the previous chapter, external control of ferromagnetism was demonstrated in a MIS structure. In the MIS structure, DMS thin film was used as the active layer. However, in order to reduce the size of the electronic devices and save on power consumption, nanostructures such as nanodots and nanowires could be the potential candidates for nano electronic devices. However, what would be the properties of these DMS nanostructures? In this chapter, DMS nanodots and nanowires would be fabricated and their properties would be characterized.

In recent years, ordered nanodot arrays are attractive for its potential applications, such as magnetic data storage [141-144], optoelectronic devices [145], biosensors [146,147] and catalysts for the growth of aligned one-dimensional nanostructures [148-151]. On the other hand, nanowires are emerging as versatile building blocks for a diversity of nanoscale functional devices ranging from UV lasers [162], nanocantilevers [166], chemical sensors [167], light-emitting diodes [168], to acoustic wave resonators [108] and field-effect transistors [41]. Many methods have been developed for nanodot array patterning, such as focused ion beam or e-beam lithography [152,153], chemical synthesis [154,155] and template based methods [145,156-160]. However, lithographic method has a high cost and low output which constrains their potential applications. Chemical synthesis method has poor control on the nanodots ordering and dimensions. Template based methods possess the advantage of high uniformity in the as-fabricated nanodots. The nonporous in anodic aluminum oxide (AAO) membranes are hexagonally self-ordered, parallel and perpendicular to the membrane surface. The pore diameters can vary from 5 nm to 400 nm, depending on the anodization conditions. These properties make the AAO membranes ideal for the fabrication of nanodot array over a large area [158-160].

On the other hand, the integration of DMS materials into modern electronics will require very low dimensions in order to make use of the advantage offered by spins, where dimensionality and size are known to play a significant role in determining various properties of the systems. DMS-based nanostructures such as nanowires, nanodots and nanobelts are therefore attracting increasing research interest recently. A number of DMS nanowires including Mn-doped GaN [174, 175], CdS, and ZnS [175] have been synthesized and investigated. The existing synthesis approaches such as ion implantation [171] and vapor-phase transport method [172] may not offer precise control over the chemical composition and morphology of the ZnO DMS nanowires.

In this context, DMS nanodots were deposited using pulsed laser deposition method. AAO membrane was used as a mask on silicon substrate. $ZnO/Zn_{0.95}Co_{0.05}O$ core-shell nanowires were synthesized using the same technique recently developed in our group [176]. This technique provides a generic approach for the synthesis of nanowires with complex compositions. The key feature is to employ proper single-crystalline nanowires as templates, and then use the pulsed-laser-deposition process to coat the templates with desired materials to form core-shell nanowires. Here, vertical ZnO nanowires as templates were used, while $Zn_{0.95}Co_{0.05}O$ was deposited via PLD to form $ZnO/Zn_{0.95}Co_{0.05}O$ core-shell nanowires.

7.2 Experimental Details

7.2.1 $Zn_{0.95}Co_{0.05}O$ Nanodot

Figure 7.1 shows the experimental procedure for the fabrication of DMS nanodots. 1 μm-thick aluminum film was first E-beam evaporated onto a SiO_2/Si substrate. The growth rate of aluminum was carefully controlled in order to achieve a smooth surface.

Then, the aluminum film was annealed at 350ºC for 2 hrs under argon environment. The purpose of annealing was to remove the residual stresses, increase the grain size and reduce the grain boundaries areas leading to a more homogenous film for subsequent anodization. The well known two-step anodization was carried out for the fabrication of ordered AAO template. The anodization voltage was 40 V while the temperature was controlled at 3ºC and 0.3 M oxalic acid [$(COOH)_2$] was used as the electrolyte. The first step anodization was carried out for 30 minutes and then the alumina layer formed was fully removed in a mixture of phosphoric acid (6 wt %) and chromic acid (1.8 wt %) at 60ºC. This revealed a textured aluminum surface with an ordered array of concaves that had formed during the first step anodization process. These ordered concaves served as the initial sites to form a highly ordered nonporous array in the second anodization process. The second step anodization was carried out until a color change and a rapid decrease in current were observed [164]. To form a through hole AAO template, the barrier layer at the bottom of the pores has to be removed. Thus, prior to deposition of the nanodot, the sample was immersed in 5 wt % H_3PO_4 for 45 minutes. After this barrier layer removal process, a 600-nm thick through-hole AAO template was formed directly on the SiO_2 substrate.

$Zn_{0.95}Co_{0.05}O$ nanodots were grown directly on n-type (100) Si substrates by pulsed laser deposition (PLD) technique. The deposition was carried out with an oxygen partial pressure of 5×10^{-6} Torr for 25 minutes. The AAO template was then mechanically removed by commercial sticky tape.

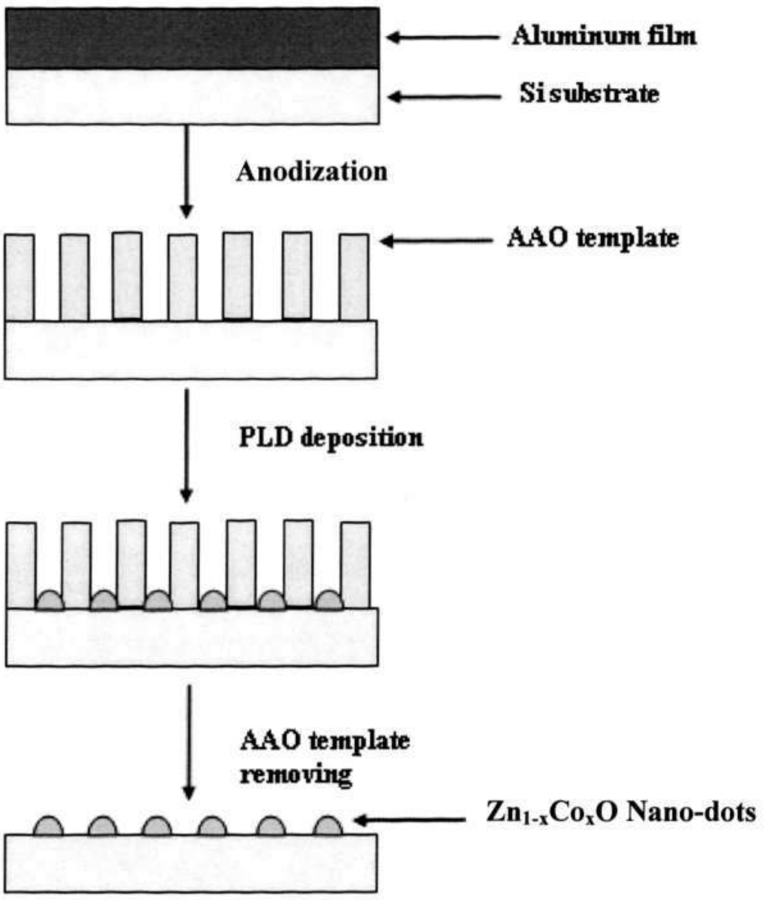

Figure 7.1 Process flow for DMS nanodots formation.

7.2.2 ZnO/ $Zn_{0.95}Co_{0.05}O$ Core-shell Nanowires

Figure 7.2 shows the process steps for formation of ZnO/ $Zn_{0.95}Co_{0.05}O$ core-shell nanowires. First, a zinc metal layer was deposited by magnetron sputtering on a bare n-type (100) silicon wafer. The thickness of the zinc metal layer was 80-100 nm. The purpose of depositing a Zn metal layer is to react it with the precursor to produce ZnO seed layer, which would serve as nucleation centers for the crystal growth of the ZnO nanowires.

The growth solution was prepared by dissolving a calculated amount of zinc nitrate hexahydrate ($Zn(NO_3)_2 \cdot 6H_2O$, 99%) in deionized water to make a solution of desired concentration (40 mM). Successively certain amount (3.6 mL) of ammonia hydroxide (28 wt % NH_3 in water, 99.99%) was added. The solution was stirred on hot plate (Stuart Heat-stir CB162) for more than 6 hour to become homogeneous.

To begin the hydrothermal growth of the ZnO nanowires, a substrate holder was required to support the substrate in the growth solution. A small glass container that was 2.5 cm in diameter and 3 cm in height was positioned in the middle of the big glass bottle to act as the holder. The substrate support had an open end facing upward such that it allowed the growth solution to fill up the empty space inside it. The Si/Zn substrate with a surface area of about 1 cm x 3 cm was suspended upside down on top of the holder, and in contact with the growth solution. The experiment set-up is shown in Figure 7.3.

The growth solution was then placed in a SHEL LAB 1330 FX Oven, and the temperature was kept at 90° C. The typical growth time was 6 h. After 6 h, the sample was removed from the solution, rinsed with deionized water, and then dried.

ZnO nanowires were then used as templates to deposit $Zn_{0.95}Co_{0.05}O$ around them by pulsed laser deposition such that ZnO/DMS core-shell structures were formed. The lattice mismatch between $Zn_{0.95}Co_{0.05}O$ and ZnO is expected to be small due to the small amount of Co atoms in the DMS layer.

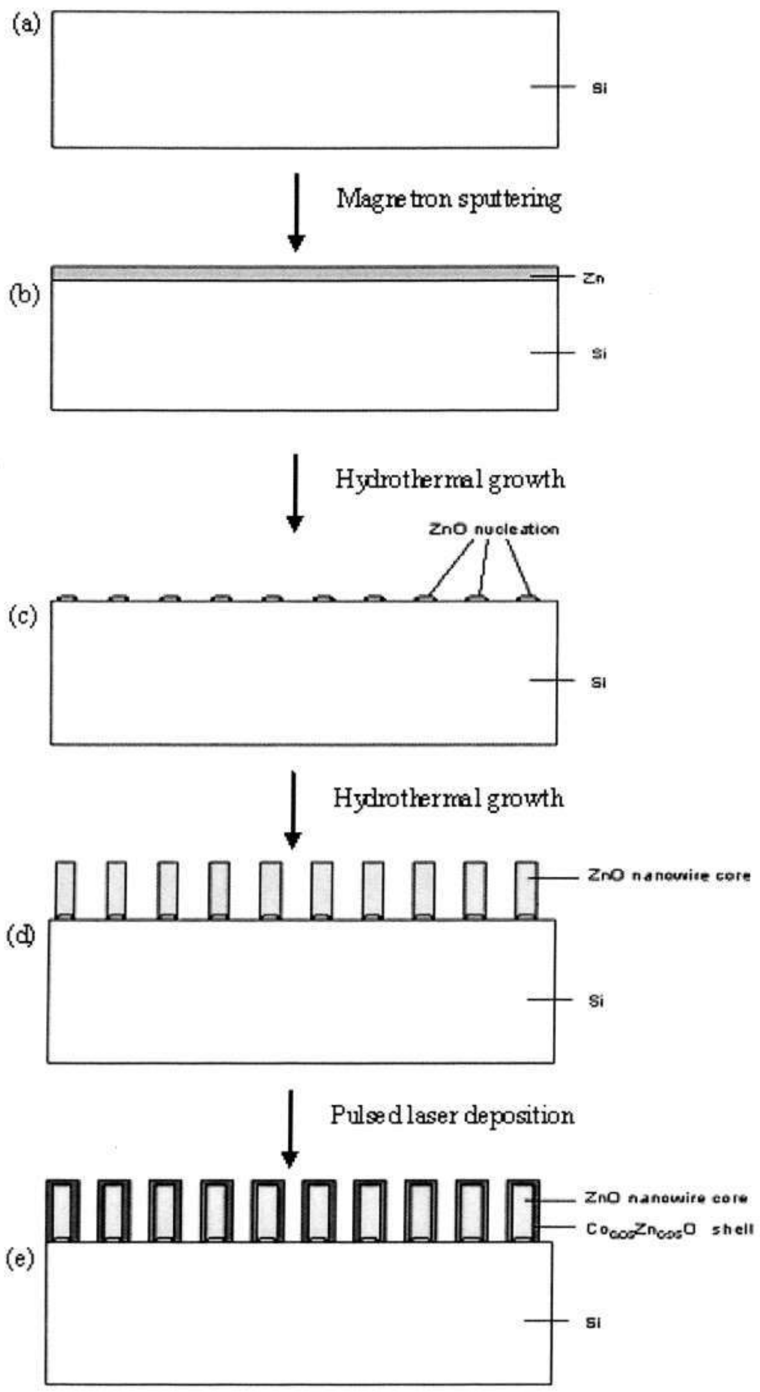

Figure 7.2 Schematic diagram of the process steps for the formation of ZnO / $Zn_{0.95}Co_{0.05}O$ core-shell nanowires. (a) Bare n-type (100) Si substrate, (b) Si substrate with magnetron sputtered Zn layers, (c) Zn reacted with precursor to produce ZnO seed layer, (d) ZnO nanowires were grown on ZnO seed layer through hydrothermal reaction, and (e) $Zn_{0.95}Co_{0.05}O$ was deposited on ZnO nanowires by pulsed laser deposition to form core-shell nanowires.

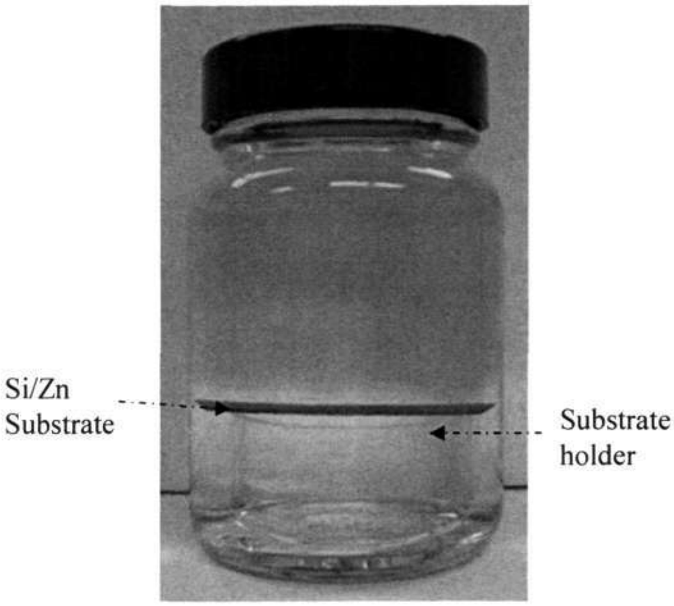

Figure 7.3 Experiment set-up for growth of ZnO nanowires.

7.3 $Zn_{0.95}Co_{0.05}O$ Nanodots

Figure 7.4 (a) shows the FESEM images of the AAO template fabricated from 1 µm-thick aluminum film after the barrier layer etching. The pore diameter is around 60 nm and the distance between the pores is about 100 nm. The cross section of the AAO template is shown in Figure 7.4 (b). From the figure, it can be observed that the nonporous are partially ordered in some region. The ordering of the pores can be improved by using pre-textured [165] method such as annealing or increasing the first step anodization time.

Figure 7.5 (a) shows the FESEM image of the nano dots deposited for 25 mins by using the AAO template. It is observed that the nano-dots were not uniformly deposited on the whole substrate surface. This is because the Al film was not fully anodized in all areas. When a nano-dot was deposited into a nonporous that was partially anodized, and the template was removed mechanically subsequently, the nano-dots would be removed together with the template. Figure 7.5 (b) is the higher magnification for the highlighted area. It shows that the nanodots has a hexagonally structure, which corresponds to the AAO template structures as shown in Figure 7.4 (a) and (b). The average diameter of the DMS nanodots is around 50 nm, which is slightly smaller than the AAO pore size. This could be due to the shadowing effect from the deposition. It is shown in figure 7.4 (b) that the aspect ratio of the AAO template can be as high as 12.

Figure 7.6 is the cross sectional TEM view of DMS nanodots. The dot is semi-spherical. However, the crystal structure is not as good as the thin film which was deposited at the same oxygen partial pressure which is shown in previous chapter. This is because the deposition temperature for those nanodots is room temperature. From the HRTEM image, the lattice distance is 0.26 nm, which corresponds to the distance between (002) inter-planes.

Figure 7.7 shows the M-H curve for the DMS nanodots measured by SQUID at room temperature. It shows room temperature ferromagnetism. It has a small Coercity H_c of 40 Oe. The magnetic moment saturated when the external field was about 1400 Oe, which is larger than that of thin films prepared at the same condition. As discussed before, the origins of this room temperature ferromagnetism property is mediated through the localized donor electrons in the impurity band, and a sufficient large number of bound magnetic polarons are required for the long range ferromagnetism order. According to the calculation for thin films, at this deposition condition, the oxygen vacancies are sufficient to form overlapped polarons. However, when the DMS is in the form of nano-dots, with an external magnetic field, magnetic cations will have ferromagnetism order at each dot. The distance between each dot is 20-30 nm, the polarons in each dot will not overlap with the neighboring dots. The saturation magnetization of nanodots (0.12 μ_B/Co) is smaller than that of thin films.

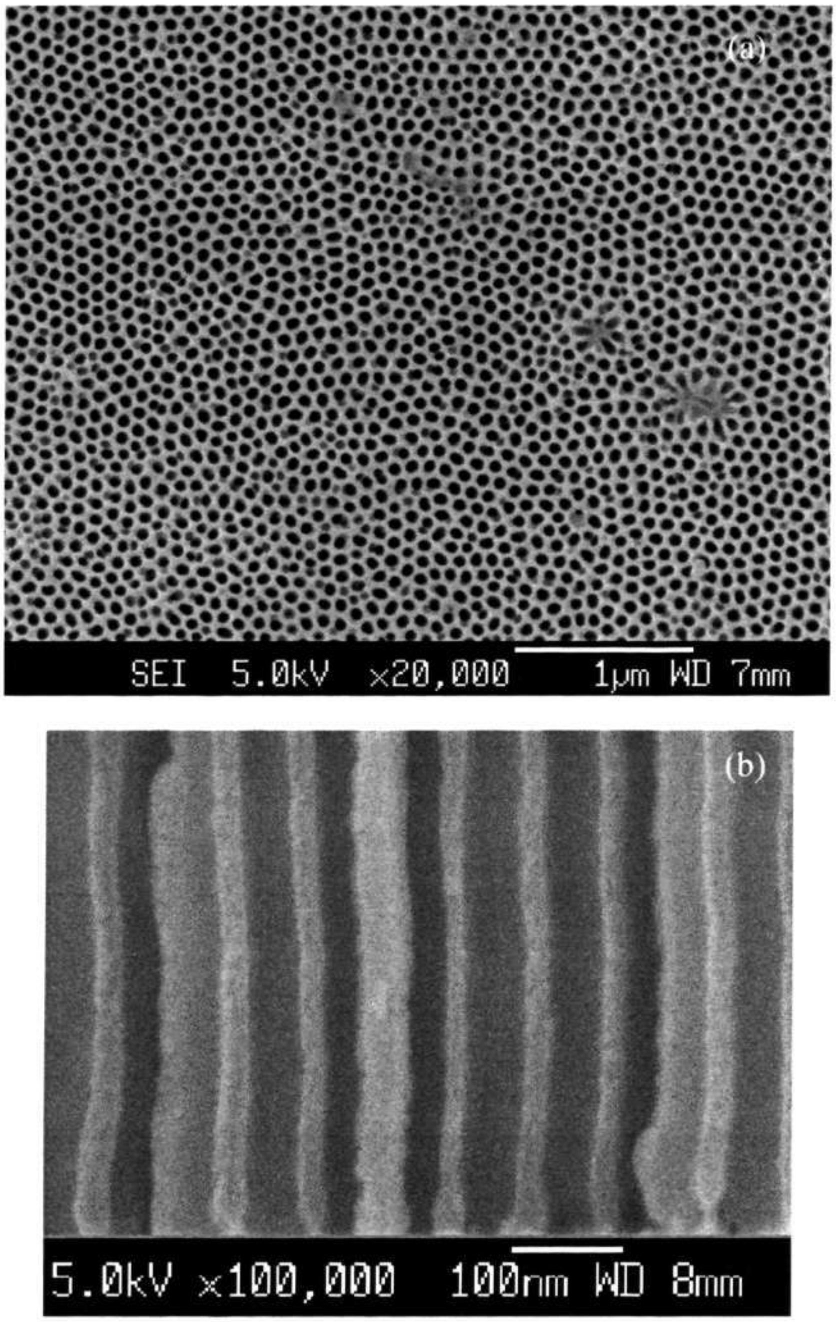

Figure 7.4 (a) Top view FESEM image of AAO template on SiO_2, and (b) is the cross section FESEM image of the AAO template.

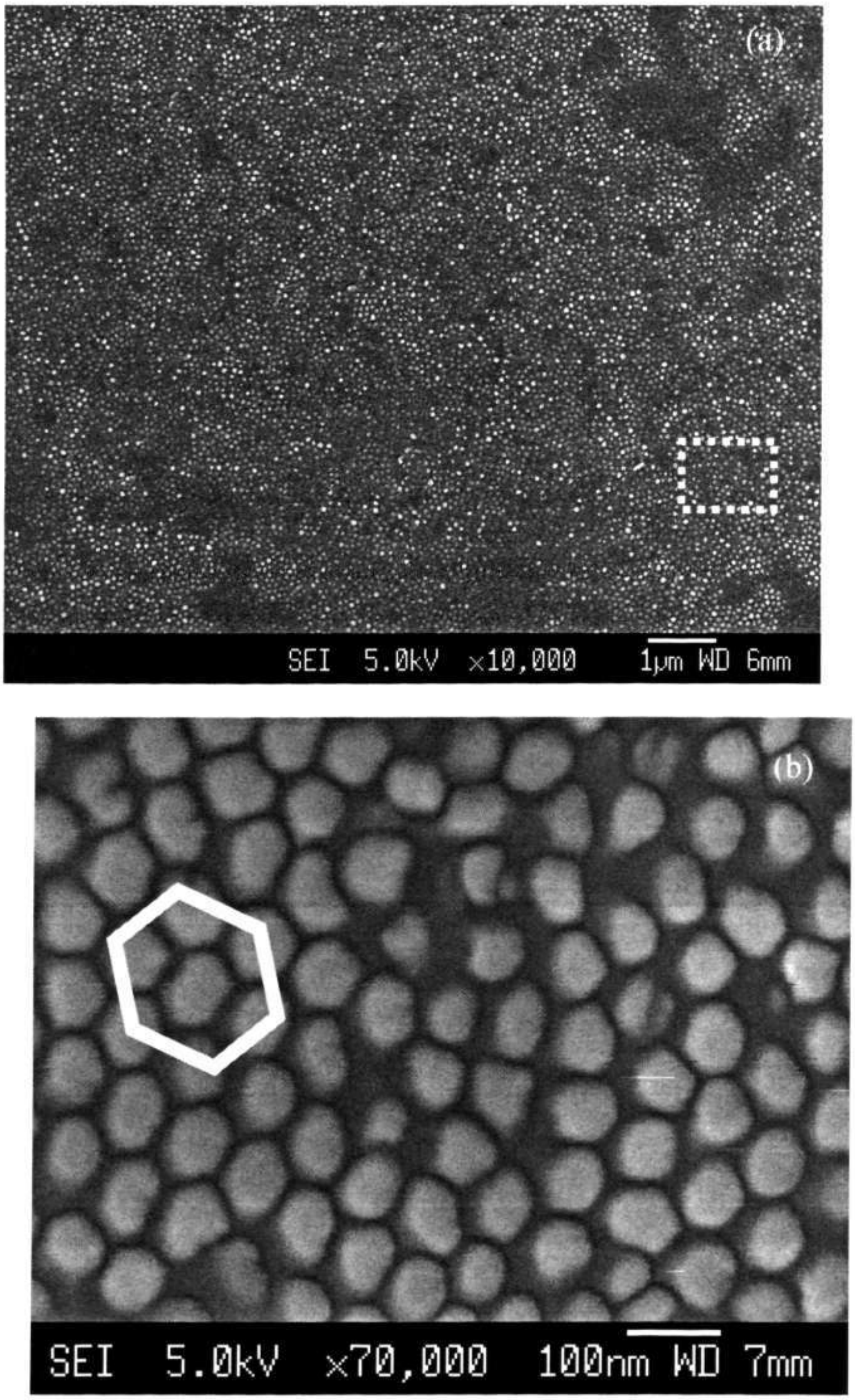

Figure 7.5 (a) Top view of FESEM image for $Zn_{0.95}Co_{0.05}O$ nano dots fabricated through AAO template by PLD technique, and (b) is a higher magnification of the highlighted area in (a).

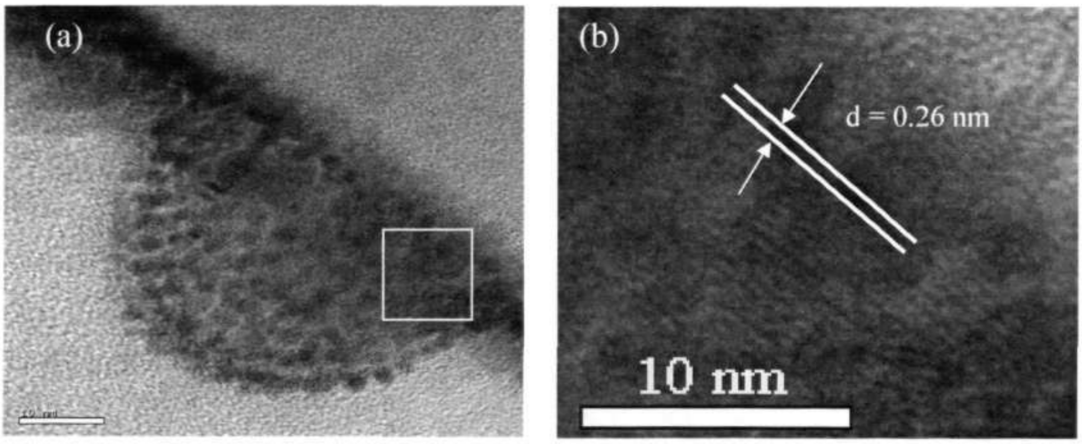

Figure 7.6 (a) Cross section TEM image for the $Zn_{0.95}Co_{0.05}O$ nano dots, and (b) is the HRTEM image for the highlighted area in (a).

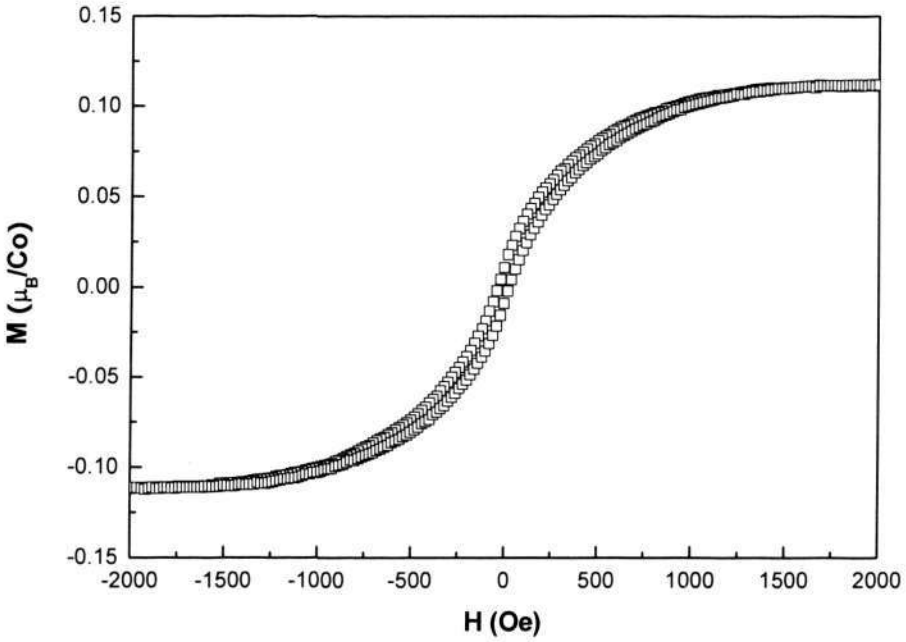

Figure 7.7 Room Temperature M-H curve for $Zn_{0.95}Co_{0.05}O$ nano dots fabricated through AAO template by PLD technique.

7.4 $ZnO/Zn_{0.95}Co_{0.05}O$ Core-shell Nanowires

The top view FESEM image of ZnO nanowires grown in 40 mM/3.6 mL solution is shown in Figure 7.8, and the cross section image is shown in Figure 7.9. Based on the top and cross section views, it was observed that the ZnO nanowires had grown vertically on the substrate. The diameter distribution of the nanowires in different areas of the sample was examined and plotted as shown in Figure 7.10. It showed that the diameter varied from 40 nm to 100 nm, and the average diameter was about 70 nm. The average length of the nanowires measured from the FESEM images was approximately 3.6 µm. A thin ZnO seed layer was also found at the bottom of ZnO nanowires as indicated in Figure 7.9. This ZnO seed layer would have served as nucleation centers for the growth of nanowires [177]. The chemical reactions are shown in the following:

$$Zn + 2OH^- \rightarrow ZnO_2^{2-} + H_2 \qquad (7.1)$$

$$ZnO_2^{2-} + H_2O \leftrightarrow ZnO_{(s)} + 2OH^- \qquad (7.2)$$

$$Zn^{2+} + 4NH_3 \leftrightarrow Zn(NH_3)_4^{2+} \qquad (7.3)$$

$$Zn(NH_3)_4^{2+} + 2OH^- \rightarrow ZnO + 4NH_3 + H_2O \qquad (7.4)$$

In the solution initially, zinc metal reacts with hydroxide ions to form zincate ions (ZnO_2^{2-}), and these zincate ions are soluble. Then, the soluble zincate ions react with water and form the solid-phase ZnO, which is shown in reactions 7.1 and 7.2. Thus, the zinc thin film deposited by sputtering was converted to ZnO during this process, and it can serve as good nucleation sites for solution-phase ZnO precursor at the elevated solution temperature. If a small amount of ammonia water was added to the zinc ion solution initially (low pH < 10), we observed the solution became turbid due to the formation of white $Zn(OH)_2$ precipitation. Increasing the amount of NH_3 (pH > 10), the turbid solution turned clean again. In this high NH_3 concentration environment, most of the zinc ions formed ($Zn(NH_3)_4^{2+}$) [37,38]. When the temperature of the solution was elevated, the $Zn(NH_3)_4^{2+}$ complex reacted with hydroxyl OH^- and produced ZnO crystals

[39,40]. Heterogeneous nucleation will take place preferentially on the ZnO seed surface, and well-aligned ZnO nanorod growth will be initiated.

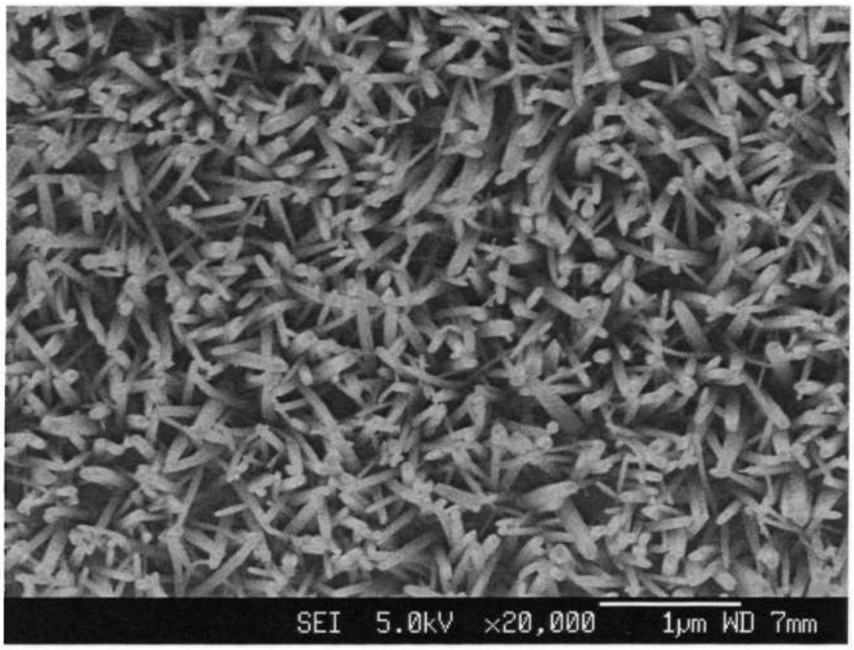

Figure 7.8 FESEM images top view of ZnO nanowires grown in 40 mM/3.6 mL solution. Scale bar: 1 μm.

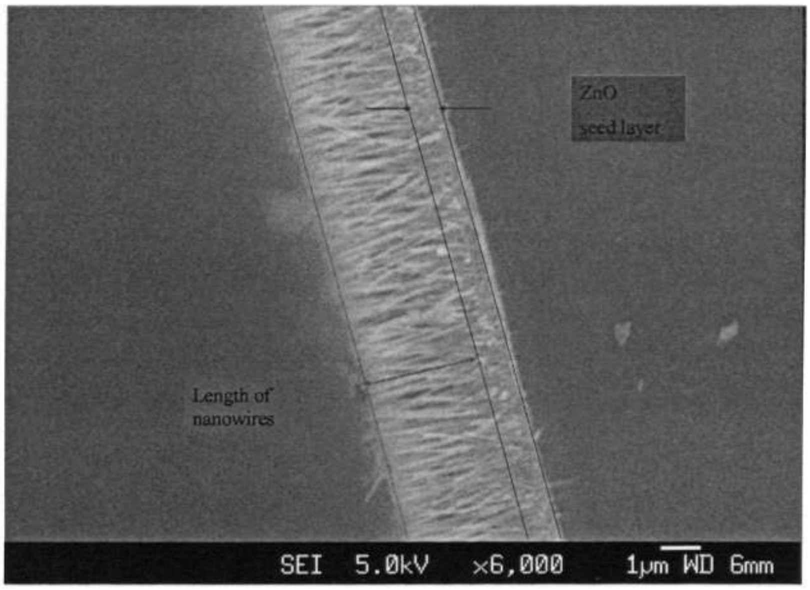

Figure 7.9 FESEM cross section view of ZnO nanowires grown in 40 mM/3.6 mL solution.

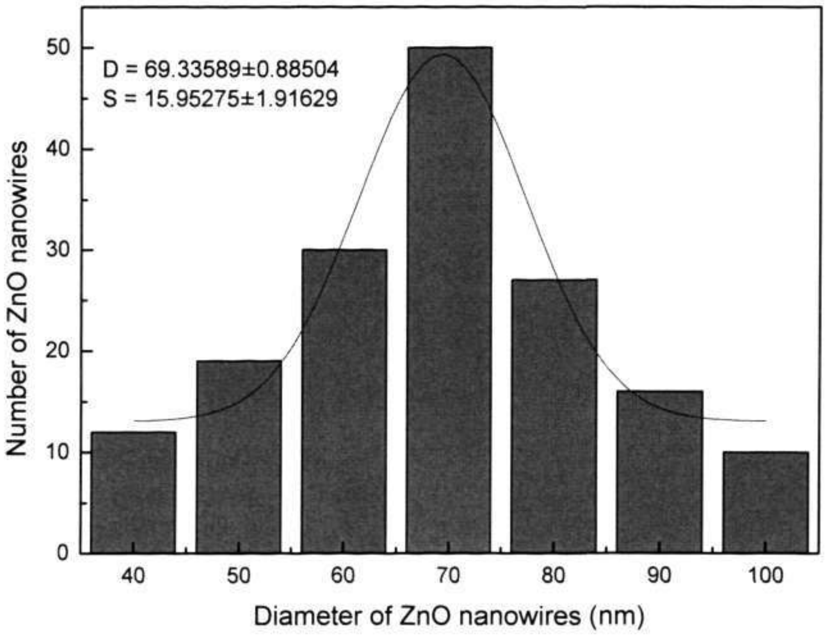

Figure 7.10 Distribution of the diameter of ZnO nanowires.

The alignment of ZnO nanowires was not all perfectly vertical and it could be seen that some nanowires tend to approach each other, deviating from the vertical growth direction. The main reason could be that the density of nanowires was not sufficiently high. If the density was high, the nanowires could be confined in the local area and would grow normal to the substrate surface. Another possible cause could be the non-uniformity of the ZnO seed layer that originated from the Zn metal layer. Prior to the nanowire growth, Zn was deposited on the Si substrate by magnetron sputtering process, whereby a small amount of impurities and defects could be incorporated. When Si/Zn substrate was immersed in the growth solution, Zn reacted to form ZnO seed layer. At the same time the impurities in the Zn film might transfer to the ZnO seed layer. As a result, the subsequent nucleation and growth of some nanowires on the ZnO seed layer would grow in a non-vertical direction.

The crystal structure of the grown ZnO nanowires was investigated using X-ray diffractometer. As shown in Figure 7.11, the XRD patterns of the ZnO nanowire arrays on the Si substrate show a strong (002) peak, a relatively weak (103) peak, and five other peaks which have insignificant intensities as compared to (002). It was found that all corresponded to ZnO peaks. The presence of multiple peaks suggests that not all ZnO nanowires were vertically aligned.

The crystal structure of the individual ZnO nanowires was investigated using TEM and high-resolution transmission electron microscopy. Figure 7.12 is a typical low-magnification TEM image of a selected ZnO nanowire. The high-magnification TEM image of the ZnO nanowires is shown in Figure 7.13. It shows that the ZnO [002] lattice fringes are perpendicular to the wire axis and have an average separation of 0.26 nm. From PDF index #050664, this distance corresponds to (002) plane. Since [002] direction is perpendicular to the (002) plane, hence the ZnO nanowire grew along the [002] direction.

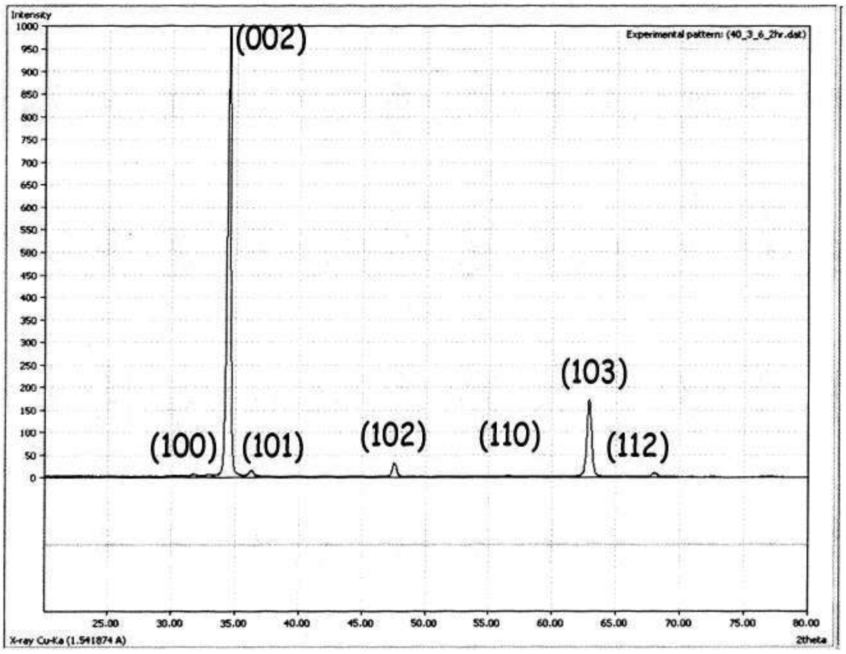

Figure 7.11 XRD patterns of ZnO nanowires.

Figure 7.14 is the corresponding selected area electron diffraction (SAED) pattern of the selected ZnO nanowire. The discrete points formed a regular pattern, indicating that the ZnO nanowires formed were single crystalline with wurtzite structure. In order to index the individual planes, a unit cell was selected. In this cell, three distances representing interplanar distances *d* as shown in the figure were measured, compared with the scale, and calculated. The interplanar distances *d* are tabulated and presented in the first column in Table 7.1, together with nominated values from PDF #050664 $d_{nominated}$ in the second column. Two sets of values are very close to each other thus the planes of ZnO nanowires could be indexed by using PDF #050664. The identified planes are (110) and (300).

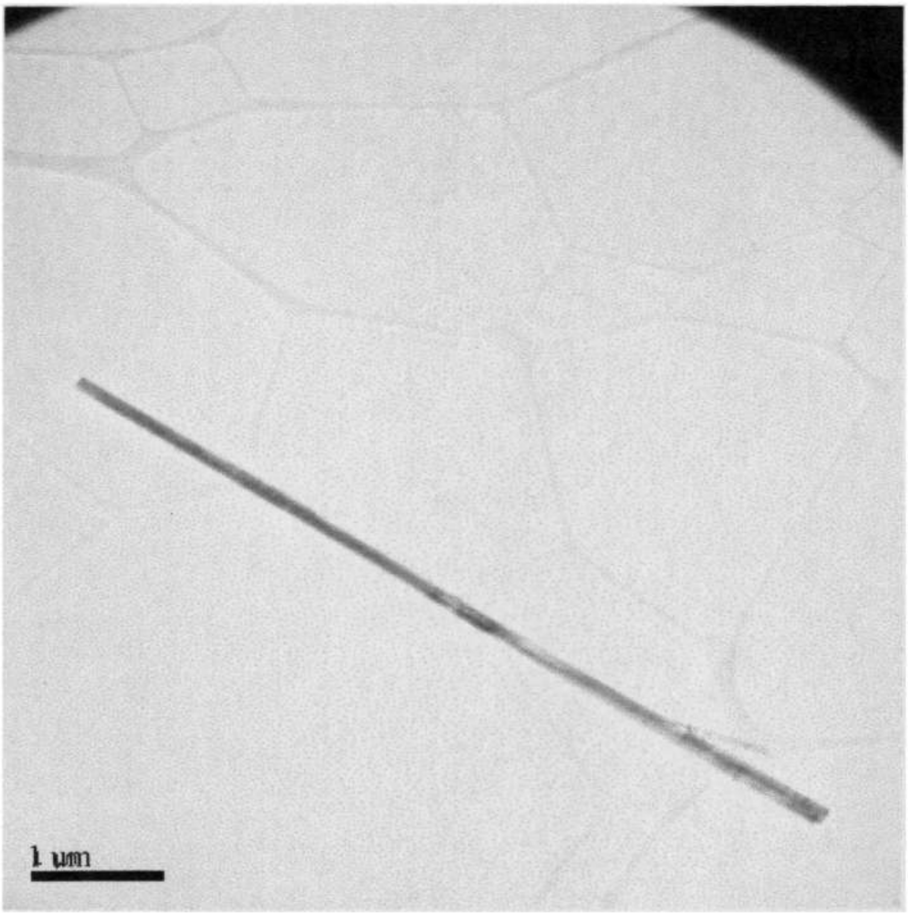

Figure 7.12 A low-magnification TEM image of a chosen ZnO nanowire.

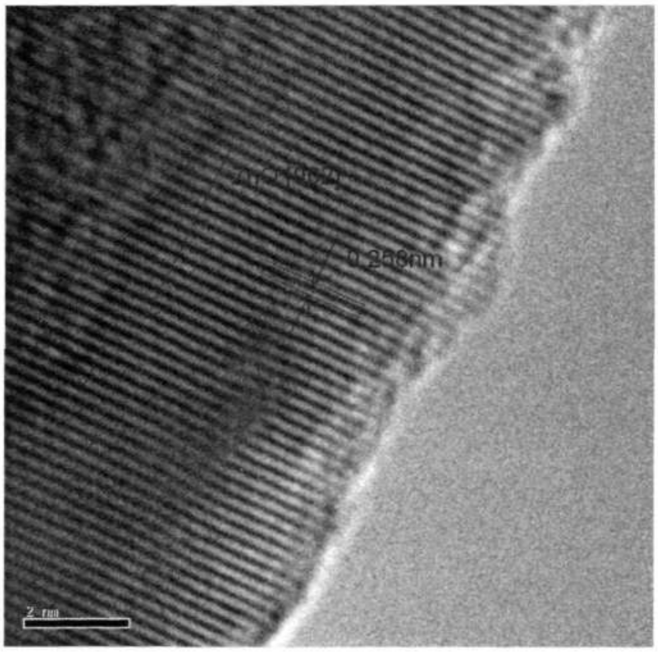

Figure 7.13 A high-magnification TEM image of a chosen ZnO nanowire.

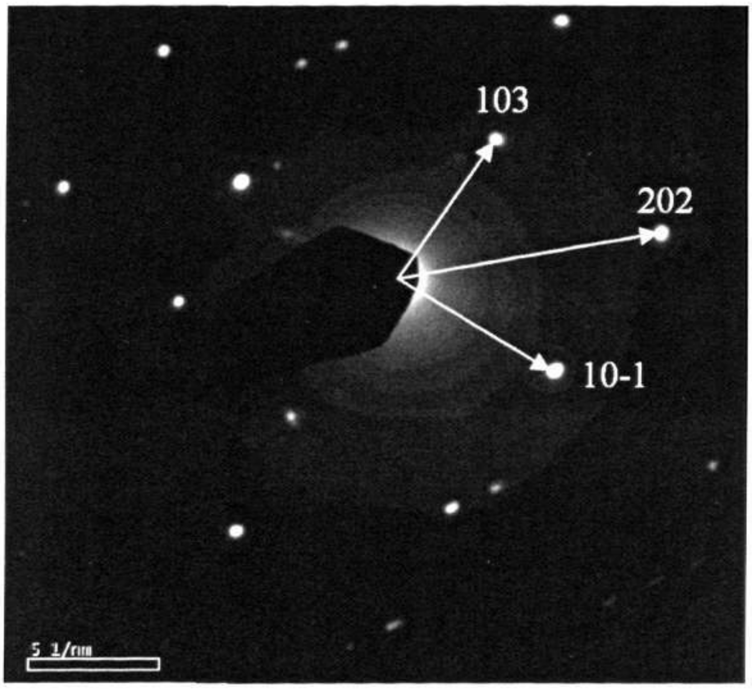

Figure 7.14 Corresponding selected area electron diffraction pattern (SAED) of a chosen ZnO nanowire.

Table 7.1 Interplanar distances of ZnO nanowire and index of planes

d(nm)	$d_{nominated}$ (nm)	hkl
0.147712	0.1464	103
0.123801	0.1235	202

The third plane index was obtained by subtracting (103) from (202), therefore giving (10-1). The zone axis could be calculated from the cross product of vectors (103) and (10-1). Since (10-1) x (103) = [0-40] = -4[010], the zone axis was [010]. The individual nanowire had a single crystalline growth along [001] direction, which was further confirmed by the (002) preferential orientation of ZnO nanowires.

The X-ray diffraction pattern of the core-shell nanowires is shown in Figure 7.15. It is evident that the positions of peaks in the XRD pattern of ZnO/DMS core-shell nanowires exactly matched with those of the ZnO nanowires previously presented in Figure 7.11, indicating that all the peaks were related to ZnO and there was no second phase present. Furthermore, the intensities of peaks were almost the same in these two patterns. Since Co (one of strong peaks appeared at $2\theta = 75.5^{\circ}$), CoO and Co_3O_4 were not detected by the XRD, it is possible that Co^{2+} ions had substituted Zn^{2+} ions in the wurtzite structure.

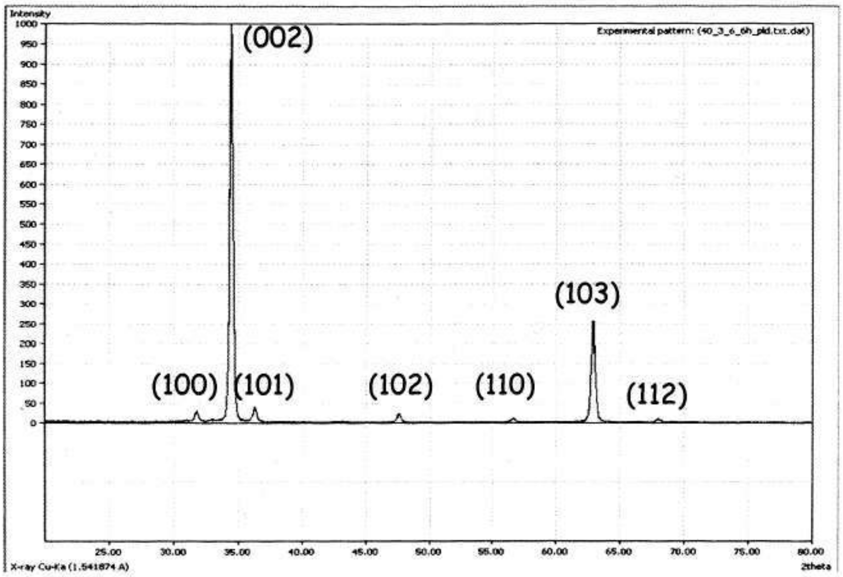

Figure 7.15 XRD patterns of core-shell nanowires.

In addition, the structure of a selected core-shell nanowire could be observed in low-magnification TEM image as shown in Figure 7.16. The structure showed two distinctive layers, each of them had sharp boundaries. The middle dark color region is the ZnO nanowire core while the grey color area on its surface is Co-doped ZnO shell. This image showed that the Co-doped ZnO shell was successfully deposited on the ZnO nanowire core with uniform thickness. From this figure, the diameter of the core-shell nanowires was measured to be about 100 nm. The diameter of the core was approximately 60 nm, with the thickness of the Co-doped ZnO shell around 20 nm.

Figure 7.17 (a) shows the HRTEM image of the edge of a core-shell nanowire. It is observed that the edge is polycrystalline. In the previous section, according to the HRTEM and SAED data, the ZnO nanowire is single crystal. By comparing these two HRTEM images, it shows that the DMS shell was coated onto the ZnO nanowires. The polycrystalline nature of DMS materials could be due to the low deposition temperature, as the samples were prepared at room temperature. From chapter 5, it was shown that when the ZnO and DMS samples were prepared at room temperature by PLD method, it could lead to polycrystalline structure instead of single crystal, which is shown in the XRD data. Figure 7.17 (b) shows the diffraction pattern for the core-shell nanowire, it shows that the nanowire is polycrystalline.

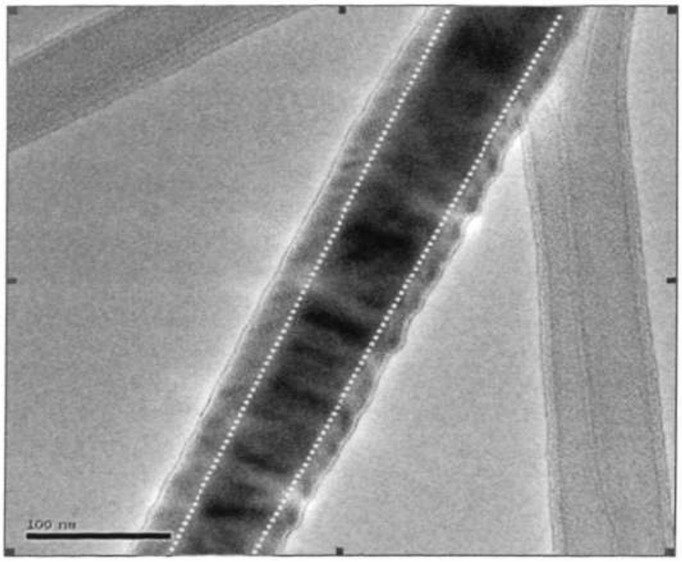

Figure 7.16 A low-magnification TEM images of a chosen core-shell nanowire.

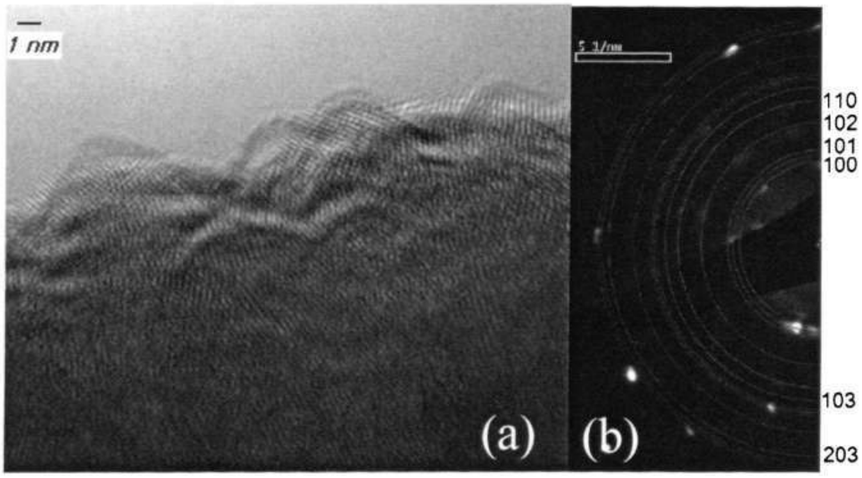

Figure 7.17 (a) HRTEM of the edge of the core-shell nanowire, scale bar: 1 nm, (b) diffraction pattern of (a).

A SQUID magnetometer was used to precisely characterize the magnetic properties of the ZnO/$Zn_{0.95}Co_{0.05}O$ core-shell nanowires. Figure 7.18 and 7.19 are measured results of the magnetization of core-shell nanowires as a function of an external applied field with the temperature kept at 5 K and 300 K respectively. Clear hysteresis loops were observed in both graphs, which strongly indicate that the core-shell nanowires were ferromagnetic at room temperature. Coercive fields of 260 Oe at 5 K and 138 Oe at 300 K were achieved.

To understand more about its magnetic behavior, temperature dependence of the zero-field-cooled (ZFC) and field-cooled (FC) magnetization of ZnO/ $Zn_{0.95}Co_{0.05}O$ core-shell nanowires in H=10 kOe was carried out as shown in Figure 7.20. Zero-field cooling was achieved by cooling the sample from 300 K to 5 K in the absence of an external field and then heating up from 5 K to 300 K in the presence of an external field of 10 kOe, and measurements of magnetization were taken during heating. The only difference between FC and ZFC was that in field-cooling, an external field was applied throughout the cooling and heating processes. From the ZFC and FC curves, it shows that from the low temperature to room temperature, the DMS core-shell nanowires show ferromagnetic properties, and no super paramagnetic or spin glass states was observed. By combining this ZFC-FC data with the M-H curves at different temperatures, it can be concluded that the nanowires were ferromagnetic. The origins of the ferromagnetic properties would be due to the oxygen vacancies generated during the sample preparation, as these samples were fabricated using the same method as previous thin film sample preparation except the substrate. Considering the amount of those wires measured, the saturation magnetization of core-shell nanowires was 0.1 (±0.05) μ_B/Co. The large errors are due to the amount of cobalt amount estimated. This saturation magnetization was smaller than that of the thin films. The reason could be due to less overlap of the bound magnetic polarons compared to the thin films.

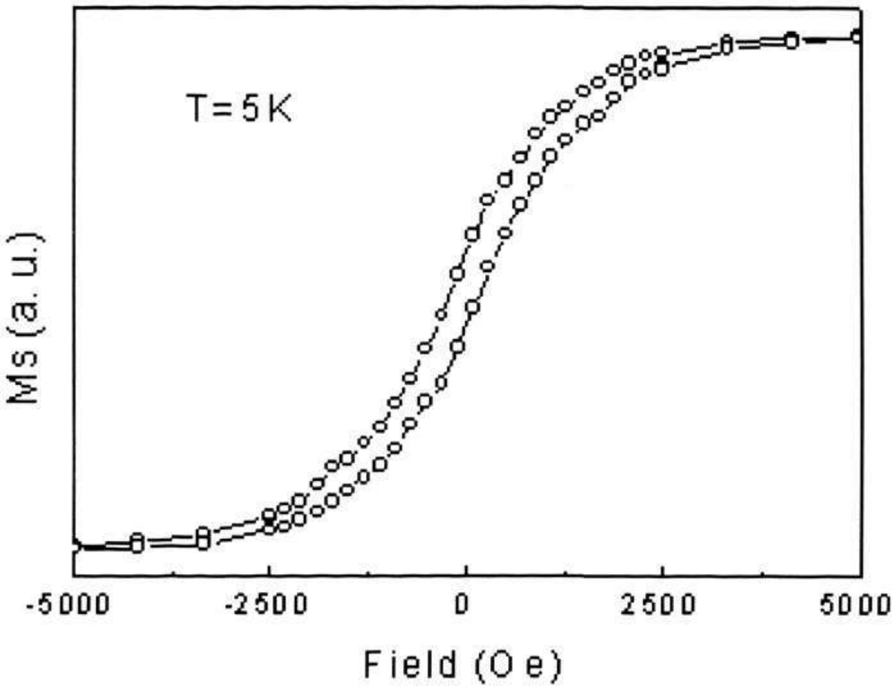

Figure 7.18 Magnetization as a function of an applied field for ZnO/ $Zn_{0.95}Co_{0.05}O$ at 5 K.

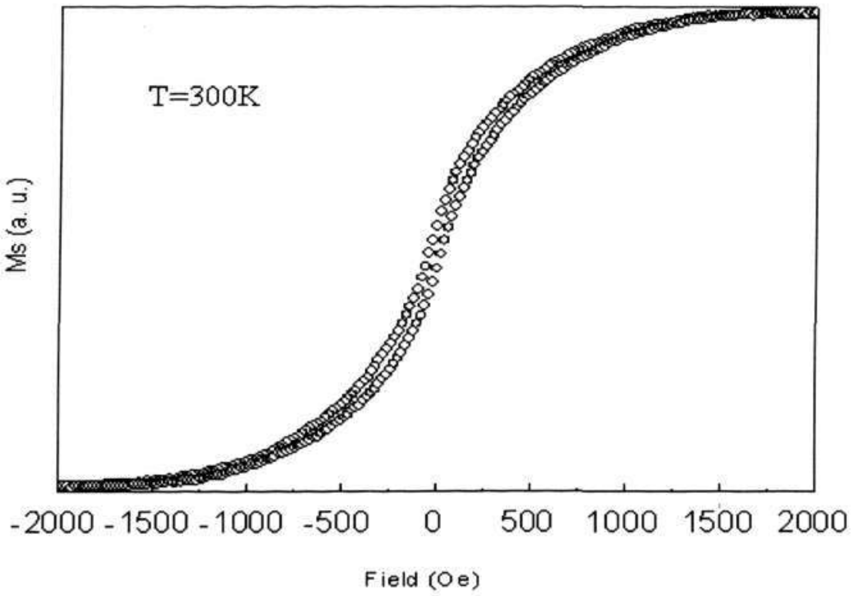

Figure 7.19 Magnetization as a function of an applied field for ZnO/ $Zn_{0.95}Co_{0.05}O$ at 300 K.

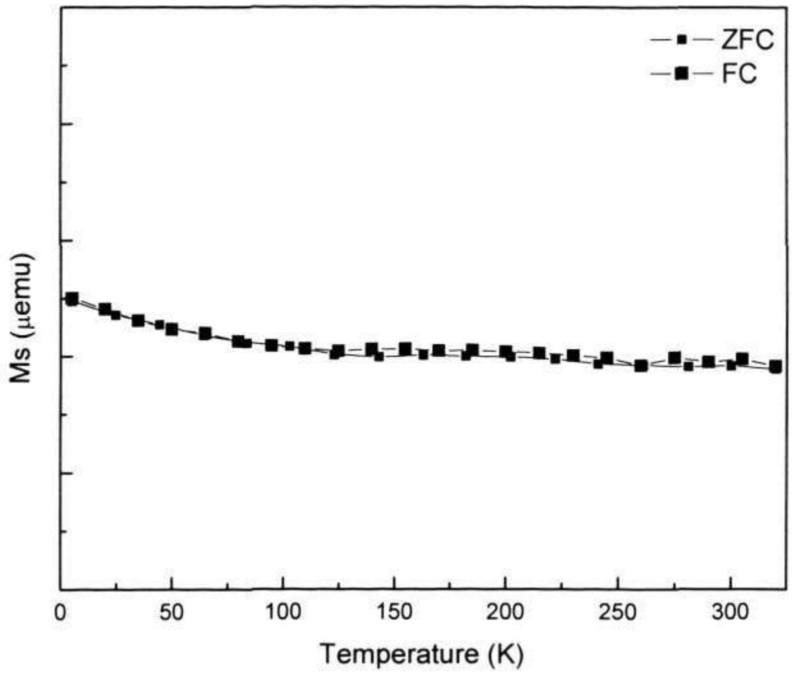

Figure 7.20 Field-cooled (FC) and zero field-cooled (ZFC) magnetization of ZnO/ $Zn_{0.95}Co_{0.05}O$ core-shell nanowires at 10 kOe.

7.5 Summary

In summary, room temperature ferromagnetism $Zn_{0.95}Co_{0.05}O$ nano dots have been successfully deposited on Si (001) substrate by Pulsed Laser Deposition technique through AAO template. A saturation magnetization of 0.12 μ_B/Co was achieved at room temperature. The origin of these room temperature ferromagnetism properties are most likely due to the oxygen vacancies introduced during the sample preparation, which is the same as in the thin films. However, the saturation magnetization is smaller than that of the thin films, as it will have less long range ordering due to the non overlap of bound magnetic polarons in the nanodots.

Vertically aligned ZnO nanowires were successfully grown on Si/Zn substrate by sol-gel method. The distribution of diameters showed a range between 40 nm to 100 nm, with an average value of 70 nm. The length of nanowires was highly uniform and estimated to be 3.6 μm. From the XRD scans, only ZnO related peaks were detected. The dominant ZnO (002) peaks were also observed, indicative of [002] preferential crystal growth direction, which in turn proved the vertical alignment of nanowires. TEM results further demonstrated (002) preferential orientation of ZnO nanowires.

Pulsed laser deposition technique was then employed to deposit dilute magnetic semiconductor Co-doped ZnO on the ZnO nanowires to form ZnO/DMS core-shell nanowires. XRD was applied again to study the crystal structure of the core-shell nanowires. The positions and intensities of core-shell nanowires matched those of ZnO nanowires very well despite small deviations in intensity. Metallic Co and cobalt related oxides peaks were not detected. This revealed that Co^{2+} ions had probably substituted Zn^{2+} ions in the wurtzite structure. TEM image clearly showed the formation of core-shell nanowires. In addition, characterized by a SQUID magnetometer, ZnO/DMS core-shell nanowires displayed hysteresis loops at 5 K and 300 K. the FC and ZFC curves almost overlapped each other. Both results led to the conclusion of ferromagnetism, and exclusion of other magnetic systems such as paramagnetism, superparamagnetic or spin glass.

Chapter 8 Conclusions and Recommendations

8.1 Conclusions

In this project, the origins of ferromagnetism inside cobalt doped ZnO DMS materials were investigated. Room temperature ferromagnetic DMS thin films and nano-structures were deposited and studied for their further application on spintronics devices. Characterizations of the DMS thin films and nano-structures were carried out by X-ray Diffraction (XRD), Field-Emission Scanning Electron Microscope (FESEM) and Transmission Electron Microscopy (TEM), and X-ray photoelectron spectroscopy (XPS). The magnetic properties measurements were carried out by using Superconductor Quantum Interface Detector (SQUID).

To overcome the limitations and challenges in the realization of spintronics devices, Co-doped ZnO DMS is one of the promising materials that may help to solve the limitation. However, the origin of its high temperature ferromagnetic properties is still under investigation, Therefore, the general goals of this project consist of the following 3 parts: (1) To fabricate and characterize cobalt doped ZnO DMS thin films on silicon substrate, (2) To investigate the role of metallic cobalt to the ferromagnetic properties of DMS materials, and the origins of ferromagnetism inside cobalt doped ZnO DMS materials, and (3) to fabricate and characterize cobalt doped ZnO DMS nano-structures for nano device application.

8.1.1 DMS Thin Films

Pulsed laser ablation has been used to successfully fabricate cobalt doped ZnO thin films in vacuum conditions at 450^{o}C. XRD and TEM analysis confirmed that the as synthesized products were hexagonal structure and single phase, with no second phase detected. XPS confirmed that the state of the cobalt is in 2+ states. TEM results also showed that the as deposited thin films have (002) preferential orientations, which is coherent with the XRD results. SQUID results indicated that the ZnO with cobalt doped thin films were ferromagnetic at room temperature. It has a saturated magnetization of 0.86 μB/Co, which is less than that of metallic cobalt (1.7 μB/Co).

8.1.2 Contribution of Metallic Cobalt Nanoclusters to Ferromagnetism

In order to rule out the contributions of metallic cobalt to the room temperature ferromagnetism of the Co-doped ZnO thin films, a Co nanodots embedded ZnO thin film was designed and successfully realized by pulsed laser ablation technique. XRD results showed that the cobalt nanoclusters embedded in ZnO have hexagonal *metallic* cobalt peak located at 43.98°. These results also showed that the ZnO matrix is polycrystalline, and more defects were generated during the sample preparation. TEM images show that the metallic cobalt nanocluster has an overall density of 1×10^{12} cm^{-2}, with an average diameter of 4.5 nm. The diffraction patterns showed that the ZnO matrix and Co metallic nanoclusters were polycrystalline. SQUID results showed that both cobalt doped ZnO and metallic cobalt nanoclusters embedded ZnO thin films were ferromagnetic. However, the cobalt doped ZnO thin films have smaller saturated magnetizations. These SQUID results also showed that the cobalt doped ZnO thin films require a much smaller external field to reach saturation conditions. All these indicated that the ferromagnetism properties of dilute magnetic thin films prepared at 5×10^{-7} Torr was not dominated by the metallic cobalt nanoclusters. SQUID results for the two systems prepared at 5×10^{-4} Torr gave the direct evidence of this conclusion. It indicated that for the cobalt doped ZnO thin film, it would be in the ferromagnetic state. On the other hand, metallic cobalt embedded ZnO system gave paramagnetic states. The XRD results show that the metallic cobalt nanoclusters embedded in ZnO matrix was in the form of CoO, instead of metallic cobalt.

8.1.3 Contribution of Oxygen Partial Pressure to Ferromagnetism

By changing the oxygen partial pressure during the sample preparation, the amount of oxygen vacancies density was adjusted. PL results showed that at lower oxygen partial pressure, the amount of oxygen vacancies was larger, and after annealing at high temperature in oxygen rich condition, these oxygen vacancies would be reduced significantly. XRD results showed that the thin films prepared at different oxygen partial pressure have (002) orientations. It also indicated that the thin films were single phase. TEM results also showed that the DMS thin films are single phase, with (002) preferred orientation, which is in coherence with the XRD results. SQUID results showed that the saturated magnetization increased when the sample was prepared at high oxygen partial pressure as compared with samples prepared at lower oxygen partial pressure. This is because under a lower oxygen partial pressure would give a larger amount of the oxygen vacancies in the samples. According to the BMP model, a larger amount of magnetic polarons due to the larger amount of oxygen vacancies would result in an increase of ferromagnetic properties.

8.1.4 Contribution of Substrate Temperature to Ferromagnetism

By changing the substrate deposition temperature, the delocalized carrier concentrations and mean free path could be adjusted. XRD results showed that the thin films prepared at different temperature had (002) preferred orientations, and it was single phase. It also indicated that at higher deposition temperature, the crystal defects would be reduced, and a larger mean free path for the free carriers generated due to the defects. TEM results again supported that the thin films had (002) preferred orientations and were single phase. SQUID results showed that thin films prepared at a substrate temperature of 450°C would give the highest saturated magnetization. This shows that both delocalize carriers concentrations and the mean free path of the delocalized carriers would impact the ferromagnetic properties of the DMS materials.

8.1.5 External Control of Ferromagnetism

A metal insulator semiconductor structure was successfully fabricated by pulsed laser ablation technique. TEM results showed the cross section image of $Au/Al_2O_3/Zn_{0.95}Co_{0.05}O/Al_2O_3/Zn_{0.9}Al_{0.1}O/Au/Ti$ structure. Under forward bias, electrons would be trapped in the DMS layer, such that the carrier concentration could be adjusted by the external electric field. Room temperature SQUID results showed that the DMS layers are ferromagnetic states. It also indicated that when the external electric field was increased, the saturated magnetization would increase as well. This increase is due to the delocalized carried mediated RKKY interaction, and localized carriers interacted with the magnetic cations within the magnetic polarons. Low temperature SQUID results showed that the DMS layers are ferromagnetic states as well. It also indicated that the saturated magnetization would not increase when the external field was increased. This remaining ferromagnetic property could not be explained by the delocalized carriers, but by the BMP model. Thus, both BMP and RKKY interactions contribute to the ferromagnetic properties of the DMS materials.

8.1.6 Co-doped ZnO Nanodots and Nanowires

Using AAO as a template, $Zn_{0.95}Co_{0.05}O$ nanodots were fabricated. FESEM results showed that these dots have uniform diameter at around 50 nm. TEM results further showed that the sizes are 50 nm in diameter, and with (002) preferred orientations. SQUID measurements showed that the dots are ferromagnetic at room temperature, but the saturated magnetization is smaller than that of thin films prepared at the same conditions. The interactions between delocalized electrons and magnetic cations would be suspended due to the physical separation. The overlap of bound magnetic polarons would be reduced as well due to this separation. ZnO/$Zn_{0.95}Co_{0.05}O$ core shell nanowires was fabricated by using ZnO nanowires as templates. TEM results showed that the DMS shell is 20 nm. SQUID measurements showed that these nanowires were ferromagnetic at room temperature. ZFC-FC measurement further confirmed that there were no spin glass or super paramagnetic states for the core shell nanowires.

8.2 Recommendations

Based on the results achieved in this project, some recommendations for future research are listed below:

1. Origins of Ferromagnetism in DMS thin film.

Although the BMP model and RKKY mechanism were investigated in our experiments, there are still some other mechanisms that could co-exist in Co-doped ZnO materials. However, it would be not easy to prove them experimentally. Some first principle study would be required in the future. One concept that needs to be highlighted is the role of oxygen vacancies. In our discussion, these oxygen vacancies play a role in the BMP model and RKKY mechanism. Will these oxygen vacancies contribute to ferromagnetism independently? How would this factor affect the ferromagnetism in Co-doped ZnO thin films?

Pure ZnO thin films without cobalt doping can be fabricated at different oxygen partial pressure by PLD deposition method. The "charger transfer ferromagnetism" would be studied experimentally. This mechanism is purely the itinerant electron ferromagnetism tied to a local density of states associated with the defects.

2. Application of DMS materials

As seen in chapter 7, the ZnO/DMS core shell nanowires were formed by PLD method. These nanowires could be used to form spin LED. One of the proposed Spin LED schematic is shown in Figure 8.1 below:

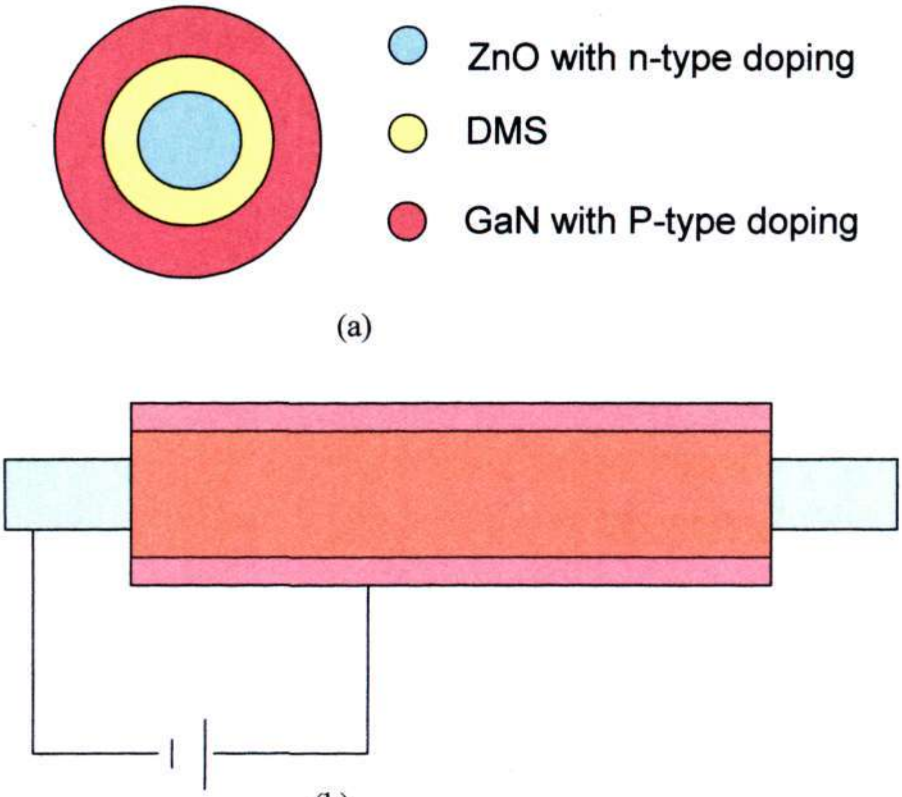

(a)

(b)

Figure 8.1 (a) top view of circular spin LED and (b) cross sectional view of spin LED.

In this spin LED, it will form n-type ZnO/DMS/p-type GaN trilayers. If external an electric field is applied, electrons will be injected from *n*-type ZnO and aligned through the DMS shell. Polarized electrons will recombine with the holes in *p*-type GaN, which results in polarized light.

Reference

[1] I. Zutic, J. Fabian, and S.D. Sarma, Rev. Mod. Phys. 76, pp. 323-410, 2004.

[2] J. Inoue, and H. Ohno, Science, Vol. 309, pp. 2004-2005, 2005

[3] J. Banhart, H. Ebert and A. Vernes, Phys. Rev. B, Vol. 56, pp. 10165-10171, 1997.

[4] M. Peter, Levy and Z. Shufeng, Phys. Rev. Lett. Vol. 65, pp. 1643-1646, 1990.

[5] A. barthelemy and A. Fert, Phys. Rev. B, vol. 43, pp. 13124-13129, 1991.

[6] G. A. Prinz, Science vol. 282, pp. 1660-1663, 1998.

[7] J. de Boeck, and G.Borghs, Physics World vol.12, No.4, pp. 27-32, 1999.

[8] C. Jacoboni and l. Reggiani, Rev. Mod. Phys. Vol. 55, pp. 645-705, 1983.

[9] M. Johnson and R. H. Silsbee, Phys. Rev. lett. Vol. 55, pp. 1790-1793, 1985.

[10] M. Johnson, Phys. Rev. Lett. Vol.70, pp. 2142-2145, 1993.

[11] M. Johnson, *Appl. Phys. Lett.* Vol. 65, pp. 1460-1462, 1994.

[12] A. Fert and S-F. Lee, Phys. Rev. B Vol. 53, pp.6554-6565, 1996.

[13] M. E. Flatte and J. M. Byers, Phys. Rev. Lett. Vol. 84, pp. 4220-4223, 2000.

[14] H. Ohno, H. Munekata, T. Penney, S. von Molnár and L. L. Chang, Phys. Rev. Lett. Vol. 68 pp. 2664-2667, 1992.

[15] H. Krenn, W. Zawadzki, and G. Bauer, Phys. Rev. Lett. Vol. 55, pp. 1510–1513, 1985.

[16] D. D. Awschalom, J. Warnock, and S. von Molnár, Phys. Rev. lett. Vol. 58, pp. 812-815, 1987.

[17] B. T. Jonker, J. J. Krebs, S. B. Qadri, and G. A. Prinz, Appl. Phys. Lett. Vol. 50, pp. 848-850, 1987.

[18] Y. Matsumoto, M. Murakami, T. Shono, T. Hasegawa, T. Fukumura, M. Kawasaki, P. Ahmet, T. Chikyow, S. Koshihara and H. Koinuma, Science vol. 291 pp. 854-856, 2001.

[19] T. Dietl, H. Ohno, F. Matsukura, J. Cibert and D. Ferrand, Science vol. 287, pp. 1019-1022, 2000

[20] P. Sharma, A. Gupta, K. Rao, F. J. Owens, R. Sharma, R. Ahuja, J. Osorio-Guillen, B. Johansson and G. Gehring, Nat. Mater. Vol. 2, pp.673-677, 2003.

[21] S. W. Lim, M. C. M C, M. H. Ham and J. M. Myoung, J. Appl. Phys. Vol. 43, pp. L280-L283, 2004.

[22] Q. Wang, Q. Sun, B. K. Rao, and P. Jena, Phys. Rev. B, vol. 69, pp. 233310-233313, 2004.

[23] N.F. Mott, Proc.R.Soc. London, Ser. A 153, 699-717 (1936a). N.F. Mott, Proc.R.Soc. London, Ser. A 156, 368-382 (1936b)

[24] R. Fiederling, P. Grabs, W. Ossau, G. Schmidt, and L. W. Molenkamp, Appl. Phys. Lett. 82, pp. 2160, 2003.

[25] A. Slobodskyy, C. Gould, T. Slobodskyy, C. R. Becker, G. Schmidt, and L. W. Molenkamp, Phys. Rev. Lett. 90, pp. 246601-246605, 2003.

[26] S. A. Wolf, D. D. Awschalom, R. A. Buhrman, J. M. Daughton, S. von Molnár, M. L. Roukes, A. Y. Chtchelkanova, D. M. Treger, Science, Vol. 294. pp. 1488 – 1495, 2001.

[27] M. T. Björk, B. J. Ohlsson, C. Thelander, A. I. Persson, K. Deppert, L. R. Wallenberg, and L. Samuelson, Appl. Phys. Lett. 81, pp. 4458, 2002.

[28] M. E. Flatté, and G. Vignale, Appl. Phys. Lett. 78, pp. 1273, 2001.

[29] H. Saito, A. Yamamoto, S. Yuasa, and K. Ando, J. Appl. Phys. 103, pp. 07D127, 2008.

[30] Jaroslav Fabian and Igor Žutić, Appl. Phys. Lett. 86, pp. 133506, 2005.

[31] M. E. Flatté and Z. G. Yu, E. Johnston-Halperin and D. D. Awschalom, Appl. Phys. Lett. 82, pp. 4740, 2003.

[32] Jaroslav Fabian Igor Žutić and S. Das Sarma, Appl. Phys. Lett. 84, pp. 85, 2004.

[33] Ming-Hao Liu and Ching-Ray Chang, Phys. Rev. B 73, pp. 205301-205305, 2006.

[34] Hyun-Woo Lee, S. Çalışkan, and Hyowon Park, Phys. Rev. B 72, pp. 153305-153308, 2005.

[35] S Caliskan, J. Phys.: Condens. Matter 18, pp.10313-10318, 2006.

[36] J. Carlos Egues, Guido Burkard, and Daniel Loss, Appl. Phys. Lett. 82, pp. 2658, 2003.

[37] M. E. Flatté, and G. Vignale, J. Appl. Phys. 97, pp. 104508, 2005.

[38] S. Das Sarma, J. Fabian and I. Žutić, Journal of Superconductivity, Vol 16, pp. 697-705, 2003.

[39] J. K. Furdyna, J. Appl. Phys.Vol. 64, pp. R29-R64, 1988.

[40] H. Ohno, Science, vol. 281, pp. 951-956, 1998.

[41] K. Sato and H. Katayama-Yoshida, Jpn. J. Appl. Phys. Vol. 39, pp. L555-L558, 2000

[42] H. Akinaga, T. Manago and M. Shirai, Jpn. J. Appl. Phys. Vol. 39, pp. L1118-L1120, 2000

[43] Medvedkin G A, Ishibashi T, Nishi T, Hayata K, Hasegawa Y and Sato K, Jpn. J. Appl. Phys. Vol. 39, pp. L949-L951. 2000

[44] J. P. Jakubovics, Magnetism and magnetic materials (Oxyford: Academic), 1987.

[45] Majlic and Norberto, The Quantum Theory of Magnetism (World Scientific), 2000.

[46] Yosida and Kei, Theory of Magnetism (Berlin: Springer), 1996.

[47] C. Zener, Phys. Rev. vol. 81 pp. 440-444, 1951.

[48] C.Zener, Phys. Rev.vol. 83, pp. 299-301, 1951.

[49] C. Zener, Phys. Rev. Vol. 82, pp. 403-405, 1951.

[50] A. C. Durst, R. N. Bhatt, and P. A. Wolff, Phys. Rev. B, vol. 65, pp. 235205-235214, 2002.

[51] T. Dietl, and H. Ohno, Mater.Res. Soc. Bull. Vol. 28, pp. 714–719, 2003.

[52] T. Dietl, and J. J. Spalek, Phys. Rev. B, vol. 28, pp. 1548–1563, 1983.

[53] P. A. Wolff, Vol. 25, (Academic, SanDiego), 1988

[54] D. E. Angelescu, and R. N. Bhatt, Phys. Rev. B, vol. 65, pp. 075211-075218, 2002.

[55] A. Kaminski, and S. Das Sarma, Phys. Rev. Lett. Vol. 88, pp. 247202-247205, 2002.

[56] N. Theodoropoulou, Phys. Rev. Lett. Vol. 89, pp. 107203-107206, 2002.

[57] X. Chen, Appl. Phys. Lett. vol. 81, pp. 511–513, 2002

[58] S. E. Park, Appl. Phys. Lett. Vol. 80, pp. 4187–4189, 2002.

[59] G. T. Thaler, Appl. Phys. Lett. Vol. 80, pp. 3964–3966, 2002.

[60] T. Sasaki, J. Appl. Phys. Vol. 91, pp. 7911–7913, 2002.

[61] S. A. Chambers, R. F. C. Farrow, Mater. Res. Soc. Bull. vol. 28, pp. 729–733, 2003.

[62] H. Saito, V. Zayets, S. Yamagata, and A. Ando, Phys. Rev. Lett. vol. 90, pp. 207202-207205, 2003.

[63] S. A. Chambers, Appl. Phys. Lett. Vol. 82, pp. 1257–1259, 2003.

[64] S. J. Pearton, J. Appl. Phys. Vol. 93, pp. 1–13, 2003.

[65] D. P. Norton, Appl. Phys. Lett. Vol. 82, pp. 239–241, 2003.

[66] S. B. Ogale, Phys. Rev. Lett. 91, 077205 ,2003.

[67] J. M. D. Coey, A. P. Douvalis, C. B. Fitzgerald, and M. Venkatesan, Appl. Phys. Lett.vol. 84, pp. 1332–1334, 2004.

[68] N. A. Theodoropoulo, Solid State Electron.vol. 47, pp. 2231–2235, 2003.

[69] K. Sato and H. Katayama-Yoshida, Jpn J. Appl. Phys. Vol. 40, pp.L651-L653, 2001.

[70] A. Tsukazaki, A. Ohtomo, T. Onuma, M. Ohtani, T. Makino, M. Sumiya, K. Ohtani, S. F. Chichibu, S. Fuke, Y. Segawa, H. Ohno, H. Koinuma, and M. Kawasaki, Nat. Mater. Vol. 4, pp. 42-46, 2005.

[71] H. W. Liang, Y. M. Lu, D. Z. Shen, Y. C. Liu, J. F. Yan, C. X. Shan, B. H. Li, Z. Z. Zhang, J. Y. Zhang, X. W. Fan, physica status solidi (a) Vol. 202, pp. 1060 – 1065, 2005

[72] T. Fukumura, Z. Jin, A. Ohtomo, H. Koinuma, and M. Kawasaki, Appl. Phys. Lett. Vol. 75, pp. 3366-3368, 1999

[73] S. W. Jung, S.-J. An, G.-C. Yi, C. U. Jung, S.-I. Lee, and S. Cho, Appl. Phys. Lett. Vol. 80, pp. 4561-4563, 2002..

[74] H.-J. Lee, S.-Y. Jeong, C. R. Cho, and C. H. Park, Appl. Phys. Lett. 81, pp. 4020-4022, 2002.

[75] Y. M. Cho, W. K. Choo, H. Kim, D. Kim, and Y. E. Ihm, Appl. Phys. Lett. Vol. 80, pp. 3358-3360, 2002..

[76] S-J. Han, J. W. Song, C.-H. Yang, S. H. Park, J.-H. Park, Y. H. Jeong, and K. W. Rhie, Appl. Phys. Lett. Vol. 81, pp. 4212-4214, 2002.

[77] K. Ueda, H. Tabata, and T. Kawai, Appl. Phys. Lett. Vol. 79, pp. 988-990, 2001.

[78] T. Wakano, N. Fujimura, Y. Morinaga, N. Abe, A. Ashida, and T. Ito, Physica E, vol. 10, pp. 260-264, 2001.

[79] H. Saeki, H. Tabata, and T. Kawai, Solid State Commun. Vol. 120, pp. 439-443, 2001.

[80] J. H. Kim, H, Kim, Y. E. Ihm, and W. K. Choo, J. Appl. Phys. Vol. 92, pp. 6066-6071, 2002.

[81] T. Fukumura, Z. Jin, M. Kawasaki, T. Shono, T. Hasegawa, S. Koshihara, and H. Koinuma, Appl. Phys. Lett. Vol. 78, pp. 958-960, 2001.

[82] Z. Jin, T. Fukumura, M. Kawasaki, K. Ando, H. Saito, T. Sekiguchi, Y. Z. Yoo, M. Murakami, Y. Matsumoto, T. Hasegawa, and H. Koinuma, Appl. Phys. Lett. Vol. 78, pp. 3824-3826, 2001.

[83] A. Tiwari, C. Jin, A. Kvit, D. Kumar, J.F. Muth, and J. Narayan, Solid State Commun. Vol. 121, pp. 371-374, 2002.

[84] G. Lawes, A. S. Risbud, A. P. Ramirez, and R. Seshadri, Phys. Rev. B, vol. 71, pp. 045201-045205, 2005.

[85] M. H. Kane, K. Shalini, C. J. Summers, R. Varatharajan, J. Nause, C. R. Vestal, Z. J. Zhang, and I. T. Ferguson, J. Appl. Phys. Vol. 97, pp. 023906-023911, 2005.

[86] S. J. Pearton, D. P. Norton, K. Ip, and Y. W. Heo, J. Vac. Sci. Technol. B, vol. 22, 932-948, 2004.

[87] X. M. Cheng and C. L. Chien, J. Appl. Phys. Vol. 93, pp. 7876-7878, 2003.

[88] M. Venkatesan, C. B. Fitzgerald, J.G. Lunney, and J.M. D. Coey, Phys. Rev. Lett. Vol. 93, pp. 177206-177209, 2004.

[89] M. Ivill, S. J. Pearton, D. P. Norton, J. Kelly, and A. F. Hebard, J. Appl. Phys. Vol. 97, pp. 053904-053908, 2005.

[90] D. P. Norton, M. E. Overberg, S. J. Pearton, K. Pruessner, J. D. Budai, L.

A. Boatner, M. F. Chisholm, J. S. Lee, Z. G. Khim, Y. D. Park, and R. G. Wilson, Appl. Phys. Lett. Vol. 83, pp. 5488-5490, 2003.

[91] K. Rode, A. Anane, R. Mattana, J.-P. Contour, O. Durand, and R. LeBourgeois, J. Appl. Phys. Vol. 93, pp. 7676-7678, 2003.

[92] S. G. Yang, A. B. Pakhomov, S. T. Hung, and C. Y. Wong, IEEE Trans. Magn. Vol. 38, pp. 2877-2879, 2002.

[93] N. Jedrecy,H. J. von Bardeleben, Y. Zheng, and J-L. Cantin, Phys. Rev. B 69, pp. 041308-041310, 2004.

[94] A. C. Tuan, J. D. Bryan, A. B. Pakhomov, V. Shutthanandan, S. Thevuthasan, D. E. McCready, D. Gaspar, M. H. Engelhard, J. W. Rogers, Jr., K. Krishnan, D. R. Gamelin, and S. A.Chambers, Phys. Rev. B vol. 70, pp. 054424-054432, 2004.

[95] N. Hong, V. Brize, and J. Sakai, Appl. Phys. Lett. Vol. 86, pp. 082505-082507, 2005.

[96] K. R. Kittilstved, N. S. Norberg, and D. R. Gamelin, Phys. Rev. Lett. Vol. 94, pp. 147209-147203, 2005.

[97] S. Kolesnik and B. Dabrowski, J. Appl. Phys. Vol. 96, pp. 5379-5381, 2004.

[98] D. A. Schwartz and D. R. Gamelin, Adv. Mater. Vol. 16, pp. 2115-2119, 2004.

[99] L. W. Guo, D. L. Peng, H. Makino, K. Inaba, H. J. Ko, K. Sumiyama, and Y. Yao, J. Magn.Magn. Mater. Vol. 213, pp. 321-325, 2000.

[100] A. Chartier, P. D'Arco, R. Dovesi and V. R. Saunders, Phys. Rev. B vol. 60, pp. 14042-14048, 1999.

[101] S-J. Han, T.-H. Jang, Y. B. Kim, B.-G. Park, J.-H. Park, and Y. H. Jeong, Appl. Phys. Lett. Vol. 83, pp. 920-922, 2003.

[102] K. Kopalko, A. Wójcik, M. Godlewski, E. Łusakowska, W. Paszkowicz, J.Z. Domagała, M.M. Godlewski, A. Szczerbakow, K. Świątek, K. Dybko, physica status solidi (c), Vol 2, Pp. 1125 – 1130, 2005.

[103] S. Kolesnik, B. Dabrowski, and J. Mais, J. Appl. Phys. Vol. 95 pp. 2582-2586, 2004.

[104] W. H. Brumage, C. F. Dorman, and C. R. Quade, Phys. Rev. B vol. 63, pp. 104411-104414, 2001.

[105] J. Shim,T. Hwang, S. Lee, J. Park, S. Han, and Y. H. Jeong, Appl. Phys. Lett. Vol. 86, pp. 082503-082505, 2005.

[106] Z. Jin, Y.-Z. Yoo, T. Sekiguchi, T. Chikyow, H. Ofuchi, H. Fujioka, M. Oshima, and H. Koinuma, Appl. Phys. Lett. Vol. 83, pp. 39-42, 2003.

[107] T. Fukumura, Y. Yamada, H. Toyosaki, T. Hasegawa, H. Koinuma, and M. Kawasaki, Appl, Surf. Sci. vol. 223, pp. 62-67, 2004.

[108] K. Sato and H. Katayama-Yoshida, Jpn. J. Appl. Phys. Vol. 40, pp. L334-L336, 2001.

[109] A.F. Jalbout, H. Chen, and S.L. Whittenburg, Appl. Phys. Lett. Vol. 81, pp. 2217-2219, 2002.

[110] E.-C. Lee and K. J. Chang, Phys. Rev. B vol. 69, pp. 085205-085209, 2004.

[111] Y. W. Heo, M. P. Ivill, K. Ip, D. P. Norton, and S. J. Pearton, Appl. Phys. Lett. Vol. 84, pp. 2292-2294, 2004.

[112] S. Ramachandran, A. Tiwari, and J. Narayan, Appl. Phys. Lett. Vol. 84, pp. 5255-5257, 2004.

[113] S.-W. Lim, D.-K. Hwang, and J.-M. Myoung, Solid State Commun. Vol. 125, pp. 231-235, 2003.

[114] A. S. Risbud, N. A. Spaldin, Z. Q. Chen, S. Stemmer, and Ram Seshadri, Phys. Rev, B vol. 68, pp. 205202-205208, 2003.

[115] X. Feng, J. Phys.: Condens. Matter. Vol. 16, pp. 4251-4259, 2004.

[116] H.-T. Lin, T.-S. Chin, J.-C. Shih, S.-H. Lin, T.-M. Hong, R.-T. Huang, F.-R. Chen, and J.-J. Kai, Appl. Phys. Lett. Vol. 85, pp. 621-623, 2004.

[117] Z. Jin, M. Murakami, T. Fukumura, Y. Matsumoto, A. Ohtomo, M. Kawasaki, and H. Koinuma, J. Cryst. Growth, vol. 214– 215, pp. 55-58, 2000.

[118] Z.-W. Jin, T. Fukumura, K. Hasegawa, Y.-Z. Yoo, K. Ando, T.Sekiguchi, P. Ahmet, T. Chikyow, T. Hasegawa, H. Koinuma,and M. Kawasaki, J. Cryst. Growth, vol. 237, pp. 548-552, 2002.

[119] P. Koidl, Phys. Rev. B vol. 15, pp. 2493-2499, 1977.

[120] Spin Electronics, edited by M.Ziese and M.J.Thornton (Springer, Berlin, 2001).

[121] A. Wolf, D. D. Awschalom, R. A. Buhrman, J. M. Daughton, S. Von Molnaer, M. L. Roukes, A. Y. Chtchelkanova, and D. M. Treger, Science 294, pp.1488 2001.

[122] Diluted magnetic Semiconductors, Semiconductors and Semimetals, edited by J. K. Furdyna and J. Kossut, Vol, 25 (academic, Boston, 1988).

[123] M. Jain, Diluted magnetic Semiconductor (World Scientific, Singapore, 1991).

[124] S. Sonoda, S. Shimizu, T. Sasaki, Y. Yamamoto, and H. Hori, J. Cryst. Growth 237, pp.1358, 2002.

[125] J. F. Moulder, W. F. Stickle, P. E. Sobol, and K. D. Bomben, in *Handbook of X-ray Photoelectron Spectroscopy*, edited by J. Chastain and R. C.King, Jr. Physical Electronics, pp.82, 1995.

[126] W. Prellier, A. Fouchet, B. Mercey, Ch. Simon, and B. Raveau, Appl. Phys. Let. 82, pp.3490, 2003

[127] J. M. D. Coey, M. Venkatesan, and C. B. Fitzgerald, Nature Mater. 4, pp.173 2005.

[128] M. H. F. Sluiter, Y. Kawazoe, P. Sharma, A. Inoue, A. R. Raju, C. Rout, and U. V. Waghmare, Phys. Rev. Lett. 94, pp.187204, 2005

[129] O. D. Jayakumar, I. K. Gopalakrishnan, S. K. Kulshreshtha, Adv. Mater. 18, pp.1857, 2006.

[130] J. H. Park, M. G. Kim, H. M. Jang, S. Ryu, Y. M. Kim, Appl. Phys. Lett. 84, pp.1338, 2004.

[131] S. Koshihara, A. Oiwa, M. Hirasawa, S. Katsumoto, Y. Iye, C. Urano, H.Takagi, and H. Munekata, Phys. Rev. Lett. 78, pp.4617, 1997.

[132] P. Erhart, and K. Albe, Appl. Phys. Lett. 88, pp.201918, 2006.

[133] P. Erhart, K. Albe, and A. Klein, Phys. Rev. B, 73, pp.205203, 2006.

[134] K.Sakai, T. Kakeno, T. Ikari, and S. Shirakata, J. Appl. Phys. 99, pp.043508, 2006.

[135] J. V. Grahn, P. E. Hellberg, and E. Olsson, J. Appl. Phys. 84, pp.1632, 1998.

[136] S. B. Zhang, S.-H. Wei, and A. Zunger, Phys. Rev. B 63, pp.075205, 2001.

[137] S. M. Park, T. Ikegami, and K. Ebihara, Thin Solid Films 513, pp.90, 2006.

[138] P. Zhao, Y. B. Xia, L. J. Wang, and J. M. Liu, Trans. Nonferrous Met. SOC. China 16, pp. s302, 2006.

[139] H. Tanaka, K. Ihara, T. Miyata, H. Sato, and T. Minami, J. Vac. Sci. Technol. A 22, 4, pp. 1757, 2004

[140] D.M. Hofmann, D. Pfisterer, J. Sann, B.K. Meyer, R. Tena-Zaera, V. Munoz-Sanjose, T. Frank and G. Pensl, Appl. Phys. A: Materials Science & Processing, Volume 88, pp.147-151, 2007

[141] Cowburn R P, J. Magn. Magn. Mater. pp. 242 505, 2002

[142] Gai Z, Howe J Y, Guo J D, Blom D A, Plummer E W and Shen J, Appl. Phys. Lett. 86, pp. 023107, 2005.

[143] Chio J H, Kim T-H, Seo J, Kuk Y and Suh M S, Appl. Phys. Lett. 85, pp.3235, 2004.

[144] Murillo R, van Wolferen H A, Abelmann L and Lodder J C, Microelectron. Eng. 78, pp. 260, 2005

[145] Xu W L, Zheng M J, Ding G Q and Shen W Z, Chem. Phys. Lett. 411 pp. 37, 2005

[146] Sato K, Hosokawa K and Maeda M, J. Am. Chem. Soc. 125, pp.8102, 2005

[147] Maxwell D J, Taylor J R and Nie S, J. Am. Chem. Soc. 124, pp.9606, 2002.

[148] Ross F M, Tersoff J and Reuter M C, Phys. Rev. Lett. 95, pp.146104, 2005.

[149] Dailey J W, Taraci J, Clement T, Smith D J, Drucker J and Picraux S T, J. Appl. Phys. 96, pp.7556, 2004.

[150] Fan S S, Chapline M G, Franklin N R, Tombler T W, Cassell A M and Dai H J, Science 283, pp.512, 1999.

[151] Li Y M, Kim W, Zhang Y G, Rolandi M, Wang D W and Dai H J, J. Phys. Chem. B 105, pp.11424, 2001.

[152] Buckmaster R, Hanada T, Kawazoe Y, Cho M W, Yao T, Urushihara N and Yamamoto A, Nano Lett. 5, pp.771, 2005.

[153] Stodolka J, Nau D, Frommberger M, Zanke C, Giessen H and Quandt E, Microelectron. Eng. 78, pp. 442, 2005.

[154] Andres R P, Bielefeld J D, Henderson J I, Janes D B, Kolagunta V R, Kubiak C P, Mahoney W J and Osifchin R G, Science 273, pp.1690, 1996.

[155] Santhanam V, Liu J, Agarwal R and Andres R P, Langmuir 19, pp.7881, 2003.

[156] Liang J Y, Luo H L, Beresford R and Xu J, Appl. Phys. Lett. 85, pp.5974, 2004.

[157] Ghanem M A, Bartlett P N, de Groot P and Zhukov A, Electrochem. Commun. 6, pp.447, 2004.

[158] Lei Y and Chim W K, Chem. Mater. 17, pp.580, 2005.

[159] Masuda H, Yasui K and Nishio K, Adv. Mater. 12, pp.1031, 2000.

[160] Masuda H and Satoh M, Japan. J. Appl. Phys. 35, pp.L126, 1996.

[161] W. Prellier, A. Fouchet, and B. Mercey, J. Phys.: Condens. Matter 15, pp. R1583, 2003.

[162] S.J. Pearton, W.H. Heo, M. Ivill, D.P. Norton, and T. Steiner, Semicond. Sci. Technol. 19, pp. R59, 2004.

[163] M. Joseph, H. Tabata, and T. Kawai, Japan. J. Appl. Phys. 38, pp.L1205, 1999.

[164] M. S. Sander and L-S. Tan, Adv. Funct. Mater. 13, pp.393, 2003.

[165] Hideki Masuda,a) Haruki Yamada, Masahiro Satoh, and Hidetaka Asoh, Masashi Nakao and Toshiaki Tamamura, Appl. Phys. Lett. 71, pp.19, 1997.

[166] Foreword Special Issue on Spintronics," IEEE transactions on electron devices, vol. 54, 2007.

[167] S. J. Pearton, D. P. Norton, M. P. Ivill, A. F. Hebard, J. M. Zavada, W. M. Chen, and I. A. Buyanova, IEEE transactions on electron devices, vol. 54, 2007.

[168] R. Janisch, PriyaGopal, and N. A. Spaldin, J. Phys.: Condens. Matter 17, pp.R657–R689, 2005.

[169] K. Sato and H. Katayama-Yoshida, Jpn. J. Appl. Phys., vol. 40, pp. L334-L336, 2001.

[170] K. Sato and H. Katayama-Yoshida, Jan. J. Appl. Phys. Vol. 39, pp. L555-558, 2000.

[171] K. K. Kim, J. H. Song, H. J. Jung, and S. J. Park, J. Appl. Phys. 87 (7) pp.3573–3575, 2000.

[172] B. J. Jin, S. Im, and S. Y. Lee, Thin Solid Films 366 (1/2), pp. 107–110, 2000.

[173] K. Ogata, T. Kawanishi, K. Maejima, K. Sakurai, and S. Fujita, Jpn. J. Appl. Phys. part 2, vol. 40, pp. L657-L659, 2000.

[174] H. Z. Wu, K. M. He, D. J. Qui, and D. M. Huang, J. Cryst. Growth vol. 217, pp. 131-137, 2000.

[175] S. A. Studenikin, N. Golego, and M. Cocivera, J. Appl. Phys. 84 (4), pp. 2287–2294., 1998.

[176] S. Z. Li, C. L. Gan, H. Cai, C. L. Yuan, J. Guo, P. S. Lee, and J. Ma, Appl. Phys. Lett. 90 (26), pp.263106, 2007.

[177] D. Zhao, C. Andreazza, P. Andreazza, J. Ma, Y. Liu, and D. Shen, Chemical Physics Letters, 408 pp.335–338, 2005.

[178] I. W. Kim, K. M. Lee, Nanotechnology, 19 pp. 355709, 2008

[179] D. C. Look, Phys. Rev. Lett. 82, pp.2552, 1999.

[180] A. F. Kohan, Phys. Rev. B, 61, pp.15019, 2000.

[181] M. K. Lee, H. F. Tu, Crystal growth and design, 8, pp.1785, 2008.

[182] R. Boubekri, Z. Beji, K. Elkabous, Chem. Mater., 21, pp.843, 2009.

[183] C. H. Chang, T. M. Hong, Appl. Phys. Lett. 93, pp. 212106, 2008

PUBLICATIONS

- Q. Liu, C. L. Gan, and G. C. Han, Appl Phys. Lett. **92**, 032501 (2008).
  Selected for the issue of Virtual Journal of Nanoscale Science & Technology.
- Q. Liu, C. L. Yuan, C. L. Gan, and G. C. Han, J. Appl Phys. **101**, 073902 (2007).
- Y. B. Zhang, Q. Liu, T. Sritharan, C. L. Gan, and S. Li, Appl. Phys. Lett. **89**, 042510 (2006)
- Q. Liu, H. Cai, C. L. Gan, and G. C. Han, MP3, Singapore (2006)
- Q.Liu, C.L.Gan, and G. C. Han, MS&T 07, Detroit, USA (2007)
- Y.B.Zhang, Q.Liu, T.Sritharan, and C.L.Gan, MRS, 2006